(i) Physical Studies of Distant Comets
(ii) Morphologies of Planetary Nebulae

Thesis by

David Jewitt

In Partial Fulfillment of the Requirements
for the Degree of
Doctor of Philosophy

California Institute of Technology
Pasadena, California
1983

(Submitted May 17, 1983)

Acknowledgements

I am grateful to my advisor, James Westphal, for the privilege of using the CCD camera "PFUEI" and for his continual support of my endeavors.

Many people have freely offered their time to assist with the collection of observations. I am especially grateful to Ed ("The Duke") Danielson for his participation in nearly all the Palomar observing expeditions, despite numerous professional and family conflicts. In addition, assistance was provided by Peter ("The King") Kupferman, Carolyn Porco, Michael Summers, Richard Terrile, John Hoessel, Barbara Zimmerman, Vance Hammerle, Donald Rudy, and Michael Ravine. They have made my observing runs a true pleasure.

Several astronomers selflessly gave me portions of their 200" time for observations of comets Halley and IRAS/Araki/Alcock. I am indebted to James Gunn, J.B. Oke, Maarten Schmidt, and Don Schneider for their extraordinary generosity.

The telescope expertise of Juan Carrasco, Skip Staples, Dave Tennant, Al Lilge, Bob Griffith, and Mike Doyle enabled many observations to be taken under difficult conditions. Relentless efforts by Wally van Ligten and Ardith Birdsell have transformed "the Monastery" from a cold building on a mountain top to a warm home from home. Bob Thicksten and Merle Sweet provided reassuring 24 hour support of the Palomar facilities.

At Caltech I have benefited from the free use of many marvelous programs written by Robert Deverill and Jerry Kristian. I thank Don Yeomans for providing dead accurate comet ephemerides.

I have greatly enjoyed working with the Caltech Infrared Army. The unusual mix of personalities found in Gerry Neugebauer, Tom Soifer, Keith

Matthews and Pat Neill will not be soon forgotten. Indeed, no datum will ever seem the same.

Donna Lathrop cheerfully typed dozens of drafts of my papers, and even translated them from English to American. I am surprised and happy to observe that she has managed to avoid the dehumanizing influences of (a) the word processor and (b) Scottish Country Dancing. I am likewise thankful to Kay Campbell, Brenda Smith, and Bernardine Burgess for their valuable help and advice.

I wish to record my thanks to Ed Danielson for his good humored toleration of this occasionally obstreperous graduate student. I treasure our many observing "traditions" from "mouse-turd muffin" to "standing in the devil." (However, "shooting the moose" does not get my approval, Ed, as you might have guessed.)

It has been my greatest honor to know Carolyn Porco. I sincerely appreciate our innumerable informative and refreshing conversations and I thank her for her disarming frankness and bright originality.

From Mike Summers I have learned that growing up on a farm in Kentucky can be surprisingly like growing up in a terraced house in north London. One day, Mike, you will admit that politics can be really interesting and that atheism is the only way.

I offer my thanks to Jon Lunine, Randy Gladstone, Jim Friedson, Don Rudy, Dave Paige, Dan Wenkert, and Jack Wisdom for wild conversations and car rides.

Preface

This thesis consists of four separate investigations into two classes of astronomical objects. The first two chapters concern the physical properties of distant comets, the last two chapters concern the small and large scale structure of planetary nebulae.

The observations reported in this thesis were taken by the writer in collaboration with several people. The optical observations of comets were taken at Palomar with G.E. Danielson. The infrared observations of comets were taken at Palomar by G. Neugebauer, B.T. Soifer, and K. Matthews and at the NASA-IRTF by the writer and R. Terrile. Both the neutral carbon and the diffuse halo observations of planetary nebulae were taken by the writer, G.E. Danielson, and P.N. Kupferman. The writer is responsible for the planning, reduction, analysis, and interpretation of the observations in all four parts of the thesis.

The first chapter of this thesis is a study of three distant comets in the wavelength range 0.5 to 20 μm. Grains of unidentifiable composition are discovered in two of the comets. The same comets are found to be much more active than normal water nucleus models predict. This work has been published in the *Astronomical Journal* **87**, 1854 (1982).

The second chapter is a detailed study of one of the comets discussed in chapter 1. Evidence is presented to show that the comet has been nearly inert since discovery. The large coma consists of dust grains ejected in a single non-equilibrium event at $R \approx 10$ AU. The comet model developed here is compared with the standard "dirty snowball" model.

The third chapter reports the detection of [CI] emission from a planetary nebula and proposes a model to account for its (unexpected) presence there. The model accounts for the CI by invoking small scale structures in the HII shell. This work has been accepted for publication in *The Astrophysical Journal.*

The fourth chapter is a report of a CCD survey of planetary nebulae made at the wavelength of Hα. The survey led to the discovery of numerous faint halos around the nebulae. The physical properties of the halos were determined in order to try to understand the reason for their existence. This work will shortly be submitted for publication in *The Astrophysical Journal.*

Abstract

Part 1:

Broadband observations of comets P/Stephan-Oterma (1980g), Bowell (1980b) and Panther (1980u) in the visual ($0.5 \lesssim \lambda(\mu m) \lesssim 0.9$) and infrared ($1.2 \lesssim \lambda(\mu m) \lesssim 20$) wavelength regions are reported together with measurements in the 1.5 to 2.4 μm wavelength range having 5% spectral resolution. The visual data indicate the existence of solid grains in extended halos around the nuclei of the three comets. The visual photometric profiles of comets P/Stephan-Oterma and Panther are interpreted as evidence that grains around Panther and those close to the nucleus of P/Stephan-Oterma are sublimating. Broadband near infrared and thermal infrared measurements of comet Panther suggest the presence of 2 to 4 μm radius particles in the coma. The particles within a 5.8×10^6 m diameter region centered on the comet have a total cross section of 10^8 m^2 and a near infrared geometric albedo of about 14%. Comet Bowell presents a total cross section of 3×10^8 m^2 within a 1.2×10^7 m region centered on the comet and its coma grains also have an albedo of 14%.

The near infrared spectrum of P/Stephan-Oterma is a featureless solar-reflection continuum. The near infrared spectra of Bowell and Panther exhibit features which are similar in the two comets. The spectral features are not due to H_2O, CH_4 or CO_2 ices nor to emissions from gases released from the nuclei nor to reflection from mineral grains of known composition in the comae. The spectrum of solid ammonia provides the best match to the near infrared; it is nevertheless significantly different from the comet spectra.

The synthesis of the visual data with the infrared data is attempted in

terms of a model involving a mantle of volatile material on the nuclei of Bowell and Panther, but not on P/Stephan-Oterma. The composition of the mantle cannot be exactly specified from the existing data but a complex molecule incorporating the N-H bond may be present.

Part 2:

An extensive series of observations of comet Bowell at optical and infrared wavelengths is summarized and interpreted in terms of a model of the outgassing of the nucleus. The observations indicate that the optical coma consists of large grains. The outer edge of the coma is expanding from the nucleus at $0.9 \pm 0.2\ \mathrm{ms}^{-1}$: extrapolation of the expansion suggests that the coma was ejected from the nucleus when the comet was at a heliocentric distance $R \sim 10$ AU. At this distance, water ice sublimation would be negligible. Models of the brightness of the comet as a function of R are compared with the measured brightness variation. Between $R = 5.3$ and 3.4 AU, the apparent cometary brightness changed by a factor of less than 20. Models which account for the equilibrium sublimation of volatiles from the nucleus predict much larger brightness variations. In particular, the models confirm that the sublimation of water ice does not control the activity of comet Bowell. The observations are consistent with the presence of an inert nucleus surrounded by a dissipating grain coma ejected impulsively at $R \sim 10$ AU. Strong OH production observed near $R = 3.4$ AU could be a result of the photodissociation of water molecules released from the coma grains by sublimation. However, near infrared spectra of the grains show no evidence for the presence of OH. Instead, several absorptions similar to the overtones of NH bond vibrations are observed. It is noted that the outgassing properties of the comet are similar to those of proton-bombarded laboratory ice specimens. Both the impulsive coma ejection and the peculiar near infrared spectrum may result from the presence of unstable compounds produced in the nucleus by cosmic ray bombardment. The activity of comet Bowell is quite unlike that exhibited by comets at small R, but may be representative of the properties of the distant comets.

Part 3:

The spatial distribution of [CI] 9823, 9850 Å emission in NGC 6720 is reported. Like [OI], the [CI] radiation appears enhanced in the region of the bright filaments. A few percent of the carbon atoms in the filaments are neutral. This neutral fraction is consistent with ionization equilibrium calculations made under the assumption of complete shielding of direct stellar radiation by hydrogen. The observed carbon lines are excited by photoelectrons produced from hydrogen by the nebular diffuse radiation field. The [CI] observations confirm that the filaments in NGC 6720 are regions of locally enhanced shielding.

Part 4:

The preliminary results of a CCD survey designed to detect and investigate faint halos around planetary nebulae are described. A TI 800 × 800 pixel CCD was used to take deep exposures of 44 planetary nebulae. The exposures were mostly obtained through an Hα filter at the Cassegrainian focus of the Palomar 1.5 m telescope. Spatial resolutions of 1 to 2 arcsecond were obtained across 400 arcsecond wide fields. The images, which are in many cases considerably deeper than any previously taken, reveal numerous planetary nebula halos. About 2/3 of the studied nebulae possess extensive outer halos. In some nebulae the mass in the halo is comparable to the mass contained in the primary HII region. We have used the data to place constraints on the mode of origin of the halos. It is likely that the halos originate either by dynamical separation of a single ejected shell of gas, or by the ejection of two or more such shells from the central star. It is less likely that the halos are caused by excitation of the pre-planetary stellar wind and highly improbable that the halos represent reflection nebulae.

Table of Contents

Part (i) Physical Studies of Distant Comets

Overview of Comets

The purpose of this overview is to provide an introduction to the modern understanding of comets. It is intended to set the context for the first two parts of this thesis. However, the overview is not intended to be comprehensive: little mention of the historical aspects of comets, their dynamical properties, their relation to the Zodiacal Light and meteor streams or of their mode of origin will be given. Introductions to these and other aspects may be found in works by Wyckoff (1982) and Brandt and Chapman (1982). A very reasonable introduction to comets may be obtained by reading Whipple (1950, 1951), Oort (1950) and Oort and Schmidt (1951). Modern comet science was born (and almost died) with the above four papers. Most subsequent work has tended only to confirm the Oort and Whipple models. This speaks for the validity of the models but also is an indicator of the slow rate of progress achieved by comet observers.

An unorthodox format has been adopted for the present work. The first section describes the large scale morphology of the comets. The second section summarizes the essential properties of the dirty water snowball model of the cometary nucleus. The observed properties of "typical" comets are given in the third section, where they are compared with the model properties. The final section describes the important differences between the observed and model properties of comets.

1. Large Scale Morphology

The large scale morphologies of comets are traditionally described in terms of three main components.

1.1 Coma

The coma is a roughly spherical region at the head of the comet having a radius on the order of 10^7 to 10^8 m. The coma has two constituents: gas and dust. The two may be empirically distinguished by taking optical spectra. The dust coma merely reflects the solar spectrum while the gas (atom, ion, molecule and radical) coma emits a resonance fluorescence spectrum. The dust coma displays a surface brightness variation well approximated by $B \propto p^{-1}$, where p is the angle impact parameter (arcseconds) measured from the coma center. The variation is consistent with the isotropic expansion of dust grains from a steady point source at the center. The gas displays a surface brightness variation which is a function of (a) the species responsible for the emission and (b) the heliocentric distance. The form of the variation is usually complicated, and will be briefly discussed in a later section. One generalization is possible, however; the surface brightness is always a decreasing function of increasing impact parameter. Near the outer edge of the coma the isophotes tend to deviate noticeably from circles in the plane of the sky. The coma grades smoothly into the comet tail.

1.2 Tail

The tail is a long projection from the coma which generally (but not always) trails away from the sun. Again, two types of tail may be distinguished on the basis of optical spectra.

1.2.1 Type I Tails

The spectra of type I tails consist primarily of emission lines and bands from ions and radicals (e.g. CO^+, H_2O^+, CH^+, CN^+, etc.). The tails appear visually blue, due to a prominent series of bands of CO^+ in the 4000-5000 Å wavelength range. On widefield photographs the type I tails may often be followed to great distances from the coma. Lengths in excess of 10^{11} m (~ 1 AU) are not uncommon for comets at $R \lesssim 1$ AU. Type I tails trail from the coma along lines which are approximately radius-vectors from the sun. These tails often display complex, time-dependent small scale morphologies which bear some (as yet unspecified) relation to the solar wind.

1.2.2 Type II Tails

The spectra of type II tails consist of scattered solar radiation from which the dust nature of the tails is inferred. The tails appear visually white (or sometimes yellow when the sodium D lines are strong (Gibson, 1975)). Type II tails are commonly followed for 10^9 to 10^{10} m from the coma — they are seldom as long as the type I ion tails. Another important difference concerns the shape of the type II tails. They are typically fan shaped with angles of divergence of $\sim 10°$ or $20°$. Furthermore, they are generally curved in the plane of the comet orbit. Type II tails are characterized by a diffuse appearance and rarely show small scale structure.

The type I and II tails both trail behind the coma of the comet. Sometimes an "anti-tail" is observed, which appears to project forward from the coma in the direction of the sun. The anti-tails are special cases of type II tails in which fortuitous viewing geometry allows part of the tail to *appear* projected in front of the coma.

A third class of tails, type III, is occasionally defined by some authors (e.g., see Sekanina, 1976). Type III tails are dust tails of exceptional curvature. However, since type III tails are not physically any different from type II tails, we prefer not to keep a separate subclass for them.

1.3 Optical Nucleus

The optical nucleus is a bright, centrally located feature seen in the comae of some comets. Its typical dimension is 1 arcsecond, comparable to the atmospheric seeing in most observations. The optical nucleus should be firmly distinguished from the true nucleus of a comet. A true nucleus is the kilometer-sized, solid object thought to lie at the center of the coma. The optical nucleus is a bright region in the coma. There are no convincing optical observations of a true nucleus but an "optical nucleus" is often detected. The causes of optical nuclei are many and varied: in some cases they are an optical illustion caused by a steep coma surface brightness function smeared by atmospheric turbulence. In other cases they may be caused by ice grain halos close to the true nucleus (see part I of this thesis). Perhaps the optical nuclei are to comet observers what canals were to Mars observers.

Older observations, particularly those by visual observers, often refer to intricate structures near the optical nucleus, and to multiple optical nuclei (Bobrovnikoff, 1931). In most cases, these observations probably refer to jets of gas and dust released from the (unobserved) true nucleus. In about twenty comets there is good evidence that the true nucleus has split into pieces.

2. The Snowball Model

Whipple (1950, 1951) proposed that the observed comae and tails of comets are produced from a small, unobserved, solid nucleus. The nucleus is composed of water ice mixed with dust particles. At large heliocentric distances, $R >> 1$ AU, the ice remains frozen and the comet has neither coma nor tail. At $R \lesssim 1$ AU the heating of the surface of the nucleus by absorbed solar radiation causes the ice to sublimate. The sublimated water molecules drag out the smaller dust grains and propel them into the coma. Subsequently, the molecules in the coma may be photodissociated (or less commonly, ionized). Their ionized fragments are channeled into the type I tail by the solar wind magnetic field. The dust grains move under the combined action of solar gravity and radiation pressure. They are pushed from the coma into the type II tail. The shape of the type II tail is determined by the ratio of the solar radiation pressure induced acceleration to the local solar gravity, and by the times of ejection of the dust grains.

The basic characteristics of the snowball model may be readily derived. We consider a solid water ice nucleus of spherical form and having a radius $r_n = 10^3$ m. The nucleus is at heliocentric distance R. The energy absorbed from the sun will be partitioned into (a) heating the surface of the nucleus to a finite temperature, T; and (b) sublimating molecules from the surface of the nucleus. Some energy will be conducted into the interior of the nucleus and will be used to heat the ice from the internal temperature of the nucleus ($T \approx 10$ K) up to the surface equilibrium temperature. However, in a first treatment the conduction term (which is small) may be neglected. The thermal equilibrium equation for the nucleus is, then,

$$\int_0^\infty \frac{F_\odot(\lambda)}{R^2}\Big[1 - A(\lambda)\Big]\, d\lambda = \chi \left[\pi \int_0^\infty \varepsilon(\lambda)\, B(\lambda,T)\, d\lambda + L(T)\, \frac{dm}{dt}\right] \tag{1}$$

Here, $F_\odot(\lambda)$ (J s^{-1} m^{-2} m^{-1}) is the solar flux density at unit heliocentric distance, R is the heliocentric distance in AU, $A(\lambda)$ is the albedo of the nucleus at wavelength $\lambda(m)$. On the right-hand side of equation (1), the thermal emission from the nucleus is put equal to the modified blackbody emission. $B(\lambda,T)$ (J s^{-1} m^{-2} m^{-1}) is the Planck function at temperature $T(K)$, $\varepsilon(\lambda)$ is the effective emissivity of the nucleus at λ, dm/dt (kg m^{-2} s^{-1}) is the rate of sublimation of the nucleus and $L(T)$ (J kg^{-1}) is the latent heat of sublimation of the ice. χ is the spin parameter which lies in the range $2 \leq \chi \leq 4$. $\chi = 2$ when the spin period of the nucleus is long compared to the cooling time of the nucleus and $\chi = 4$ when the reverse is true. The mass sublimation rate may be further expressed as

$$\frac{dm}{dt} = P(T) \left[\frac{\mu m_{\mathrm{H}}}{2\pi k T}\right]^{1/2} \tag{2}$$

where $P(T)$ (N m^{-2}) is the vapor pressure of the sublimated molecules, μ is the molecular weight of water, m_{H} (kg) is the mass of a hydrogen atom and k (J K^{-1}) is Boltzmann's Constant. The quantity in brackets is the inverse average speed of the molecules sublimated from the nucleus. The pressure, $P(T)$, is experimentally determined for water ice. To good approximation, however, $P(T)$ may be estimated using the Clausius-Clapeyron approximation for the slope of the solid-vapor phase boundary:

$$\frac{dP(T)}{dT} = \frac{L}{T \Delta V} \tag{3}$$

where the T dependence of the latent heat has been suppressed and where ΔV (m^3 kg^{-1}) is the change in the specific volume which occurs upon sublimation. To good order $\Delta V = V$ (vapor), since V (vapor) >> V (solid). The specific volume of the vapor is given by the perfect gas equation of state

$$V_v = \frac{kT}{\mu m_{\mathrm{H}} P(T)} \tag{4}$$

Substitution of (4) into (3) and integration gives

$$P(T) = P(T_0)\exp\left[\frac{\mu m_{\mathrm{H}}L}{kT_0}\right]\exp\left[\frac{-\mu m_{\mathrm{H}}L}{kT}\right] \qquad (5)$$

where $P(T_0)$, T_0 is a reference point on the phase boundary. Equations (2) and (5) together give the mass sublimation rate as a function of the temperature. With equation (1), the equilibrium temperature, and so the sublimation rate, may be found for any heliocentric distance.

The calculation of the sublimation rate, while conceptually simple, is dependent on several unknown or poorly constrained quantities. These include the albedo and emissivity of the nucleus and the spin parameter. Solutions for dm/dt have been computed under a range of assumed values of $\overline{A(\lambda)}$, $\overline{\varepsilon(\lambda)}$ and χ. Typical results are plotted in Figures 1, 2, and 3. The figures illustrate several important points.

1. The individual sublimation curves each consist of two regions – an inner region at $R \lesssim 3$ AU in which $dm/dt \sim R^{-2}$ and an outer region $R > 3$ AU in which dm/dt is a very strong function of R. The former region may be understood as the sublimation dominated regime. The second term on the right-hand side of equation (1) greatly exceeds the first at small R, giving $dm/dt \propto R^{-2}$ directly. At larger R, the first term cannot be neglected.
2. At small R, within the sublimation dominated regime, the effects of changing $\overline{A(\lambda)}$, $\overline{\varepsilon(\lambda)}$, and χ within wide limits are relatively minor. At large R the same changes produce drastic variations of dm/dt.
3. The turnover between the sublimation and radiation

Figure 1. The equilibrium sublimation mass flux as a function of heliocentric distance for a water ice nucleus. The effects of assuming a slow spinning ($\chi = 2$) and a fast spinning ($\chi = 4$) nucleus are shown. Computations assume Bond albedo $A = 0.10$ and unit emissivity.

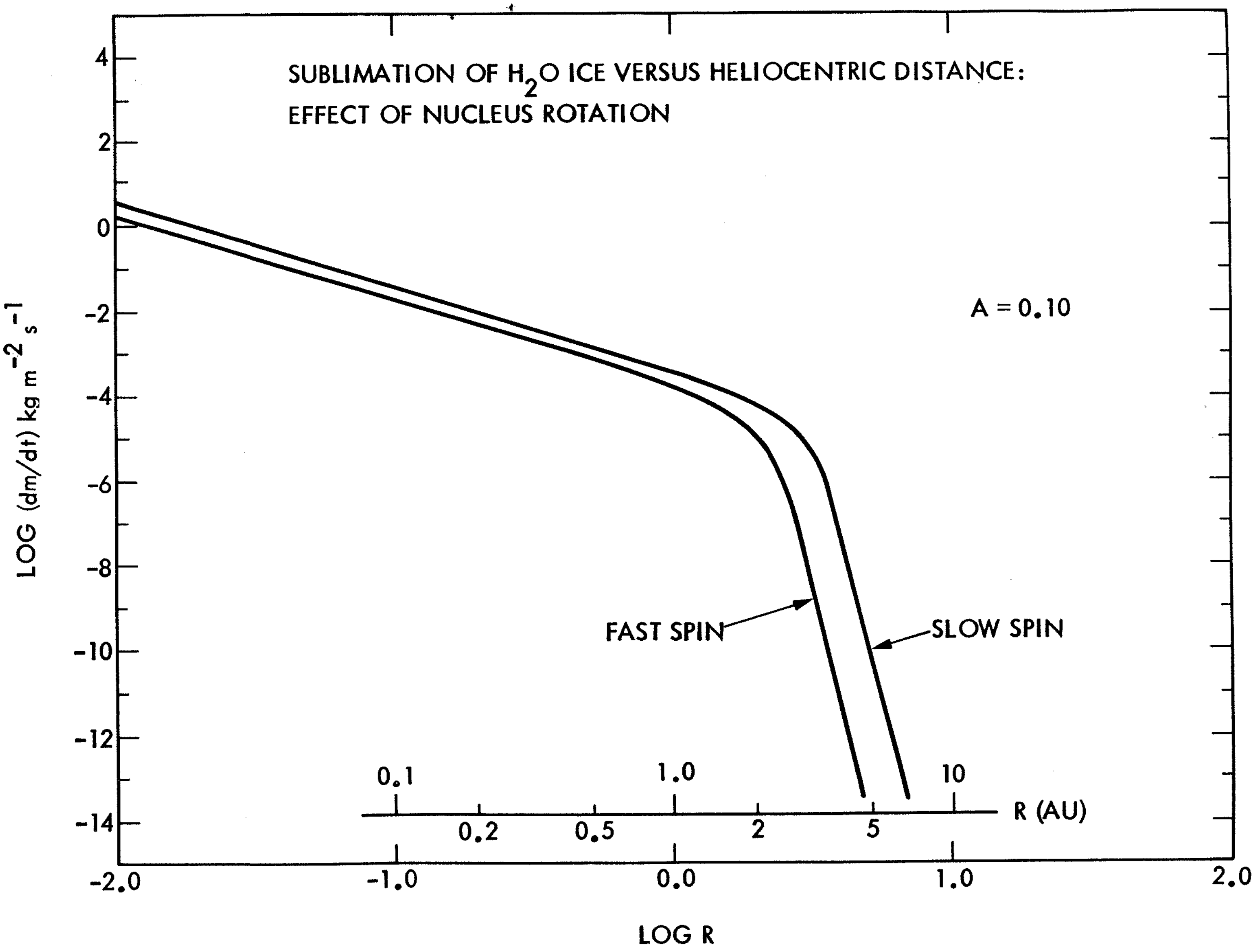

SUBLIMATION OF H_2O ICE VERSUS HELIOCENTRIC DISTANCE: EFFECT OF NUCLEUS ROTATION

Figure 2. The effect of the albedo of the nucleus on the sublimation mass flux. A rapidly spinning water nucleus having unit emissivity is assumed.

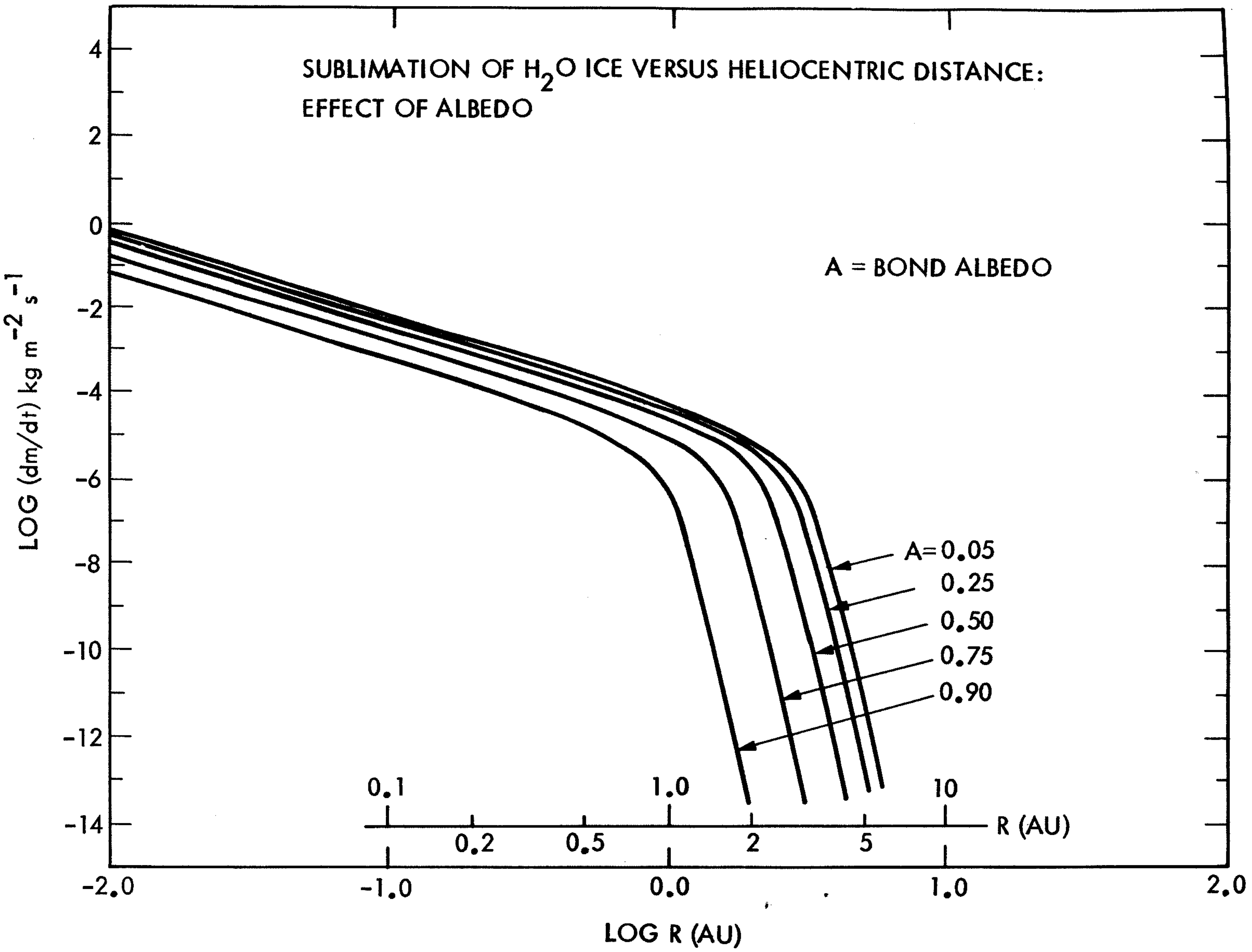
SUBLIMATION OF H_2O ICE VERSUS HELIOCENTRIC DISTANCE:
EFFECT OF ALBEDO
A = BOND ALBEDO
A=0.05
0.25
0.50
0.75
0.90
LOG (dm/dt) kg m^{-2} s^{-1}
4
2
0
-2
-4
-6
-8
-10
-12
-14
0.1
1.0
10
0.2
0.5
2
5
R (AU)
-2.0
-1.0
0.0
1.0
2.0
LOG R (AU)

Figure 3. Equilibrium subliation of water, ammonia, and nitrogen ices as a function of heliocentric distance. These illustrative solutions are for a rapidly spinning nucleus having a Bond albedo $A = 0.1$.

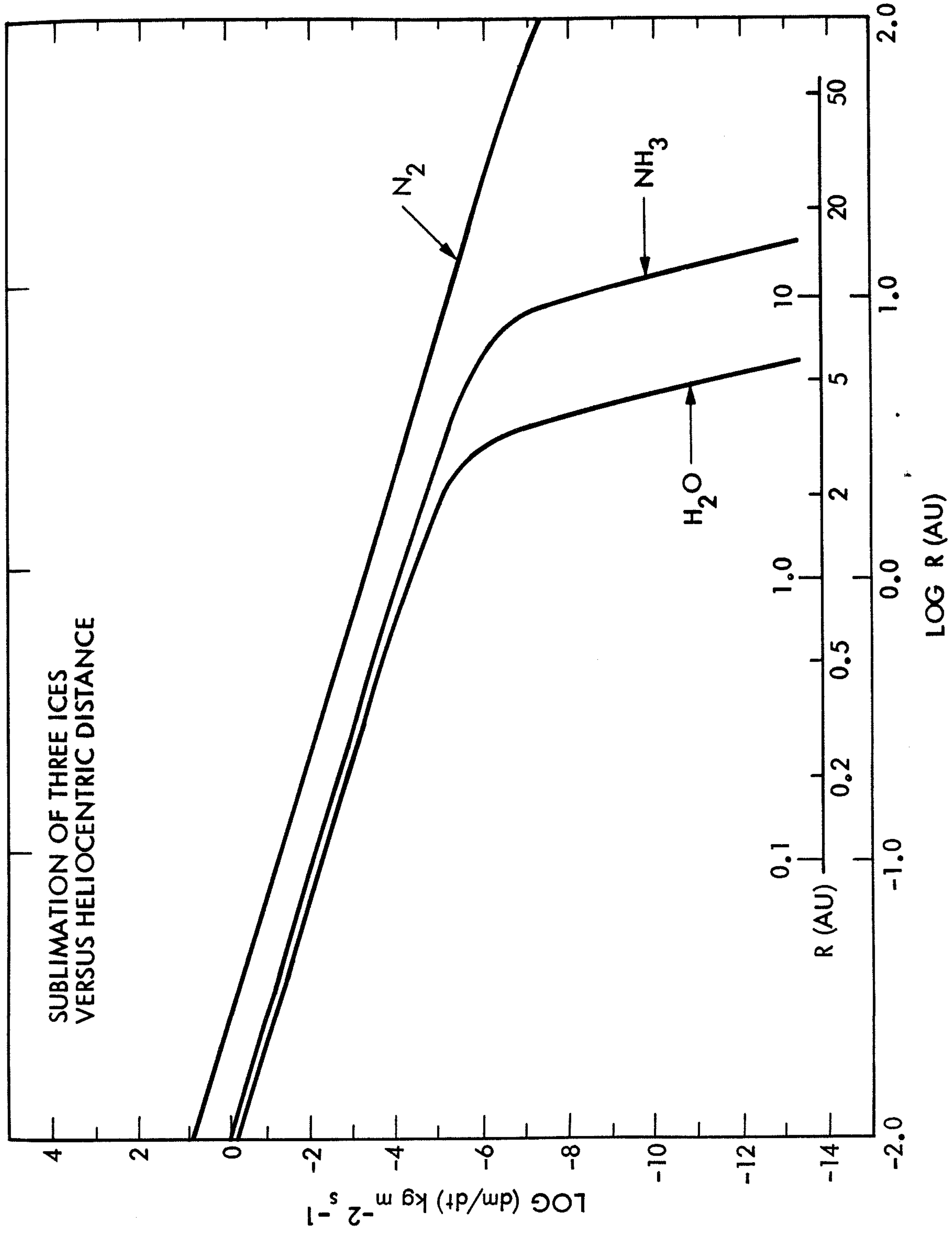
SUBLIMATION OF THREE ICES
VERSUS HELIOCENTRIC DISTANCE
N_2
NH_3
H_2O
R (AU)
0.1
0.2
0.5
1.0
2
5
10
20
50
-2.0
-1.0
0.0
1.0
2.0
LOG R (AU)
4
2
0
-2
-4
-6
-8
-10
-12
-14
LOG (dm/dt) kg m^{-2} s^{-1}

dominated regimes occurs within the range $1 \lesssim R\,(AU) \lesssim 3$. That is, the sublimation rate of a water ice nucleus drops catastrophically with increasing R beyond 1 to 3 AU. Hence the model predicts the cessation of coma and tail production beyond R = 1 to 3 AU, depending on the assumed parameters.

Also shown in Figure 3 are the sublimation rates calculated for N_2 and NH_3 ices. Evidently, N_2 is so volatile that its sublimation dominated regime extends throughout the entire solar system ($dm/dt \propto R^{-2}$, everywhere). The sublimation of NH_3 proceeds strongly out to a critical distance $R \simeq 15$ to 20 AU and declines rapidly thereafter.

Having defined the equilibrium sublimation rates as a function of heliocentric distance, we now fix our attention on the properties of a water body at R = 1 AU. Adopting (plausibly), $\overline{A(\lambda)} = 0.5$, $\overline{\varepsilon(\lambda)} = 1.0$, and $\chi = 4$ we obtain

$$\frac{dm}{dt}(\mathrm{H_2O}, R = 1\mathrm{AU}) = 10^{-3.6}\ \mathrm{kg\ m^{-2}\ s^{-1}} \quad . \tag{6}$$

A nucleus of 10^3 m radius would hence produce about 4×10^3 kg s^{-1} at R = 1 AU, or in terms of a molecular production rate, $Q_{H_2O} \simeq 10^{29}\ s^{-1}$.

The molecular number density at distance r from the center of the nucleus is

$$N_1(r) = \left[\frac{1}{\mu m_{\rm H} V}\right]\left[\frac{r_n}{r}\right]^2 \frac{dm}{dt} \quad , \quad r \geq r_n \tag{7}$$

where V (m s^{-1}) is the radial speed of the escaping gas and the flow is assumed to be isotropic. The outflow speed will be close to the speed of sound at the temperature of the nucleus. At R = 1 AU we adopt V = 500 m s^{-1}. Equations (6) and (7) then give

$$N_1(r) \simeq \frac{10^{25}}{r^2} \ \ (\mathrm{m}^{-3}) \tag{8}$$

The mean free path to collisions is $\lambda \simeq (N_1(r)\sigma)^{-1}$ where $\sigma \simeq 10^{-19}$ m^2 is a typical H_2O collision cross section. Collisions will be important inside a region of the coma of radius r_c, determined by the condition

$$\int_{r_c}^{\infty} N_1(r)\,\sigma\, dr \lesssim 1 \tag{9}$$

or

$$r_c \simeq 10^6 \ \mathrm{m} \quad .$$

All coma chemistry must occur within this tiny collisional zone.

In the snowball model, dust grains are dragged from the nucleus by sublimated molecules. The equation of motion is

$$\frac{4}{3}\pi\rho a^3 \frac{d^2r}{dt^2} = C_D \pi a^2 \left(V - \frac{dr}{dt}\right)^2 \mu m_{\mathrm{H}} N_1(r) \quad , \quad a << \lambda \tag{10}$$

where ρ (kg m^{-3}) is the grain density, C_D is a drag coefficient of order unity and the other quantities are as previously defined.

We define

$$A = 3C_D \, \mu m_{\mathrm{H}} \, N_1(r_n) r_n^2 / 4\rho a \tag{11}$$

and solve (10) to find

$$\frac{dr}{dt} = V \left[1 - \exp\left(\frac{-A}{r_n}\right)\right] \quad , \tag{12}$$

at R = 1 AU, $A/r_n \simeq 2 \times 10^{-7}/a$.

A typical 1 μm radius grain would be dragged from the nucleus at fractional speed $\frac{dr}{dt}/V \simeq 0.2$. We conclude that grains of $a \lesssim 1$ μm are well coupled to the gas in the inner coma. Larger grains acquire only a small fraction of the gas outflow speed.

The gravitational escape speed from a 1 km nucleus of density 1000 kg m^{-3} is $V_e \simeq 1$ m s^{-1}. Grains larger than a critical radius $a_c \simeq 10^{-4}$ m (100 μm) can never escape from the nucleus under the action of gas drag alone, at 1 AU.

3. Observed Properties

3.1 Constituents

A list of the observed cometary constituents is given in Table I. The list is an accumulation of results from the study of many comets: there does not exist a single comet in which all the listed species have been detected (Wyckoff, 1982). The majority of the observed species are produced in the coma by photodissociation of "parent molecules" which are themselves released from the nucleus by its sublimation. Only three of the listed species are believed to be undissociated parent molecules: H_2O, HCN and CH_3CN. The major objective of cometary spectroscopy is to deduce the identities of unobserved parents from the observed "daughters." Direct detection of the parent molecules is very difficult because of their short photodissociation lifetimes. Small molecules at $R = 1$ AU have photodissociation lifetimes $\approx 10^4$ s. With outflow speeds $v \simeq 500$ m s^{-1}, they travel only $\sim 5 \times 10^6$ m from the nucleus before being destroyed. The best attainable spatial resolutions are of the same order, for most comets. Consequently, the parents cannot generally be resolved.

The optical spectra of gas comae consist primarily of the resonance fluorescence lines of CN, CH, CO, C, C_2, and NH_2. The dominant constituents of the gas comae are H, OH, and O: these species have their strongest lines in the UV and are not represented in the optical.

Production rates of species are usually estimated from aperture photometry. The observing aperture typically samples only a

Table I

Observed Cometary Constituents

Coma

H								
C	C_2	C_3	CH	CN	CO	CS	HCN	CH_3CN
NH	NH_2							
O	OH	H_2O						
Na								
K								
Ca								
Cr								
Co								
Mn								
Fe								
Ni								
Cu								
V								
Si								
S								

Type I Tail

CO^+	CO_2^+	CH^+	Ca^+	N_2^+	OH^+	H_2O^+

Type II Tail

SiO_2, carbonaceous dust

small portion of the coma and so a correction needs to be applied to the measured flux densities in order to derive production rates. The correction is usually based on the Haser formalism, in which the parent and daughter molecules have known scale lengths l_p, l_d, respectively. Then the number density of the daughter at distance r from the nucleus may be written

$$N_d(r) = \frac{Q_d}{4\pi v r^2}\left[\exp\left[\frac{-r}{l_d}\right] - \exp\left[\frac{-r}{l_p}\right]\right]$$

The volume integration of $N_d(r)$ gives the total number of daughter molecules in the coma. If the lifetime of the daughter is known the production rate Q_d can be estimated. There is some error involved in the use of Haser's model. It assumes that both parent and daughter molecules travel radially from the nucleus at their respective speeds (which need not be equal). However, the parents sometimes have $l_p \lesssim r_c$, so that their motions are thermalized and not radial. Furthermore, each photodissociated parent ejects its daughter in a random direction from a point $\sim l_p$ from the nucleus. Lastly, there is evidence that ice grains in the coma may themselves act as copious sources of parent molecules far away from the nucleus. Consequently, application of the Haser formalism may lead to error in the calculation of production rates. The justification for its use is that it provides a simple *approximation* to the surface brightness distribution in some comets.

Production rate determinations have been made for about a dozen comets (Feldman, 1982; Weaver et al., 1981). The important properties are as follows:

A. $Q_H \sim 10^{28}$ s^{-1} to 10^{30} s^{-1} for comets at $R = 1$ AU. The variations between comets may be due to differences in the sizes of the nuclei or to differing albedos, etc.

B. $Q_H/Q_o \approx 2$ at all observed R. This strongly suggests that H_2O is the source of most cometary O and H.

C. Q_{CN}, Q_{CO}, etc. typically amount to only 1% to 10% of Q_H at a given R.

D. $Q_H(R) \propto R^{-n}$ with $2 \lesssim n \lesssim 4$ and $0.5 \lesssim R \lesssim 2$. Figs. 1, 2, and 3 show that sublimating water ice (or any more volatile materials) would give $n = 2$. Instances when $n = 4$ could provide evidence for the presence of an ice grain halo: the production of grains and the sublimation rate of grains would both vary as R^{-2}.

Table II contains a summary of the elemental abundances in comets as deduced from Q determinations (Delsemme, 1982). It shows that

A. H is underabundant by a factor of $\simeq 10^3$, relative to cosmic proportions.

B. $H/O \simeq 1.5$, implying the presence of a source of O in addition to H_2O.

C. C, S may be slightly underabundant and may be confined within dust grains.

Table II.

Element	Number Ratio Comet (1)	Cosmic (2)
H	1.5	1.5×10^3
C	0.2	0.55
N	0.1	0.1
O	$\equiv 1.0$	$\equiv 1.0$
S	0.003	0.02

(1) From Delsemme (1982).

(2) From Allen (1973).

4. Discrepant Comets

The previous sections indicate the remarkable correspondence between the properties of the snowball model and those of comets at small heliocentric distances, $R \lesssim 2$ AU. The agreement between the model and the observations strongly argues for the validity of the model. However, there exist numerous observations of comets which seem to contradict the model in its simplest form. These observations mostly refer to comets at $R \gtrsim 2$ AU which appear much brighter than would be expected on the basis of water ice nucleus sublimation, for example, comets Morehouse 1908 III and Humason 1962 III.

It cannot be supposed that the "over-active" comets merely have uncommonly large nuclei and so large sublimation cross-sections. Often, a comet which is well behaved and water-like at $R \lesssim 2$ AU exhibits anomalous activity at larger R. A more reasonable solution to the problem of the over-active comets might be that substances of greater volatility than water are present in the nucleus. Such substances could replace water as the source of the coma at $R \gtrsim 2$ AU where the water sublimation rate falls to a very low value (Fig. 3).

The over-active comets are generally "new" in the Oort-Schmidt (1950) sense: they are probably making their first close passage to the sun since the time of their formation. In fact, the above authors suggested that new comets might be coated with a volatile 'frost', causing them to appear excessively bright or 'active.' The frost would sublimate away during or soon after the first solar passage, if the comet were captured into a periodic orbit. Such a property was suggested to account for the observed deficiency of comets making second and third solar passages at intermediate heliocentric distances.

The nature of the volatile material is not known. Neither is it true to say that only new comets are over-active. Figure 4 shows periodic comet P/Schwassmann-Wachmann 1 at $R = 6.3$ AU in the midst of a surge of activity during which its brightness increased 100 times. It is not even clear that the material is present in a surface layer as opposed to being uniformly mixed throughout the nucleus. Finally, it is possible that the material responsible for excess activity causes it not by sublimation but by chemical reaction. For instance, in part 2 of this thesis evidence is presented which suggests a reaction of unstable radicals on the nucleus of a comet at $R = 10$ AU.

Figure 4. **Comet P/Schwassmann-Wachmann 1 as observed with the "PFUEI"** CCD camera on UT February 18, 1981. The comet was recorded through a broadband filter, centered at 0.65 μm wavelength, using the Palomar 1.5 m telescope. Five exposures of 300 s duration have been shifted and added. The coma is seen to be highly asymmetric. A spiral tail about 2.5×10^8 m across emanates from the region of the nucleus. The comet moves in a nearly circular orbit at $R \simeq 6$ AU and exhibits outbursts of the magnitude shown here several times per year. Such outbursts cannot be powered by sublimation of H_2O.

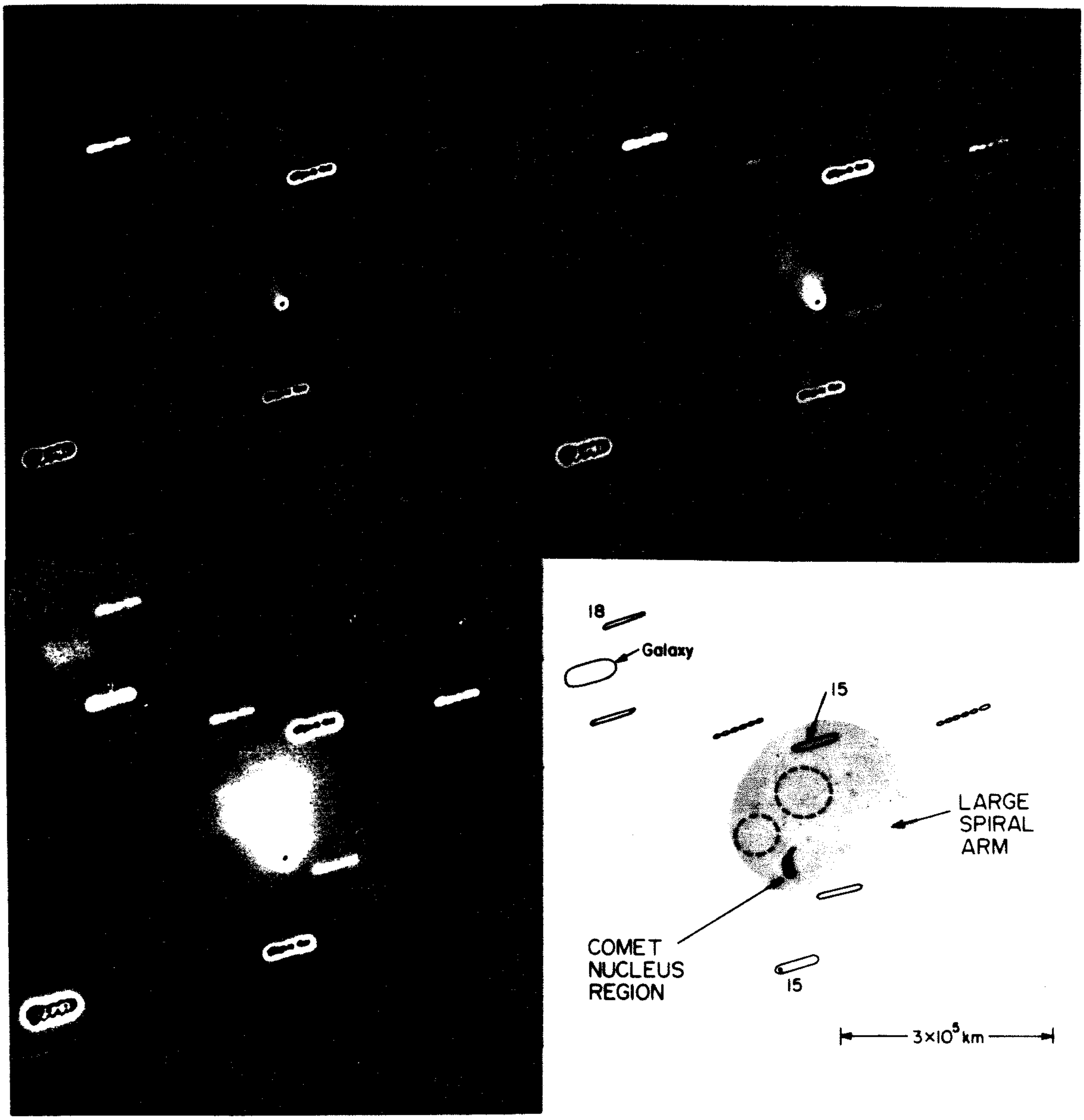
18
Galaxy
15
LARGE SPIRAL ARM
COMET NUCLEUS REGION
15
3×10⁵ km

References

Allen, C.W., (1973), "Astrophysical Quantities" Athlone Press, London.

Bobrovnikoff, N.T., (1931). Pub. Lick Obs. XVII, part II.

Brandt, J.C. and Chapman, R.D. (1981). "Introduction to Comets," Cambridge University Press.

Delsemme, A.H. (1982). In "Comets," edited by L.L. Wilkening, University of Arizona Press.

Feldman, P.D. (1982). In "Comets," edited by L.L. Wilkening, University of Arizona Press.

Gibson, E.G. (1975). In "Comet Kohoutek," NASA SP-355, Washington, DC.

Oort, J.H. (1950). *Bull. Astron. Inst. Netherlands* **11**, 91.

Oort, J.H. and Schmidt, M. (1951). *Bull. Astron. Inst. Netherlands* **11**, 91.

Sekanina, Z. (1976). In "The Study of Comets II," NASA SP-393, Washington, DC.

Weaver, H.A., Feldman, P.D., Festou, M.C., A'Hearn, M.F., and Keller, H.U. (1981). *Icarus* **47**, 449.

Whipple, F.L. (1950). *Ap. J.* **111**, 375.

Whipple, F.L. (1951). *Ap. J.* **113**, 464.

Wyckoff, S. (1982). In "Comets," edited by L.L. Wilkening, University of Arizona Press.

Visual and Infrared Observations of the Distant Comets P/Stephan-Oterma (1980g), Bowell (1980b) and Panther (1980u)

D.C. Jewitt,[1,2] B.T. Soifer,[1,3] G. Neugebauer,[1,3]
G.E. Danielson,[1,2,4] and K. Matthews[1,3]

Published *The Astronomical Journal*, **87**, 1854-1867 (1982)

Contribution number 3694 from the Division of Geological and Planetary Sciences, California Institute of Technology, Pasadena, California 91125.

[1] Palomar Observatory, California Institute of Technology.

[2] Division of Geological and Planetary Sciences, California Institute of Technology.

[3] Division of Physics, Mathematics and Astronomy, California Institute of Technology.

[4] Guest observer at the Kitt Peak National Observatory.

Abstract

Broadband observations of comets P/Stephan-Oterma, Bowell (1980B) and Panther (1980u) in the visual ($0.5 \lesssim \lambda(\mu m) \lesssim 0.9$) and infrared ($1.2 \lesssim \lambda(\mu m) \lesssim 20$) wavelength regions are reported together with measurements in the 1.5 to 2.4 μm wavelength range having 5% spectral resolution. The visual data indicate the existence of solid grains in extended halos around the nuclei of the three comets. The visual photometric profiles of comets P/Stephan-Oterma and Panther are interpreted as evidence that grains around Panther and those close to the nucleus of P/Stephan-Oterma are sublimating. Broadband near infrared and thermal infrared measurements of comet Panther suggest the presence of 2 to 4 μm radius particles in the coma. The particles within a 5.8×10^6 m diameter region centered on the comet have a total cross section of 10^8 m^2 and a near infrared geometric albedo of about 14%. Comet Bowell presents a total cross section of 3×10^8 m^2 within a 1.2×10^7 m region centered on the comet and its coma grains also have an albedo of 14%.

The near infrared spectrum of P/Stephan-Oterma is a featureless solar-reflection continuum. The near infrared spectra of Bowell and Panther exhibit features which are similar in the two comets. The spectral features are not due to H_2O, CH_4 or CO_2 ices nor to emissions from gases released from the nuclei nor to reflection from mineral grains of known composition in the comae. The spectrum of solid ammonia provides the best match to the near infrared; it is nevertheless significantly different from the comet spectra.

The synthesis of the visual data with the infrared data is attempted in terms of a model involving a mantle of volatile material on the nuclei of Bowell and Panther, but not on P/Stephan-Oterma. The composition of the mantle

cannot be exactly specified from the existing data but a complex molecule incorporating the N-H bond may be present.

1. Introduction

Comet nuclei are generally supposed to consist of heterogeneous mixtures primarily of water ice and refractory dust grains (Whipple, 1950, 1951). The thermodynamic properties of water ice are such that the gross features of cometary activity are well matched by a water based model. Quantities of more complex materials must be present in order to account for spectroscopic identifications of C, C_2, C_3, HCN, CO and numerous other radicals in comet comae and tails. Recent observations of H_2O^+ (Wehinger et al., 1974), and of appropriate quantities of H and O, support the notion that H_2O dominates the composition of comet nuclei. However an unambiguous direct detection of H_2O molecules in any comet has yet to be reported.

At intermediate heliocentric distances ($2 \lesssim R(\mathrm{AU}) \lesssim 10$) many comets exhibit activity in excess of that expected from a sublimating water nucleus. Modification of the canonical model by replacing water snow by clathrates of volatile molecules does not remove this problem: the sublimation rate of a CO_2 clathrate for instance, is similar to that of water ice itself since the water ice lattice must be disrupted before the CO_2 can escape (Delsemme and Miller, 1970). Most likely frozen volatiles are responsible for the excess activity but their identity is unknown. The problem is especially acute for many of the long period 'first appearance' comets which are frequently active at $R >$ 2AU. Two of the comets discussed in this work (Bowell and Panther) fall into this class. The other (P/Stephan-Oterma) is a short period object.

Although the above dilemma between theory and observation has been recognized for many years, few attempts have been made to resolve it by observational means. Broadband infrared observations have been taken from numerous comets (Becklin and Westphal, 1966; O'Dell, 1971; Ney, 1975). Only two attempts have been made to detect the near infrared spectral features of ices in comets. Oishi et al. (1978) failed to detect any such features in comet West because the 3 μm region of the comet spectrum was contaminated by strong thermal emission. More recently A'Hearn et al. (1981) examined P/Stephan-Oterma and obtained a reflection spectrum devoid of features but similar to the spectrum reported in the present work. Because of the large diaphragm used by these observers it is likely that the near infrared spectrum they obtained refers to refractory grains in the outer coma and not to ice grains in a cloud near the nucleus. In this paper we report combined visual imagery and spectroscopy, near infrared spectroscopy and broadband infrared photometry of the three mentioned comets at intermediate heliocentric distances.

2. Observations at Visual Wavelengths

Observations in the visual range ($0.5 \lesssim \lambda(\mu m) \lesssim 0.9$) were obtained with the CCD camera built by the Space Telescope Wide Field and Planetary Camera Investigation Definition Team (Gunn and Westphal, 1981). The camera ("PFUEI") enables rapid interchange between operation as a direct camera and as a low resolution ($\lambda/\Delta\lambda \sim 250$) visual spectrograph. PFUEI was used at the prime focus of the Hale 5.1 m telescope and at the Cassegrainian focus of the 1.5 m telescope, both at Palomar Observatory and at the Cassegrainian focus of the 2.1 m telescope at KPNO. A journal of observations, together with a list of relevant camera parameters is given in Table 1.

The characteristics of the PFUEI which are especially relevant to the comet imaging include the seeing-limited spatial resolution (commonly 1 to 2 arcseconds), the good linearity of the detector response (0.1%), the great sensitivity (the quantum efficiency of the detector averages 0.5 at $\lambda \sim 0.6$ μm) and the large dynamic range. The latter is especially important for studies near the photometric nuclei of the comets where the coma surface brightness may vary greatly over short distances. In the spectrographic mode a 105 × 2 arcsecond slit was used.

In addition to the data frames listed in Table 1, numerous flat field and erase frames were recorded. These were subsequently used to remove the zero exposure bias signal from the CCD chip and to divide-out pixel to pixel variations in the sensitivity. The processed data frames are generally found to be uniform at the 1% level over their full width. Defective pixels remain imperfectly "flattened" but are, however, so few in number (< 0.1% of the total) as to be largely negligible. When precision photometry was performed the defective pixels were eliminated by replacing them with the average value of the four adjacent pixels. Processed data frames are limited by photon noise. Occasionally several consecutive frames were digitally stacked to improve the signal to noise ratio. The stars BD+26°2606, BD+29°2091, BD+54°1216, HD 84937 and HD 19445 were recorded to provide measures of the absolute surface brightnesses of the comets (Thuan and Gunn, 1976).

The appearances of the comets through broadband filters with bandpasses ~ 0.1 μm and central wavelengths 0.50, 0.65, 0.80 and 0.95 μm were similar. Unless otherwise noted the following descriptions apply to all filters but

Table 1. Journal of Visual Observations

Date	Telescope Diameter (m)	Image Scale (arcseconds per pixel)	Seeing (arcsecond)	Direct Frames*	Spectra*
12/17/80	1.5	0.59	1 to 2	S-O	S-O
12/18/80	1.5	0.59	2	S-O,B	S-O
2/18/81 to 2/23/81	1.5	0.59	1 to 2.5	S-O,B	B
3/21/81	5.1	0.42	5	—	P,S-O
5/6/81	2.1	0.46	1.5	P	—
5/18/81	1.5	0.59	1 to 2	S-O,B	—

*S-O = Stephan-Oterma, B = Bowell, P = Panther.

refer specifically to data taken with the 0.65 μm filter. Table 2 lists the heliocentric distance R, geocentric distance Δ, and phase angle α for each comet at the first and last dates of observation.

The photometric profiles of the comets were examined by taking brightness averages within concentric circular annuli about the photometric centers of the comae. Representative results are plotted in Figure 1. The ordinate is the logarithm of the surface brightness B above the sky background B_s (in arbitrary units). On the abscissa is plotted the logarithm of the radial distance from the photometric center in arcseconds. The error bars represent the maximum uncertainties associated with the determination of the sky background. Statistical uncertainties in the coma-signal are negligible as are errors due to imperfect location of the photometric center. Where errors are not plotted it is because they are too small to be shown at the scale of the graph.

2.1 P/Stephan-Oterma

The main feature of this comet was an almost stellar brightness enhancement around the location of the nucleus. This is shown in Figure 2 by a brightness profile across the nuclear region of the comet and across a typical field star. The extended wings at the base of the comet profile are due to the extended coma. The full width of half maximum (FWHM) of the nuclear region (1.58 ± 0.03 arcsec) was found to be significantly larger than the FWHM of nearby field stars (1.40 ± 0.03 arcsec), indicating the presence of a 0.7 ± 0.1 arcsec [$(8 \pm 1) \times 10^5$ m diameter] cloud around the nucleus. The enhanced nuclear region was observed in frames obtained December 1980 through May 1981, though the degree of enhancement decreased during this

Table 2. Supporting Comet Information

Comet	Period of Observations	R (AU)	Δ (AU)	α (degrees)
P/Stephan-Oterma	12/15/80- 5/19/81	1.58- 2.59	0.60- 2.52	3- 23
Bowell	12/18/80- 5/19/81	5.34- 4.38	5.42- 3.73	10.- 11
Panther	3/21/81- 5/6/81	1.80- 2.10	1.42- 2.11	33- 27

Figure 1. **Logarithmic brightness profiles of the three comets at** 0.65 μm wavelength. The ordinate is proportional to the logarithm of the surface brightness of the coma above the sky background. The coma surface brightness was averaged around concentric annuli centered on the nucleus. The logarithm of P, the radius of the annulus in arcseconds is plotted on the abscissa. For clarity only about half of the measured data points have been plotted for each comet. The continuous lines represent model fits described in the text. The fits to the surface brightness, B, are not plotted for $\log(p) < 0.4$ or for $(B - B_s) < 0.1\ B_s$, where B_s is the sky background brightness. In each graph, $B_s \sim 10^3$ data numbers. The three profiles were measured from CCD images taken 12/17/80, 5/6/81 and 2/20/81, respectively.

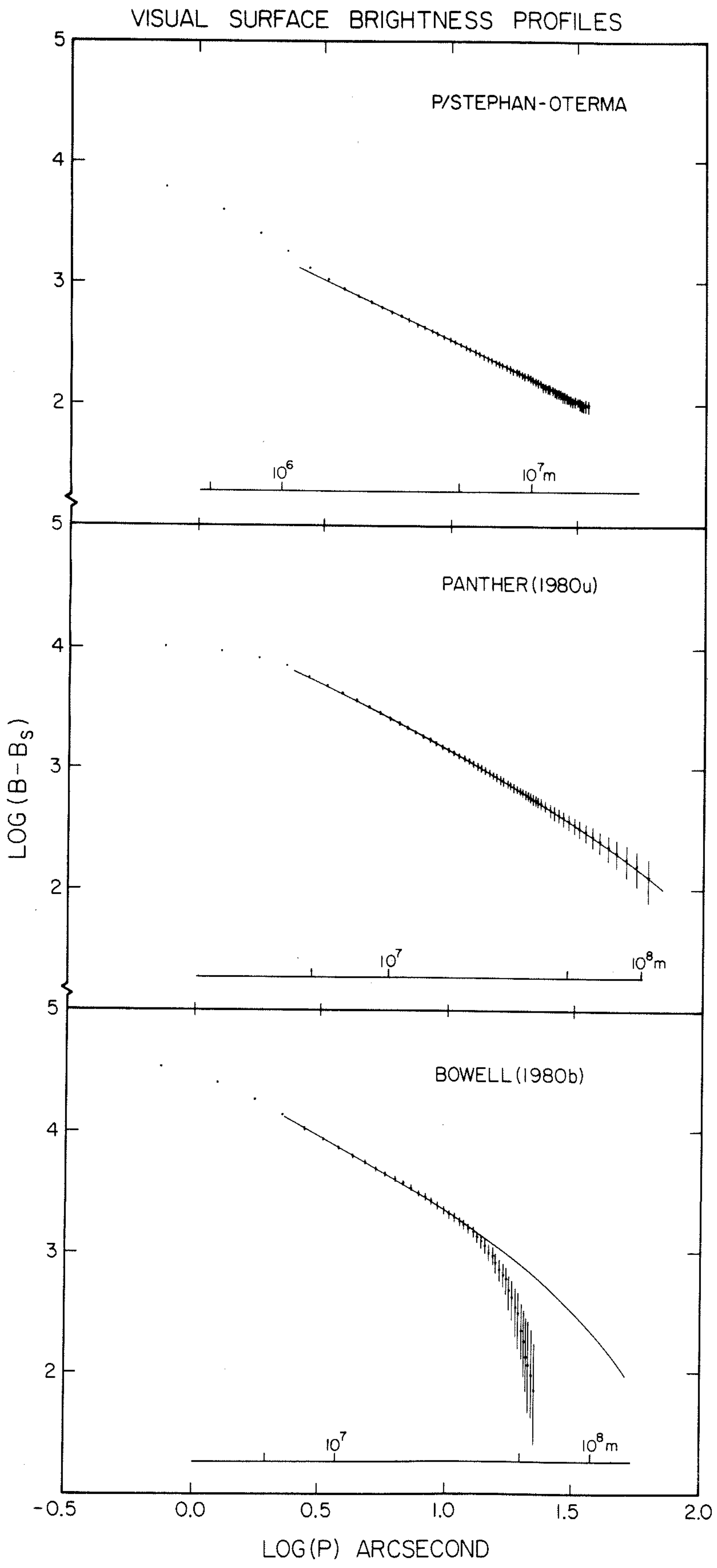
VISUAL SURFACE BRIGHTNESS PROFILES
P/STEPHAN-OTERMA
10^6
10^7m
PANTHER (1980u)
10^7
10^8m
BOWELL (1980b)
10^7
10^8m
LOG (B - B_S)
5
4
3
2
-0.5
0.0
0.5
1.0
1.5
2.0
LOG (P) ARCSECOND

Figure 2. **Brightness profiles across the central region of comet P/Stephan-Oterma** (solid line) and across a star image (dotted line) are taken from a single CCD frame. The pixel size is 0.59 arcsec. In addition to having broad 'wings' due to coma the comet profile has a FWHM significantly larger than the 1.40 ± 0.03 arcsec FWHM of the star image. A central 'cloud' (8 ± 1) × 10^5 m diameter is present in the comet. The profile was measured from a CCD image taken on 12/17/80 with the Palomar 1.5 m telescope.

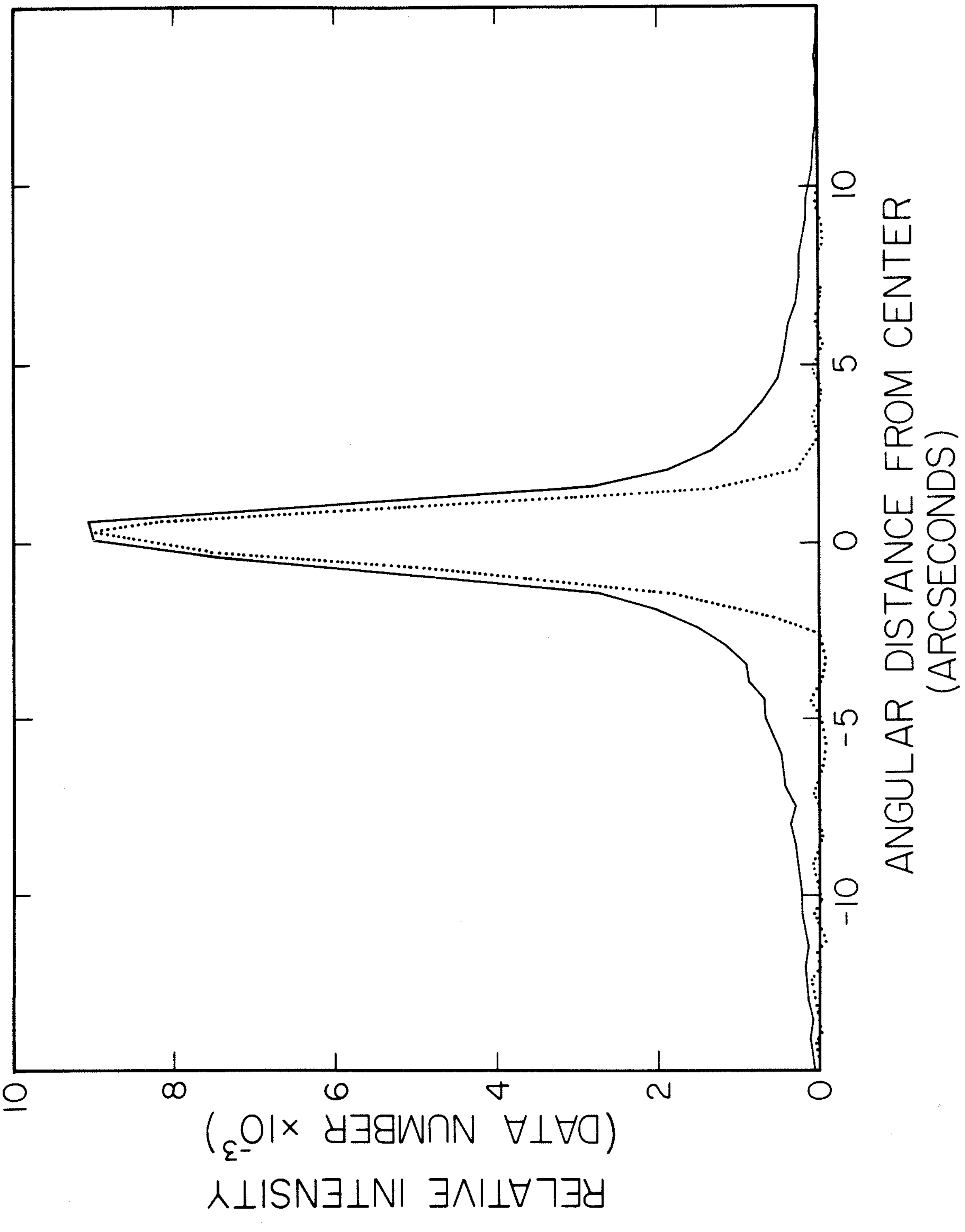
RELATIVE INTENSITY
(DATA NUMBER ×10^{-3})
0
2
4
6
8
10
ANGULAR DISTANCE FROM CENTER
(ARCSECONDS)
-10
-5
0
5
10

period. In mid February 1981 the material in the resolved nuclear region had an albedo, cross-section product equal to 8.0×10^7 m^2, as judged by aperture photometry from CCD frames. Out to a radius of 10 arcsec ($\sim 10^7$ m), the isophotes of the coma remain closely circular.

Visual spectra of the coma and nuclear region of comet P/Stephan-Oterma show a bright solar reflection continuum with a few weak emissions from [OI] and C_2 (Figure 3). Between 0.5 and 0.7 μm the gaseous emissions contribute < 1% to the total brightness of the comet in February 1981 data.

2.2 Comet Panther

Comet Panther displayed a bright coma, spherically symmetric out to $\sim 10^7$ m. No nuclear condensation was seen (see Figure 1). The albedo cross section product within a circular aperture of 2×10^7m projected radius was 1.7×10^8 m^2; this value may be uncertain by up to 50% since the comet was observed on a night of low photometric quality.

Visual slit spectra of comet Panther reveal many prominent spectral lines and bands. These are shown in Figure 3, together with several line identifications. An estimated 1% of the total light between 0.5 and 0.7 μm was gaseous emission, the remainder was reflection continuum.

2.3 Comet Bowell

This comet displayed a large bright coma in all filters. Its photometric profile, shown in Figure 1, gives no evidence for a strong central condensation. The material within 2×10^7 m of the nucleus had an albedo-cross section product equal to 1.0×10^8 m^2, similar to that present in the nuclear excess of P/Stephan-Oterma alone. A faint stubby tail extending in the anti-solar direction was evident in the PFUEI data. The contribution of the tail to the total

Figure 3. Visual spectra obtained from CCD frames. The ordinates are proportional to the flux density at each wavelength. C_2 band-heads and NH_2 emission lines are identified. Lines partly or wholly due to night sky emission are marked with dots. The spectrum of P/Stephan-Oterma was taken on 12/18/80 with the Palomar 1.5 m telescope, while the spectra of comets Panther and Bowell were taken with the Palomar 5 m telescope on 3/21/81 and 2/21/81, respectively.

VISUAL SPECTRA OF COMETS
P/STEPHAN-OTERMA, PANTHER AND BOWELL

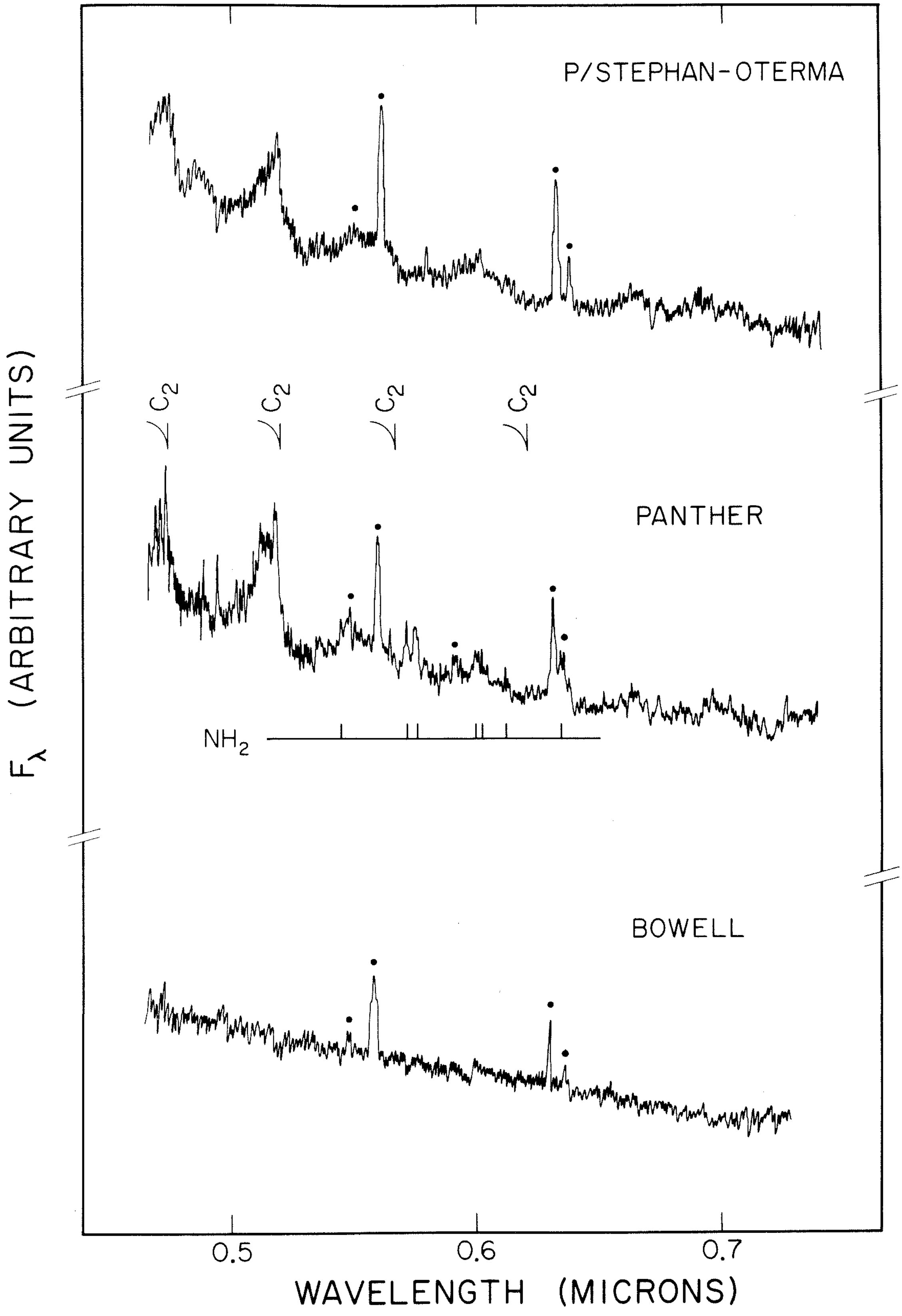

light of the comet was estimated to be < 5%.

Visual spectra taken with the slit across the nuclear region of the comet reveal a solar reflection continuum completely devoid of gaseous emissions, typical of many comets at such large heliocentric distance, (R = 5 AU in February 1981).

3. Spectral Observations at Near Infrared Wavelengths

Comets P/Stephan-Oterma and Panther were observed in the near infrared on UT March 16, 1981 using the Palomar 5 m telescope. Observations of comet Bowell were acquired on UT April 14, 1981. The infrared observations were obtained with an InSb detector cooled to 55 K and a circular variable filter (CVF) wheel cooled to 77 K. The spectra had a resolution $\lambda/\Delta\lambda \sim 20$. Photometric observations were obtained successively at wavelengths separated by half resolution intervals. For the Bowell and Panther observations a 6 arcsecond diameter diaphragm was used with 6 arcsecond chop in the north-south direction to remove infrared background radiation. In the case of P/Stephan-Oterma a smaller diaphragm of 3 arcseconds was used with a 3 arcsecond chop in the north-south direction. The smaller diaphragm was selected in order to maximize the contribution to the signal from the central excess of P/Stephan-Oterma (cf: §2.1). This accounts for the relatively larger errors in the spectrum of the latter object as compared with those in the Panther and Bowell spectra. Except for the measurements of comet Bowell between 1.46 and 1.78 μm the measurements, summarized in Table 3, are averages of two or three values obtained in consecutive wavelength scans. In each case the individual scans were similar within the statistical uncertainties. The conversion to absolute flux density was achieved through observations of

Table 3. Measured Near Infrared Flux Densities.

Wavelength (μm)	Stephan-Oterma (mJy)	Bowell (mJy)	Panther (mJy)
1.46	—	3.87 ± 0.29	—
1.50	1.22 ± 0.08	4.12 ± 0.14	28.4 ± 0.4
1.54	1.19 ± 0.08	3.95 ± 0.10	27.3 ± 0.4
1.58	1.30 ± 0.08	3.97 ± 0.13	26.8 ± 0.4
1.62	1.18 ± 0.07	4.09 ± 0.08	26.4 ± 0.4
1.66	1.15 ± 0.03	3.71 ± 0.09	26.3 ± 0.4
1.70	1.21 ± 0.05	3.95 ± 0.08	26.2 ± 0.4
1.74	1.11 ± 0.05	3.61 ± 0.07	26.6 ± 0.4
1.78	1.22 ± 0.04	3.66 ± 0.16	28.0 ± 0.4
2.00	0.90 ± 0.04	2.78 ± 0.06	20.0 ± 0.3
2.05	0.88 ± 0.03	2.85 ± 0.06	19.9 ± 0.3
2.10	0.92 ± 0.03	2.81 ± 0.06	19.5 ± 0.3
2.15	0.79 ± 0.03	2.75 ± 0.09	19.7 ± 0.3
2.20	0.88 ± 0.05	2.65 ± 0.07	19.0 ± 0.3
2.25	0.99 ± 0.04	2.54 ± 0.06	18.1 ± 0.3
2.30	0.82 ± 0.06	2.39 ± 0.09	17.6 ± 0.3
2.35	0.76 ± 0.06	2.48 ± 0.11	18.7 ± 0.3
2.40	0.77 ± 0.04	2.50 ± 0.12	17.9 ± 0.3
2.45	—	2.50 ± 0.26	—

early type stars at similar airmasses. The spectra were divided by the solar spectrum as measured by Arveson et al. (1969) to obtain relative reflectivities. The relative reflectivities of the three comets normalized to unity at 2.20 μm are presented in Figure 4.

The near infrared relative reflectivities of Bowell and Panther are identical within the uncertainties. Both comets exhibit a broad reflectivity minimum centered at 2.22 ± 0.02 μm. Reflectivity maxima at 1.78, 2.15 and > 2.40 μm are common to both objects, as is a trend of increasing reflectivity with wavelength.

Although the similarity between the reflectivities of comets Bowell and Panther is clear it is less clear whether the P/Stephan-Oterma reflectivities agree with or significantly differ from those of Panther or Bowell, especially in view of the larger uncertainties on the former. The value of $\chi^2 = 17$ was computed between the mean Panther-Bowell and P/Stephan-Oterma spectra. The number of data points was 17. The chance that this value of χ^2 (or a larger one) would result from measurements of identical spectra is ~ 0.4. Hence the P/Stephan-Oterma spectrum has the same shape as the average Panther-Bowell spectrum within the uncertainties. A'Hearn et al. (1981) have also measured the near infrared spectrum of P/Stephan-Oterma but used a 10 arcsecond diaphragm. Using their reflectivities to compare P/Stephan-Oterma with Panther gives $\chi^2 = 18$ from 17 data points: again there is ~ 0.4 chance that the P/Stephan-Oterma and Panther-Bowell reflectivities are the same. Hence the P/Stephan-Oterma spectrum is consistent with the Panther and Bowell spectra within the uncertainties of the measurements.

Figure 4. Near infrared reflectivities obtained by dividing the cometary flux densities by the solar flux density. The comet reflectivities have been normalized at 2.2 μm. The laboratory spectra of ice are arbitrarily normalized. A 3 arcsecond diaphragm and 3 arcsecond beam chop were used for the observations of comet P/Stephan-Oterma in order to suppress the contribution from the isotropic coma and to enhance that from the nuclear excess. The spectra of comets P/Stephan-Oterma and Panther were obtained on 3/16/81. The spectrum of comet Bowell was obtained on 4/14/81. All observations were with the Palomar 5 m telescope.

Normalised Reflectivities of Three Comets and of Common Ices versus Wavelength

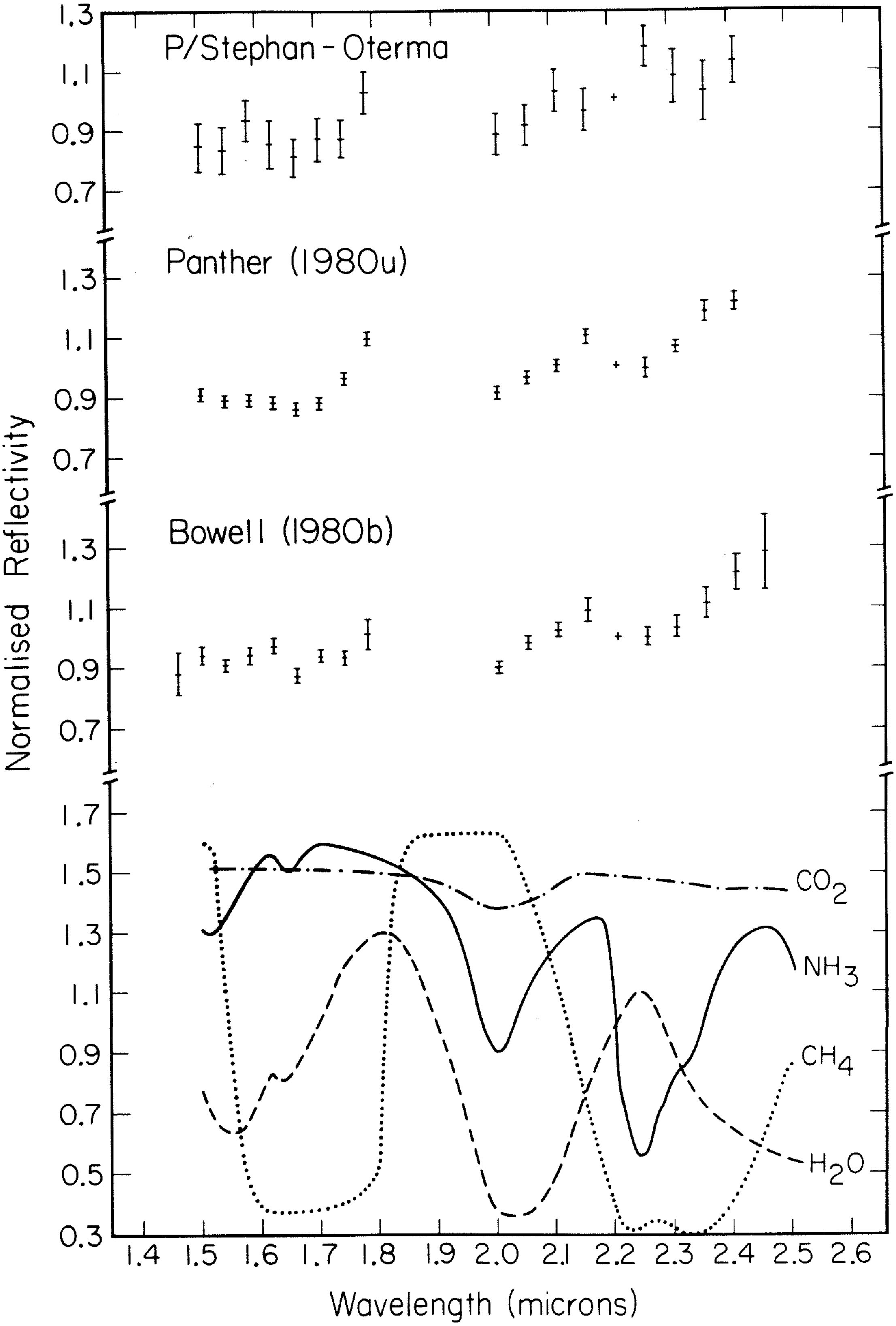

4. Broadband Infrared Wavelength Observations

Comets Panther and Bowell were observed through broadband infrared filters on the nights of UT April 14 and 15, 1981. Again the Palomar 5 m telescope was used. The filters employed had central wavelengths 1.2, 1.6, 2.2, 3.7, 4.8, 10 and 20 μm. The first five of these filters had fractional FWHM bandpasses of ~ 20%. The 10 and 20 μm filters had bandpasses of about 6 μm. A diaphragm of 4.4 arcsecond diameter was employed. The measurements were reduced to absolute flux densities by using observations of stars on the photometric system defined by Elias et al. (1982). The broadband data are summarized in Table 4 and are plotted in Figure 5. In the figure a broadband observation at 0.65 ± 0.1 μm, obtained by summing over an effective 4.4 arcsecond diameter diaphragm, has been added for comparison with the infrared data. This flux density, derived by comparison with the photometric standards of §2, was found to be 0.9 ± 0.1 mJy.

5. Interpretation of the Visual Data

In this section an attempt is made to use the appearances of the comets as seen in the PFUEI direct images and visual spectra to help define the properties of the three objects.

It may be noted that the visual data do not refer to the bare nuclei of the comets. Having typical radii of a few kilometers (Wyckoff, 1982) such nuclei would be observed as unresolved objects having geometric albedo cross-section products of less than about 10^7 m^2. No such objects are seen in any of the comets. Instead the light is scattered from their comae.

We take the strong continua in the visual spectra shown in Figure 3 to indicate that most of the light from the three comets is sunlight scattered from

Table 4

Broadband Infrared Measurements

λ (μm)	Panther Flux Density (mJy)	Bowell Flux Density (mJy)
1.2	12 ± 1	3.5 ± 0.3
1.6	12 ± 1	3.2 ± 0.2
2.2	8.4 ± 0.6	2.1 ± 0.2
3.7	8 ± 2	—
4.8	60 ± 20	—
10	870 ± 100	17 ± 2
20	2500 ± 600	400 ± 200

Figure 5. The logarithms of the broadband flux densities (in mJy) are plotted versus the central wavelengths (in μm). All observations were made with a 4.4 arcsecond diaphragm. The filter FWHM are indicated by horizontal bars. Continuous and dashed lines are blackbody fits to the reflected and thermal components of the two spectra. The broadband measurements were obtained on 4/14/81 and 4/15/81 with the 5 m telescope.

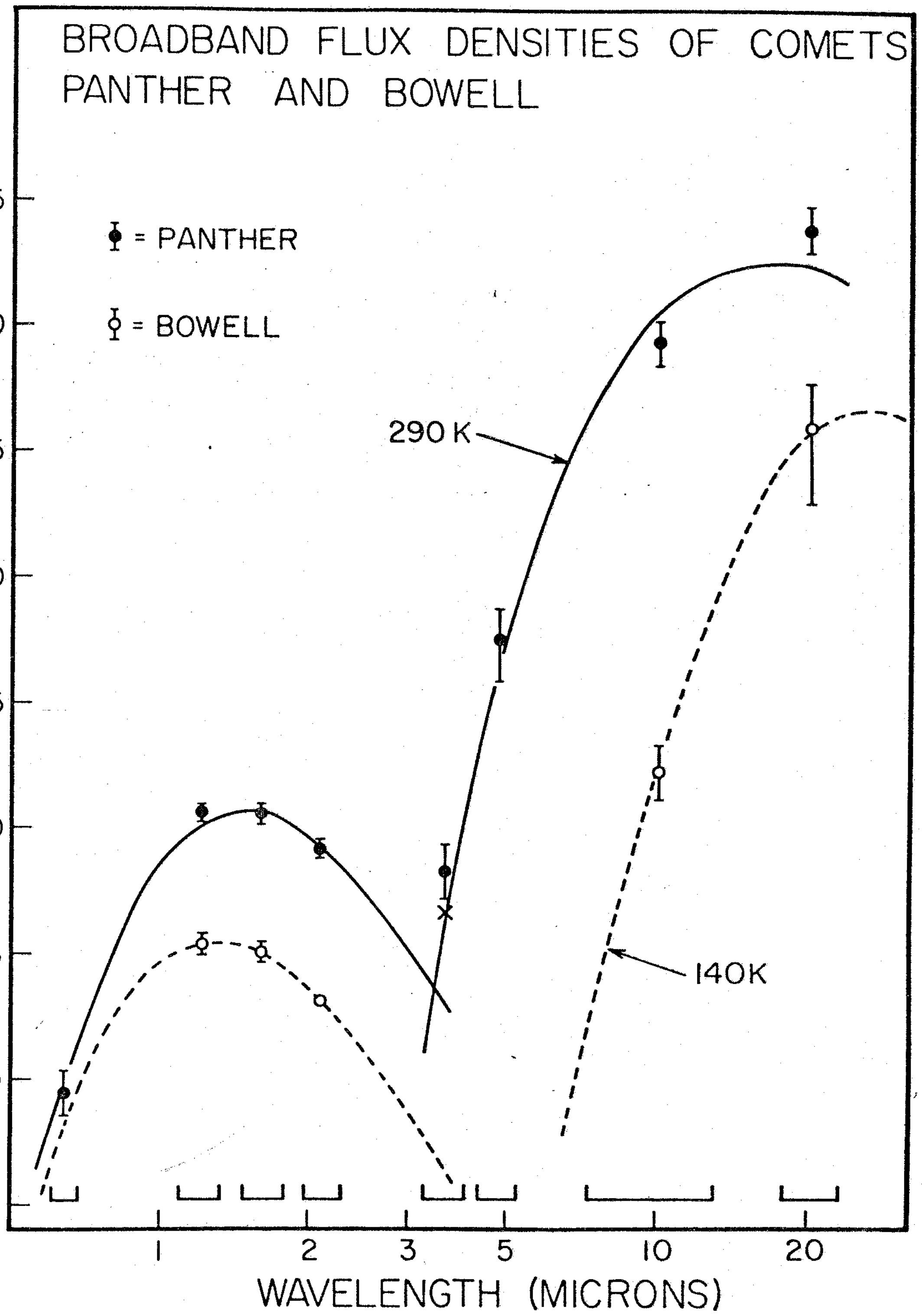
BROADBAND FLUX DENSITIES OF COMETS PANTHER AND BOWELL
● = PANTHER
○ = BOWELL
290 K
140K
log F_ν(mJy)
3.5
3.0
2.5
2.0
1.5
1.0
0.5
0.0
-0.5
1
2
3
5
10
20
WAVELENGTH (MICRONS)

solid particles. The emission bands and lines observed in comet Panther can be attributed to the C_2 and NH_2 radicals.

Comparisons of the observed logarithmic visual brightness profiles of the three comets with model calculations are physically revealing. In making such comparisons the parts of the profiles with $\log(p) \lesssim 0.4$ and with $(B - B_s) < 0.1\, B_s$ are ignored; here p is the angular separation, in arcseconds, between the photometric center of the coma and the line of sight and $B - B_s$ is the brightness of the coma above the sky brightness B_s. In the former region the observed profiles are distorted by the effects of atmospheric seeing while in the latter region errors in the choice of the sky brightness become significant.

In the simplest model, the coma comprises an isotropically expanding spherically symmetric and optically thin collection of constant size dust grains. In such a coma the grain number density n varies with radial distance from the center of the nucleus, r, according to $n \propto r^{-2}$ as a consequence of continuity. The coma surface brightness then varies as $B(p) \propto p^{-1}$. This result remains valid for an optically thin coma even for non-isotropic grain ejection provided the ejection is symmetric about the subsolar point on the nucleus and provided observations are made from small phase angles. Numerical integrations show that the first order effects of the distortion of the coma by solar radiation pressure do not alter the above result.

This very simple coma model is plotted in the upper part of Figure 1, where it is seen to provide a satisfactory fit to the observed brightness profile of P/Stephan-Oterma. The success of this simple model is taken to indicate that the coma of P/Stephan-Oterma, for $\log(p) > 0.4$, consists of a steadily expanding collection of grains each of constant radius. However at $\log(p) \lesssim 0.3$

the surface brightness rises considerably higher than the projected $B(p) \propto p^{-1}$ variation. This excess cannot be a result of the seeing: the smearing action of the seeing would instead tend to depress the observed brightness. The central brightness excess must result from an excess grain cross section in the region around the nucleus. The most likely explanation of the brightness excess which is consistent with its observed persistence (at least five months) and with its finite width is that it is an ice grain halo (Delsemme and Miller, 1971). Individual ice grains ejected from the nucleus by gas drag sublimate in the sunlight and all but disappear by the time they have traveled a few hundred kilometers. Refractory grains which may be incorporated within the ice grains are 'released' at the edge of the ice grain halo and travel outward to populate the isotropic region observed at $\log(p) > 0.4$. The persistence of the ice grain halo is due to its continual replenishment by sublimation of the nucleus. Dirty water ice grains of initial radius $a(0) \sim 100\ \mu\text{m}$ would indeed have lifetimes of a few hours, permitting them to travel the observed 400 km radius of the halo (Hanner, 1980).

Attempts to fit the profiles of comets Bowell and Panther with the simple isotropic expansion model are unsatisfactory. We therefore attempt to reproduce the observed profiles with a model involving sublimating grains following the approach of Delsemme and Miller (1971). The grain radius at distance r from the nucleus is put equal to

$$a(r) = a(0)\left[1 - r/r_H\right] \tag{1}$$

where $a(0)$ is the initial radius of the grain and r_H is the radius of the ice grain halo. Equation (1) merely implies that the grain size decreases at a constant rate, approximately consistent with grain sublimation for instance, or with sputtering erosion. More complicated alternatives to equation (1) could be substituted but would be difficult to justify.

By integrating along the line of sight it may be shown that equation (1) leads to a coma surface brightness

$$B(\gamma) = A\left\{\frac{\arccos\gamma}{\gamma} - 2\ln\left[\frac{1 + \left(1 - \gamma^2\right)^{1/2}}{\gamma}\right] + \left[1 - \gamma^2\right]^{1/2}\right\} \qquad (2)$$

where $\gamma = p/p_H$, $0 < \gamma \leq 1$, p_H is the angular radius of the ice grain halo in arcseconds and A is a constant.

Equation (2) has been fitted to the observed profiles by varying p_H and the constant of proportionality. The best fit lines are plotted in the middle and lower parts of Figure 1. A fit to P/Stephan-Oterma is indistinguishable from the fit obtained using the simple model, provided the ice grain halo radius is $p_H \gtrsim 10^4$ arcsecond ($r_H \gtrsim 5 \times 10^9$ m). In the case of comet Panther, the fit achieved with equation (2) is entirely satisfactory (see Fig. 1). The ice grain halo radius deduced from the fit is $p_H = 320$ arcseconds ($r_H = 5 \times 10^8$ m). The good fit strongly suggests that the coma around Panther consists of an expanding halo of grains composed of a sublimating volatile material.

The fit to the profile of comet Bowell is less pleasing (see Fig. 1). The surface brightness of this comet decreases much more rapidly with p than would that of an ice grain halo. We do not understand the surface brightness profile of comet Bowell. Sekanina (1982) has suggested that the coma of Bowell in fact comprises a swarm of large particles *in orbit* about the nucleus in which case the ice grain halo model would be inapplicable. The present data neither confirm nor deny this contention and it would seem prudent to reserve judgment on the nature of the coma particles until better observations and/or models are available.

It has already been noted that solar radiation pressure would not substantially affect the near-nucleus brightness profiles of the cometary comae. However another argument concerning the effects of radiation pressure may be used to constrain estimates of the grain sizes. To first order the effect of a radiation pressure induced acceleration w would be to move an initially circular dust shell radially back a distance $l \sim \frac{1}{2} w \left[\frac{r}{v}\right]^2$ where r is the radius of the dust shell in question and v is the initial speed of ejection of the dust grains into the coma. The distances l and r may be measured from the PFUEI images. The velocity v may be estimated from Bobrovnikoff's (1954) empirical relation

$$v\,(ms^{-1}) \sim 500\ R^{-0.6} \tag{3}$$

where R is the heliocentric distance measured in AU. Since equation (3) describes the motions of shocks in the gaseous components of comae we may confidently use it to provide *upper limits* to the speeds of solid grains and so upper limits to the radiation pressure induced accelerations. Values of l, R and v are listed in Table 5, together with the resultant accelerations w. The ratio $\beta = w/g_{\odot}$ with $g_{\odot}$ the local acceleration due to solar gravity is also listed for each comet.

The ratio β depends upon the grain radius a, on the mass density ρ and on the grain complex refractive index $m = n - ik$. Values of β versus a have been computed for a number of common solar system materials by Burns et al. (1979). From their Figure 1 it may be observed that the upper limits to β found for comets Panther and Stephan-Oterma rule out the substantial presence of iron or magnetite grains between about 0.02 and 0.4 μm radius. More specific statements concerning the particle sizes cannot be made from the visual data

Table 5

Measurements of Coma Distortion

Parameter (1)	Stephan-Oterma	Bowell	Panther
l (2) (1)	1.5×10^6	3.7×10^7	1.6×10^6
r (m)	1.7×10^7	4.7×10^7	$1.8\ 10^7$
R (AU)	1.83	4.90	2.10
v (ms^{-1}) (3)	350	190	320
w (ms^{-2})	$< 1.3 \times 10^{-3}$	$< 1.2 \times 10^{-3}$	$< 1.0 \times 10^{-3}$
$g_{\odot}$ (ms^{-2})	1.8×10^{-3}	2.5×10^{-4}	1.35×10^{-3}
β	< 0.7	< 5	< 0.8

(1) See section 5.

(2) Projection factor included.

(3) Computed with equation (3).

alone.

6. Interpretation of the Broadband Infrared Data

In Figure 5 the reflected and thermally radiated components of the radiation from comets Panther and Bowell are clearly separated. At $\lambda \lesssim 3\ \mu m$ the measured flux densities are due to sunlight scattered by the coma grains. At $\lambda \gtrsim 4\ \mu m$ the measured radiation is primarily due to sunlight absorbed and then re-radiated by the grains. The measurement of comet Panther at $3.7\ \mu m$ represents mostly thermal radiation but contains a significant component due to reflected solar radiation. By fitting a Planck function to the points with $\lambda < 3\ \mu m$ and extrapolating to $3.7\ \mu m$, the reflected solar radiation component was estimated to be 3 mJy leaving 5 mJy of thermal emission. The effective blackbody temperature of the reflected radiation, ~ 3000 K, is forced by the low flux density at $0.65\ \mu m$, and implies an intrinsic redness of the grains. The $3.7\ \mu m$ measurement corrected for the reflected component is indicated in Figure 5 by a cross.

Planck functions were fitted to the thermal broadband measurements of the two comets. The resulting best-fits are shown in the figure. There is no evidence for the $10\ \mu m$ emission normally associated with the presence of silicates in comets. However at the relatively large heliocentric distances of comets Panther and Bowell the emission is not expected. In the case of comet Bowell the best fit temperature is estimated to be 140 ± 10 K, where the uncertainty results mostly from the uncertainty on the $20\ \mu m$ data point. This may be compared to the temperature expected for a blackbody at the same 4.6 AU heliocentric distance, namely $T_{BB} = 130$ K. The two temperatures are in agreement. However, the best-fit temperature for comet Panther is 290 ± 15 K which is ~ 50% higher than the equilibrium blackbody temperature $T_{BB} = 210$ K at $R = 1.8$ AU.

This detection of elevated grain temperature can be used to limit the range of grain properties in the coma of comet Panther by the following method. The elevated grain temperature implies that the emissivities of the grains must decrease with increasing wavelength. The specific form of the wavelength dependence can be found from the solution of the thermal equilibrium condition for individual grains. If the grains can be treated as spheroidal Mie particles the thermal equilibrium condition is

$$\int_0^\infty Q_a(a,\lambda,m)\, F_\odot(\lambda)\, d\lambda = 4\pi R^2 \int_0^\infty Q_a(a,\lambda,m)\, B(\lambda,T)\, d\lambda \qquad (4)$$

where $Q_a(a,\lambda,m)$ is the absorption efficiency of a grain of radius a and complex refractive index m at wavelength λ, $F_\odot(\lambda)$ is the solar flux density at a heliocentric distance of 1 AU, R is the heliocentric distance of the grain in AU and $B(\lambda,T)$ is the Planck function at temperature T. Equation (4) was solved iteratively for the $Q_a(a,\lambda,m)$. To facilitate the evaluation of equation (4), the solar flux density $F_\odot(\lambda)$ was approximated by a 5890 K blackbody. Because the refractive index m of the grain material is unknown, the equation was solved for a range of complex indices of astrophysical interest. After each iteration the Mie particle emission spectrum was fitted to the long wavelength broadband measurements in order to compute the new best-fit temperature. The iterations were halted when the change in grain temperature between successive iterations became less than the temperature uncertainty due to the errors on the broadband measurements themselves. Usually three iterations were found to be sufficient. The corresponding size uncertainties typically amount to a few tenths of a micron. For complex refractive indices $m = n - ik$ with n in the range 1.1

to 1.5 and k in the range 0.07 to 0.3, the equilibrium grain radii were found to lie in the range from 2 to 4 μm. The physical temperatures corresponding to these particles were close to 250 K.

Particles with radii around 2-4 μm have small β values which are consistent with the upper limit imposed by the visual data. At visual and near infrared wavelengths the particles have $x = 2\pi a/\lambda >> 1$ and would thus be considered large in the classical sense. In the 10 μm thermal emission region the particles have $x \sim 1$.

It would not be reasonable to attempt to reach more specific conclusions than those above since a) the cometary grains are probably not well approximated by Mie spheroids; b) the size distribution of the grains is unknown; c) the complex refractive indices of the grains are unknown, and; d) the quality of the broadband data does not permit a study significantly more detailed than the present one.

The observed thermal flux densities can be used to compute the cross section present in the coma from the absorption efficiency $Q_a(a,\lambda,m)$. Under the safe assumption of an optically thin coma the total cross section present within a 4.4 arcsecond diameter diaphragm (corresponding to 5.8×10^6 m at the comet) is $(1.0 \pm 0.2) \times 10^8$ m^2. The observed near infrared broadband measurements then give the near infrared albedo as 0.14 ± 0.05.

It may be noted that the broadband observations permit an estimate of the total mass of the dust in the coma of comet Panther. The total cross section was found to be $\sim 1 \times 10^8$ m^2. With a grain radius of 4 μm some 2×10^{18} grains were present in the coma. If the grain density was 10^3 kg m^{-3} the total mass of the grains within a region subtending 5.6×10^6 m centered on the nucleus was 5×10^5 kg. From equation (3) an upper limit to the expansion speed of the grains from the nucleus of 350 ms^{-1} may be obtained. This implies the time within the diaphragm to be $> 8 \times 10^3$ s and an upper limit to the mean grain mass production rate to be approximately 60 kg s^{-1}. Averaged over the surface of a 10^3 m radius nucleus this is equivalent to an upper limit to the surface recession rate of 5×10^{-9} ms^{-1}. This rate could be sustained for years before substantial depletion of the upper few meters of the nucleus occurred.

For comet Bowell the observation that the grain temperature of 140 ± 10 K is consistent with the local blackbody temperature of 130 K suggests that $Q_a(a,\lambda,m) \equiv 1$ in the 1 to 20 μm wavelength region. If this is correct a total cross section of $(3 \pm 1) \times 10^8$ m^2 is found to lie within a 4.4 arcsecond (1.16×10^7 m) diaphragm. The visual and near infrared broadband data then lead to an estimated 1 to 2 μm geometric albedo of 0.14 ± 0.05, within the same diaphragm. That the absorption efficiencies are close to unity suggests that the mean grain size is even larger than that in comet Panther. By taking $a \gtrsim 10$ μm we find the total mass within the projected diaphragm to be $\gtrsim 4 \times 10^6$ kg. The estimated mass loss rate from the comet is then $\lesssim 70$ kg s^{-1}.

Broadband infrared observations of comet P/Stephan-Oterma have been reported by Veeder and Hanner (1981). They interpret their observations to rule out the presence of large numbers of submicron grains and grains of radius > 10 μm.

7. Interpretation of the Infrared Spectra

In general the appearances of the near infrared spectra of all three comets may result from the presence of both solid grains and/or free gaseous molecules and radicals in the cometary comae. We believe that solid grains are primarily responsible for the near infrared spectral features in comets Panther and Bowell. Firstly, the two comets exhibit widely different degrees of gaseous emission in the visual yet display identical near infrared features; the infrared features are therefore not from gas. Secondly, the features are much broader than would be expected from a gaseous source (FWHM ~ 0.2 μm) suggesting that they originate in solid particles. This will be assumed through the remainder of the paper.

The near infrared spectrum of the grains in the comae will depend upon the composition and crystallographic state of the grain material and on the grain size, temperature and shape (Kieffer, 1968). Effects due to multiple scattering between grains should be negligible since the comae are optically thin. In principle, grain size dependent scattering effects could produce substantial variations of reflectivity with wavelength, particularly if $x \sim 1$. However several arguments suggest that such scattering effects are small:

1. The broadband near infrared and thermal infrared data suggest particle sizes in the range 2 to 4 μm for comet Panther and still larger sizes for comet Bowell.
2. Cometary grains seem to be highly irregular in shape (Brownlee, 1978) and the irregularities would tend to smooth-out reflectivity effects due to scattering.
3. The distribution of grain sizes would likewise degrade strong reflectivity effects due to scattering.

We therefore proceed on the basis that the shapes of the near infrared spectra of the three comets result from the compositions of solid grains in the comae of these objects. Fine details of the spectra, in particular the depths of the absorption features, may reflect the influence of particle size and shape, however.

The near infrared spectrum of P/Stephan-Oterma gives no evidence for the 2 μm absorption band of water ice (see Figure 4). In order to place quantitative limits to the possible contribution of water ice to the P/Stephan-Oterma spectrum, elementary additive mixing calculations were performed. To simulate the reflective properties of refractory dust, a linear reddened continuum was added to the water ice spectrum in various proportions. The slope of the continuum and the proportion of the dust relative to the water ice were varied until χ^2 was minimized between the model and the P/Stephan-Oterma spectra. It was found that not more than 20% of the near infrared photons from the comet can have passed through large pure water ice grains. In view of the prevalence of water ice in all viable comet models, and especially in view of the suggestion from the visual data of a halo of subliming grains close to the nucleus of this comet, the absence of the strong water ice absorption seems initially surprising. The possibility that water ice is totally absent from the comet is consistent with the infrared data alone. However, the visual spectroscopic detection of H_2O^+ in this comet by Cochran et al. (1981) and the variation of the integrated brightness of the comet with heliocentric distance both suggest that water ice is present in the nucleus. The albedo of ice grains is mostly determined by refraction through their interiors, rather than by reflection from their surfaces. For this reason a small quantity of an absorbing contaminant in grains may suppress the overtones of fundamental vibration bands, especially those weaker features occurring at short wavelengths (Warren and Wiscombe, 1981). The contamination of ice grains by small dust particles is a natural consequence of the standard comet nucleus models in which the two are taken to be closely mixed. Additionally, model calculations of the sublimation of *dirty* water ice grains of initial radius $a(0) \sim 100\ \mu m$ suggest an ice grain halo radius of $\lesssim 10^6$ m, consistent with the observed value 4×10^5 m. Pure ice grains would produce a much larger halo than is observed (Hanner, 1980) as a result of the small absorptivity of ice in the visual region. Finally, the redness of the coma of comet P/Stephan-Oterma is contrary to the blueness of pure snows (O'Brien and Munis, 1975), but is similar to the redness of many refractory materials where the color is often due to the Fe^{2+} ion. This again suggests contamination but it could also be a particle size effect.

In comets Bowell and Panther the absence of the water ice absorptions cannot be due to masking by a neutral absorbing contaminant since (other) discrete spectral features *are* present. It is implausible that a contaminant which is able to mask the strong water absorptions would simultaneously be unable to hide those of another molecule. Presumably the non-appearance of the water ice signature in the Bowell and Panther spectra shows that water ice is truly deficient in the coma grains of these comets. The results of additive mixing calculations indicate that not more than about 10% of the sunlight reflected from comets Bowell and Panther has passed through large pure water ice grains.

Attempts to identify the spectra with those of other solar system bodies have all failed. Some similarity to asteroid and meteorite reflectivities might be expected since in most comets an appreciable quantity of dust is present; typically half the cometary mass is in dust (Wyckoff, 1982). The spectral features are not similar to any seen in the asteroids, the planets, planetary satellites or in terrestrial or meteorite samples (Hunt and Salisbury, 1970,1971; Kieffer and Smythe, 1974; Smythe, 1975; Fink et al., 1976; Larson et al., 1979;

Clark and McCord, 1980; Lebofsky et al., 1981). A comparison with spectra of the interstellar medium and of objects in the cool interiors of molecular clouds has also proved fruitless. Similarity to interstellar dust spectra might be expected since, according to some workers (e.g., Greenberg, 1980), comets may be aggregates of unaltered interstellar grains.

In Figure 4 the comet spectra are compared with those of methane, ammonia, carbon dioxide and water ices. Of these simple (and cosmically important) ices, the best match is with the wavelengths of overtones of vibration bands of ammonia. However while there are general similarities with the ammonia ice spectrum, major differences exist in detail. Most importantly, the reflectivity minimum at 2.22 ± 0.02 μm in the comet spectra is significantly short of the ammonia minimum at 2.30 μm (Slobodkin et al., 1978). Kieffer and Smythe (1974) place this band at 2.27 μm in 500 μm grains at a temperature of 77 K. Slobodkin et al. showed that the wavelengths of the above spectral features are not significantly altered by changing the temperature of the ammonia reflecting surface, neither do they depend appreciably on the crystallographic phase of the ammonia though a fundamental absorption at ~ 3.1 μm does. In addition an absorption centered at 1.54 μm in the ammonia spectrum is completely absent from the comet spectra. The relative strengths of the ammonia absorption features do exhibit a dependence on the sample temperature and on the rate of crystal formation. At a sample temperature of 85 K, for instance, the 1.54 μm feature is all but absent, while the 2.04 and 2.30 μm features remain strong. Unfortunately the temperature of the grains in comet Panther (~ 250 K) is much higher than the 80 K at which the 1.54 μm absorption disappears. Hence based on the laboratory spectra it seems unlikely that temperature or other effects could be responsible for the differences between the ammonia and the comet spectra. The spectrum of ammonia hydrate ($NH_3 \cdot H_2O$) includes a strong contribution from H_2O and is therefore inconsistent with the comet spectra. Conceivably, if ammonia *is* present in the comets, blends with spectral bands of other materials might cause the band centers to shift to the observed positions. However we cannot find any convincing candidate materials which reproduce the spectra of comets Panther or Bowell.

8. Discussion

The existence and break-up of ammonia molecules in Panther would be consistent with the visual spectra of this object which show numerous lines due to NH_2. However, it is not clear that the solid grains in the comae of either of the comets can be composed only of ammonia ice since the lifetimes of such grains to sublimation would be very short. For instance at $R \sim 5$ AU, a distance similar to that of comet Bowell at the time of observation, the sublimation mass flux of NH_3 ice having a Bond albedo 0.5 would be $10^{-5.5}$ kg m^{-2} s^{-1}. With a density of 10^3 kg m^{-3}, even a 100 μm grain would have a lifetime to sublimation of only $10^{4.5}$ s. To travel $\sim 10^8$ m from the nucleus to the edge of the coma such a grain would have to be ejected from the nucleus at a speed $\sim 10^{3.5}$ ms^{-1}. Not only is this in excess of the speed suggested by the application of equation 3, it is ten times the sound speed in ammonia gas at the local blackbody temperature. In short, small ammonia grains would sublimate away too quickly to be detected and large grains would be propelled from the nucleus too slowly to reach far into the coma. These results become even more restrictive when more absorbing grains or smaller heliocentric distances are considered.

An alternative is that the observed absorptions do indeed result from overtones of vibrational transitions of the N-H bond but from within a different and less volatile molecule. Photodissociation of the molecule could still give rise to the NH_2 radical seen in the visual spectra. In addition to ammonia the interstellar medium is known to contain molecules of formamide and methyl amine both of which include NH_2 and could be present in comets. Clearly the present data do not permit a unique identification of the material responsible for the near infrared spectral features of comets Bowell and Panther. However many materials are ruled-out by the data, most importantly water and the simple ices.

According to some workers the initially simple chemistry of the comet nuclei (mostly H_2O, CO_2, NH_3) is modified by interaction with the interstellar UV radiation and with the flux of galactic cosmic rays. Although the UV and cosmic ray fluxes are very low, the 4.5×10^9 year residence time of comets in the Oort cloud is sufficient to permit substantial concentrations of new molecules and radicals to build up. The mass of material involved in cosmic-ray reprocessing need not be large. Probably only the outer most few meters of the nucleus would undergo significant chemical transformation. Laboratory simulations of this chemical reprocessing have been performed by Moore (1981). Near infrared spectra of the modified chemicals have been taken. Unfortunately, these spectra exist only for $\lambda > 3\ \mu m$ so that a comparison with our comet data is presently impossible (B. Donn, 1981, private communication).

It may be that the near infrared spectra of the comets Bowell and Panther record the presence of complex molecules on grains of a few μm radius in their comae. In fact, the hypothesis that 'new' comets have unstable mantles of such molecules which are lost soon after the first perihelion is completely consistent with both the visual *and* the infrared observations of all three comets. Comets Bowell and Panther are both thought to be making their first approaches to the Sun as judged from their orbital characteristics. Both comets became active at large heliocentric distances. Comet Bowell possessed an extended dust coma at $R = 7$ AU and comet Panther has likewise been strongly active at large R. The similarities between these two comets in terms of their excess activity extend to their near infrared reflection spectra. On the other hand, comet P/Stephan-Oterma was relatively inactive at *smaller* R, had a more simple photometric profile and possibly a different near infrared reflection spectrum. It is tempting to note that P/Stephan-Oterma is an older periodic comet which might easily have lost any supervolatile mantle it may once have possessed. It will be necessary to pursue the types of observation reported in the present work to encompass a larger sample of comets.

9. Summary

The observed properties of the comets P/Stephan-Oterma, Panther and Bowell in the 0.5-3.0 μm region are all explainable by scattering of solar radiation from solid grains in their comae.

The visual surface brightness profile of comet P/Stephan-Oterma consists of two parts: a bright central region 4×10^5 m in radius is interpreted to be a halo of sublimating grains while an extended outer region is consistent with the presence of an isotropically expanding cloud of refractory grains. The near infrared spectrum of the comet is featureless within the uncertainties of the measurements.

The visual surface brightness profile of comet Panther suggests the presence of sublimating grains in a halo having a radius 5×10^8 m centered on the nucleus. The grains in the central region of the coma have, depending on the actual value of the grain refractive index, a geometric albedo of 0.14 ± 0.05 and mean radii in the range 2-4 μm. At a heliocentric distance $R \sim 1.9$ AU the grain mass loss rate from comet Panther was $\lesssim 60$ kgs^{-1}. The 1.4-2.4 μm spectrum of comet Panther displays spectral features which are similar to features observed in laboratory spectra of solid NH_3, although there are significant differences. Micron sized NH_3 grains would be unstable to sublimation in the coma of comet Panther and therefore the majority of the grains cannot consist of NH_3. The 2-4 μm grains most likely contain molecules which incorporate the N–H bond but which are more complex and less volatile than NH_3. Such molecules might be produced in the grains by cosmic ray reprocessing.

The visual surface brightness profile of comet Bowell cannot be readily understood in terms of the simple models employed in the present study. The grains in comet Bowell have a similar albedo to those in comet Panther but have a larger mean radius (probably $\gtrsim 10$ μm). At $R \sim 4.5$ AU the grain mass loss rate was $\lesssim 70$ kgs^{-1}. Near infrared spectral features identical to those seen in comet Panther similarly suggest the presence of a molecule which incorporates the N–H bond.

Acknowledgements

We are grateful to J. Westphal and J. Gunn for permission to use the PFUEI and to J. Carrasco, S. Grollix, J. Hoessel, C. Porco, S. Staples and G. Veeder for assistance with the observations. We thank J. Westphal and E. Ney for careful reading of the manuscript. D. Yeomans kindly provided ephemerides for the comets. This research was supported by NASA and NSF grants.

References

A'Hearn, M.F., Dwek, E. and Tokunaga, A.T. (1981). *Ap. J.* **248**, L147-151.

Arveson, J.C., Griffin, R.N., and Pearson, B.D. (1969). *Appl. Opt* **8**, 2215-2232.

Becklin, E.E., and Westphal, J.A. (1966). *Ap. J.* **145**, 445-453.

Bobrovnikoff, N. (1954). *Astron. J.* **59**, 351-358.

Brownlee, D.E. (1978). in *Cosmic Dust*, edited by J.A.M. McDonnell, Wiley-Interscience.

Burns, J.A., Lamy, P.L., and Soter, S. (1979). *Icarus* **40**, 1-48.

Clark, R.N. and McCord, T.B. (1980). *Icarus* **43**, 161-168.

Cochran, A.L. and Barker, E.S. (1981). Comets: Gases, Ices, Grains and Plasma, IAU Colloquium 61, Tucson, Arizona.

Cruikshank, D.P. (1980). *Icarus* **41**, 246-258.

Delsemme, A.H. and Miller, D.C. (1970). *Planet. Space Sci.* **18**, 717-730.

Delsemme, A.H. and Miller, D.C. (1971). *Planet. Space Sci.* **19**, 1229-1257.

Elias, J., Frogel, J., Matthews, K. and Neugebauer, G. (1982), submitted to *Astron. J.*

Fink, U., Larson, H.P., Gautier, T.N. and Treffers, R.R. (1976). *Ap. J.* **207**, L63-67.

Fink, U. and Sill, G. (1981). Abstract of a paper delivered at IAU Colloquium #61, Comets: Gases, Ices, Grains and Plasma, held in Tucson, Arizona, 1981.

Greenberg, J.M. (1976). *Astrophys. and Space Sci* **39**, 9-18.

Greenberg, J.M. (1980). I. Halliday and B.A. McIntosh (eds.), Solid Particles in the Solar System, IAU Symposium No. 90, 343-350. D. Reidel Publishing Company.

Gunn, J.E. and Westphal, J.A. (1981). *Proc. International Soc. Opt. Engineers* **290**, 16-23.

Hanner, M.S. (1980). I. Halliday and B.A. McIntosh (eds.), Solid Particles in the Solar System, IAU Symp. 90, 223-236. D. Reidel Publishing Company.

Hanner, M.S. (1981). *Icarus* **47**, 342-350.

Hasegawa, I., Nakano, S. and Yabushita, S. (1981). *Mon. Not. R. astr. Soc.* **196**, 45P-46P.

Hunt, G.R. and Salisbury, J.W. (1970). *Modern Geology* **1**, 283-300.

Hunt, G.R. and Salisbury, J.W. (1971). *Modern Geology* **2**, 23-30.

Kieffer, H.H. (1968). Thesis, California Institute of Technology.

Kieffer, H.H. and Smythe, W.D. (1974). *Icarus* **20**, 506-512.

Larson, H.P., Feierberg, M.A., Fink, U. and Smith, H.A. (1979). *Icarus* **39**, 257-271.

Lebofsky, L.A., Rieke, G.H. and Lebofsky, M.J. (1981). *Icarus* **46**, 169-174.

Moore, M.H. (1981). Ph.D. thesis, submitted to University of Maryland.

Ney, E.P. (1975). Published in The Study of Comets, Part 1, NASA SP-393.

O'Brien, H.W. and Munis, R.H. (1975). Cold Regions Research and Engineering Laboratory, Research Report 332.

O'Dell, C.R. (1971). *Ap. J.* **166**, 675-681.

Oishi, M., Kawara, K., Kobayashi, Y., Maihara, T., Noguchi, K., Okuda, H., Sato, S., Iijima, T., and Ono, T. (1978). *Pub. Astr. Soc. Japan*, **30**, 149.

Sekanina, Z. (1975). *Icarus* **25**, 218-238.

Sekanina, Z. (1982). *Ap. J.* **87**, 161-169.

Slobodkin, L.S., Buyakov, I.F., Cess, R.D. and Caldwell, J. (1978). *J. Quant. Spectrosc. Radiat. Trans.* **20**, 481-490.

Smythe, W.D. (1975). *Icarus* **24**, 421-427.

Thuan, T.X. and Gunn, J.E. (1976). *Pub. Astron. Soc. Pacific*, **86**, 543-547.

Veeder, G.J. and Hanner, M.S. (1981). *Icarus* **47**, 381-387.

Warren, S.G. and Wiscombe, (1981). *J. Atmos. Sci.* **37**, 2712-2745.

Wehinger, P.A., Wyckoff, S., Herbig, G., Herzberg, G. and Lew, H. (1974). *Ap. J. Lett.* **190**, L43.

Whipple, F.L. (1950). *Ap. J.* **111**, 375.

Whipple, F.L. (1951). *Ap. J.* **113**, 464.

Wyckoff, S. (1982). In *Comets*, L.L. Wilkening, Editor. University of Arizona Press, Tucson, Arizona.

Comet Bowell (1980b): Evidence for Non Steady-State Nucleus Outgassing

David C. Jewitt[1,2,3]

[1]Palomar Observatory, California Institute of Technology.

[2]Division of Geological and Planetary Sciences, California Institute of Technology, Pasadena, California 91125.

[3]Guest observer at the NASA-IRTF, Mauna Kea Observatory, University of Hawaii.

Contribution number 3847 of the Division of Geological and Planetary Sciences, California Institute of Technology, Pasadena, California 91125.

Abstract

An extensive series of observations of comet Bowell at optical and infrared wavelengths is summarized and interpreted in terms of a model of the outgassing of the nucleus. The observations indicate that the optical coma consists of large grains. The outer edge of the coma is expanding from the nucleus at 0.9 ± 0.2 ms^{-1}: extrapolation of the expansion suggests that the coma was ejected from the nucleus when the comet was at a heliocentric distance $R \sim 10$ AU. At this distance, water ice sublimation would be negligible. Models of the brightness of the comet as a function of R are compared with the measured brightness variation. Between $R = 5.3$ and 3.4 AU, the apparent cometary brightness changed by a factor of less than 20. Models which account for the equilibrium sublimation of volatiles from the nucleus predict much larger brightness variations. In particular, the models confirm that the sublimation of water ice does not control the activity of comet Bowell. The observations are consistent with the presence of an inert nucleus surrounded by a dissipating grain coma ejected impulsively at $R \sim 10$ AU. Strong OH production observed near $R = 3.4$ AU could be a result of the photodissociation of water molecules released from the coma grains by sublimation. However, near infrared spectra of the grains show no evidence for the presence of OH. Instead, several absorptions similar to the overtones of NH bond vibrations are observed. It is noted that the outgassing properties of the comet are similar to those of proton-bombarded laboratory ice specimens. Both the impulsive coma ejection and the peculiar near infrared spectrum may result from the presence of unstable compounds produced in the nucleus by cosmic ray bombardment. The activity of comet Bowell is quite unlike that exhibited by comets at small R, but may be representative of the properties of the distant comets.

1. Introduction

Comet Bowell (1980b) was discovered at the unusually large heliocentric distance, $R \approx 7$ AU (Bowell, 1980). The early discovery of the comet permitted the taking of several novel observations not usually attempted on comets because of the lack of fore-warning. Astrometric observations showed that the orbit was parabolic, within the uncertainties of measurement (Hasegawa et al., 1981). Comet Bowell has probably not previously entered the inner solar system. For this and other reasons the comet has proved to be of unusual interest.

Several observations of comet Bowell have been reported in the literature. Veeder and Hanner (1981) described broadband infrared measurements taken when the comet was at $R = 4.80$ AU. Their observations showed the coma to consist of dark solid grains. Jewitt et al. (1982, hereafter referred to as Paper I) confirmed these findings and discovered peculiar spectral features in the 1.4 to 2.4 μm wavelength range. In addition they estimated the solid grain mass loss rate to be ~ 70 kgs^{-1} at $R = 4.58$ AU and found that the mean grain size in the coma was greater than about ten microns — an order of magnitude larger than typical cometary grains. In the optical wavelength range the coma was found to have a steep surface brightness profile which could not be matched by either of two simple models. Recently, Campins et al. (1982) observed comet Bowell in the near infrared but were unable to detect the spectral features reported in Paper I as a result of the poor signal to noise in their spectrum. Lastly, Feldman et al. (1982) inferred an OH production rate $Q_{OH} \sim 3 \times 10^{28}$ s^{-1} at $R = 3.39$ AU from observations made with the IUE. The same observers inferred a CN production rate $Q_{CN} \sim 7 \times 10^{25}$ s^{-1} at the same R.

A model of comet Bowell was proposed by Sekanina (1982) in order to account for the unusually small variation of the total comet brightness with changing R and to account for the very small rate of change of the coma diameter, which he measured. In his model the comet nucleus was supposed to be essentially inert. The observed coma was said to consist of a cloud of solid particles gravitationally attached to the nucleus. Sekanina inferred a very large mean particle size ($a \gtrsim 500$ μm) from dynamical analysis of a weak tail present in the comet. Sekanina (who wrote his paper when the comet was at $R \sim 4$ AU), did not exclude the possibility of a small amount of outgassing from the nucleus near perihelion at $R = 3.36$ AU.

In this paper we present further optical (0.65 μm) and infrared (3 to 4 μm) observations of comet Bowell. We also present a simple model for the photometric behavior of the comet, which is consistent with all the photometric observations known to us. The model is in one sense the exact opposite of the one proposed by Sekanina. We do not believe that the nucleus has been inert but instead believe that the extensive coma was produced by impulsive outgassing of the nucleus at large R. Subsequent to the outburst the nucleus has been inactive, however.

2. Observations

2.1 Optical Wavelengths

Observations were obtained in the optical 0.5-0.9 μm region using the CCD camera and techniques described in Paper I. The observations were taken at the Cassegrainian focus of the Palomar 1.5 m telescope. A representative CCD image of comet Bowell taken at 0.65 μm wavelength is shown in Figure 1. The figure reveals both the bright, almost circularly symmetric coma of the comet

Figure 1. **Broadband CCD image of comet Bowell taken 3/ 25/82 at the** 1.5 **m** telescope of Palomar Observatory. Note roughly spherical coma and long, faint tail. The image is 440 arcsecond wide, corresponding to 1.1×10^9 m at the distance of the comet.

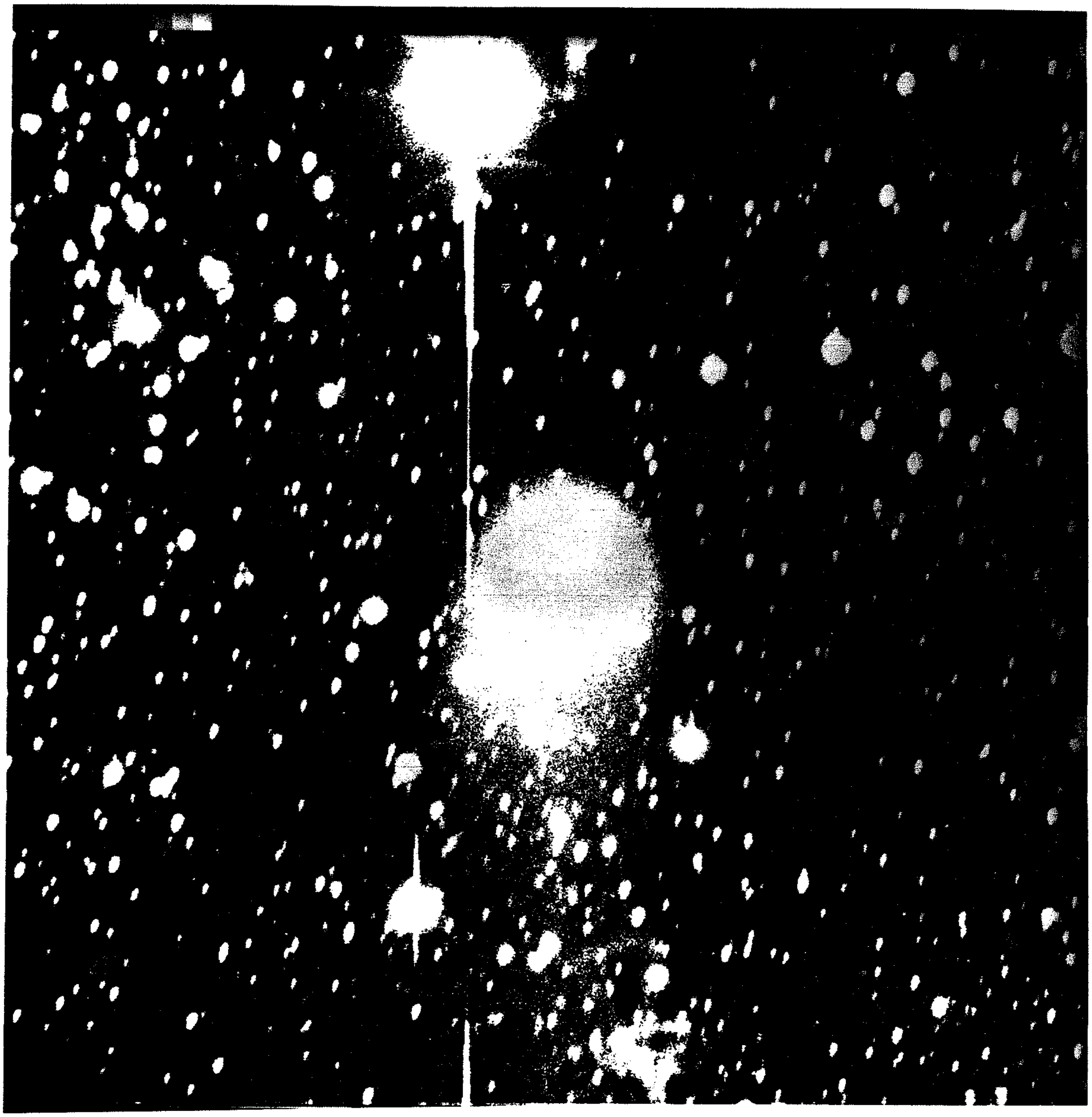

and the faint tail.

The CCD images were used to determine the radius of the coma by taking surface brightness plots perpendicular to the comet tail. The extent of the coma was taken to result from the component of the ejection velocity of the grains normal to the comet orbit plane. Since the comet orbit was almost coplanar with the ecliptic, the extent of the coma in the measured direction could not be appreciably influenced by solar radiation pressure. As a result of the ever steepening surface brightness profile near the edge of the coma, it was possible to obtain a good measurement of the coma radius by extrapolation of the observed surface brightness. The measured radii, corrected to $\Delta = 1$, have been plotted in Figure 2 as a function of Julian Day Number. The figure shows that the coma radius is a linearly increasing function of time. The slope of the least squares fit straight line is

$$v = 0.9 \pm 0.2\ \mathrm{ms}^{-1} \tag{1}$$

which is the best estimate of the coma expansion rate. We assume that this is also the speed of ejection of the optically important grains in the coma. By extrapolation, the coma is found to have had zero radius at

$$\mathrm{JD}(0) = 2443760 \pm 700 \tag{2}$$

corresponding to a period centered on September 1978. At this time, about a year before discovery, the comet was at heliocentric distance $R \sim 10$ AU. The observed expansion of the coma provides strong evidence for the initiation of activity on the comet nucleus at large R.

2.2 Infrared Wavelengths

Observations in the 3-4 μm region were taken with the 3 m NASA Infrared

Figure 2. The apparent radius of the coma of comet Bowell is shown as a function of time. All measurements were taken from CCD images. Geometric dependence has been removed by scaling all measurements to a unit geocentric distance. Also shown are the heliocentric distance R(AU) and the linear radius of the coma. The line is the least squares fit to the data, and indicates a significant but slow coma expansion.

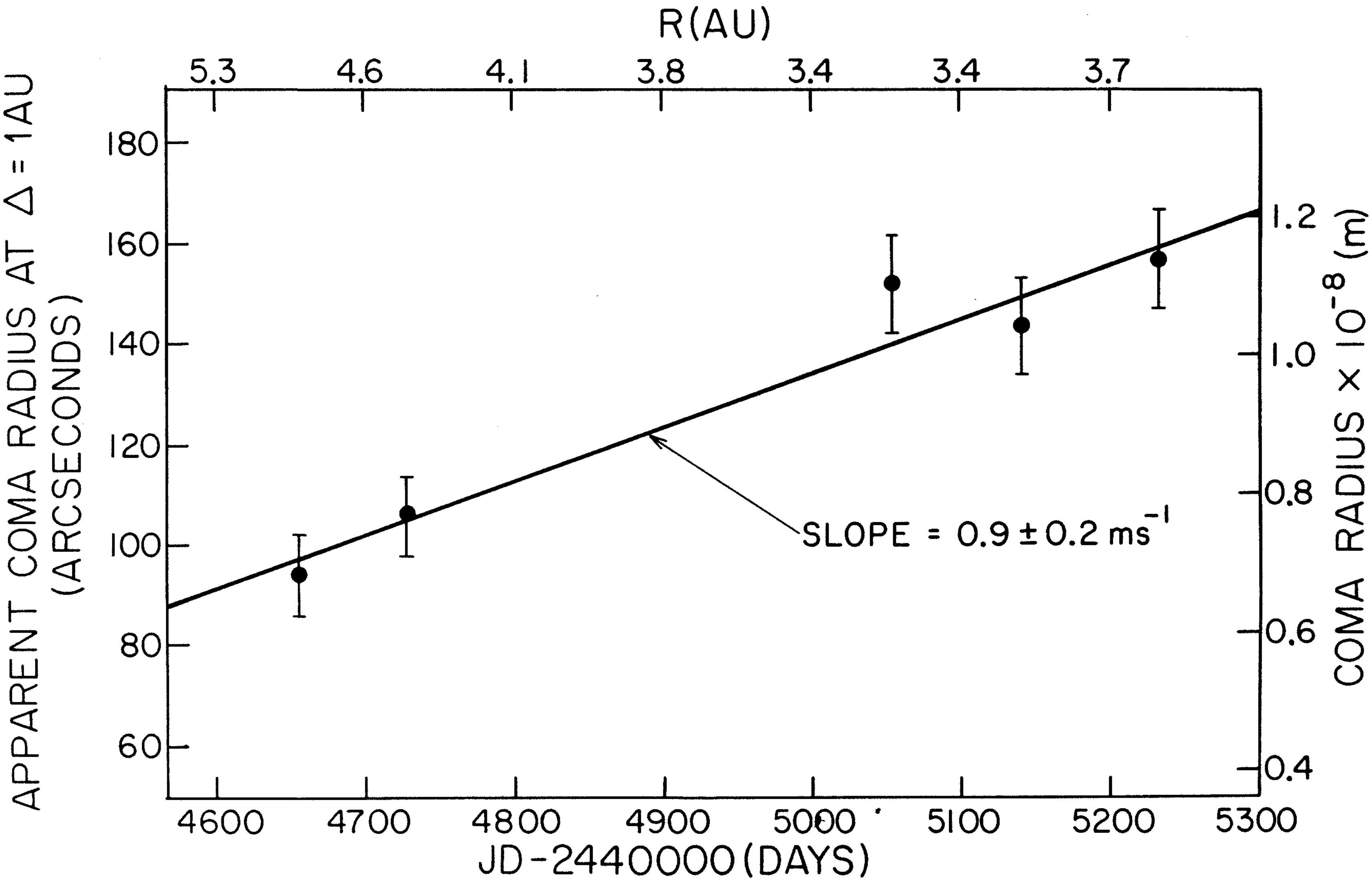
R(AU)
5.3
4.6
4.1
3.8
3.4
3.4
3.7
APPARENT COMA RADIUS AT Δ = 1AU (ARCSECONDS)
180
160
140
120
100
80
60
COMA RADIUS × 10^{-8} (m)
1.2
1.0
0.8
0.6
0.4
SLOPE = 0.9 ± 0.2 ms^{-1}
4600
4700
4800
4900
5000
5100
5200
5300
JD-2440000 (DAYS)

Telescope Facility (IRTF) at Mauna Kea Observatory from UT May 27 to UT May 29, 1982, inclusive. An InSb detector, cooled to liquid helium temperatures, was used at the f/30 Cassegrainian focus. A diaphragm of 8 arcsecond projected diameter was used with a beam chopping amplitude of 10 arcsecond in declination. The atmospheric seeing was at all times very small compared to the diaphragm size. Comet Bowell was found to be too faint to permit the recording of a complete 3 to 4 μm circular variable filter (CVF) spectrum. In addition the comet was projected against the galactic plane at the time of observation, causing field star interference to be a major problem. Consequently, only broadband J, H, K, L flux densities and a single 3.05 ± 0.06 μm CVF flux density were measured.

To detect the presence of field star contamination in the chopped beams the J magnitude was monitored as a function of time throughout the observing periods. Brief excursions from the steady state J magnitude were taken as evidence that one or more field stars were present in the beams. In addition we visually checked the beams for stars using the TV guider on the IRTF. Approximately half of the observations were rejected on the basis of these two tests. We found these techniques to be especially valuable during the long integrations at L and 3.05 μm CVF wavelengths.

The comet measurements were calibrated by taking repeated observations of the three stars BS 4689, BS 5409 and 16 CygB. The first two stars are broadband standards on the MKO IR standard list and the third is a type G3V; the latter is useful as a nearly solar type star. Empirical extinction coefficients were determined for the J, H, K and L filters by taking observations at a range of airmasses. Typical airmass differences between the calibration stars and comet Bowell were only 0.1 to 0.2. From long series of standard star observations the photometric stability was found to be better than 3% on each night. The estimated uncertainties accrued in the J, H, K and L measurements of comet Bowell amount to 5%. The measurement uncertainty at 3.05 μm has been estimated by taking the weighted mean of four independent integrations, and amounts to about 30%. Table I contains a summary of the computed magnitude and reflectivity of comet Bowell at each wavelength. The reflectivity has been plotted as a function of wavelength in Figure 3, where observations reported in Paper I are also shown.

The J magnitudes of comet Bowell are listed in Table II. The table contains the following information:

Column 1	JD, the Julian Day Number of the observation minus 2440000.
Column 2	R (AU), the heliocentric distance of the comet at the time of observation.
Column 3	Δ (AU), the geocentric distance of the comet at the time of observation.
Column 4	α (degrees), the phase angle of the comet.
Column 5	J, the measured J magnitude of the comet.
Column 6	φ (arcsecond), the projected diameter of the diaphragm within which J was measured.
Column 7	the beam chop amplitude (arcseconds) and direction of chop in the plane of the sky.
Column 8	ΔJ_1, the magnitude correction for diaphragm size. The correction is to a 10 arcsecond diameter diaphragm and was computed assuming that the coma integrated brightness follows $B(\varphi) \propto \varphi$ (e.g., see Paper I).
Column 9	ΔJ_2, the magnitude correction for beam chop amplitude.

Table I. Summary of Infrared Measurements

Filter	Wavelength (microns)	Magnitude*	Normalized Reflectivity
J	1.25 ± 0.30	12.26 ± 0.05	0.87 ± 0.06
H	1.65 ± 0.35	11.81 ± 0.05	1.0 ± 0.06
K	2.20 ± 0.42	11.79 ± 0.05	1.00
CVF	3.05 ± 0.06	—	0.34 ± 0.12
L	3.45 ± 1.05	$12.66^{+0.16}_{-0.26}$	$0.52^{+0.14}_{-0.08}$

*Within 8 arcsecond diaphragm.

Figure 3. The 1-4 μm reflectivities of comet Bowell are compared with the reflectivity of water frost. The 1 sigma uncertainties are indicated. Horizontal bars indicate broadband filter FWHM. The comet exhibits a low 3-4 μm reflectivity similar to H_2O, but is otherwise spectrally dissimilar to H_2O.

NORMALIZED REFLECTIVITIES OF COMET BOWELL AND WATER FROST

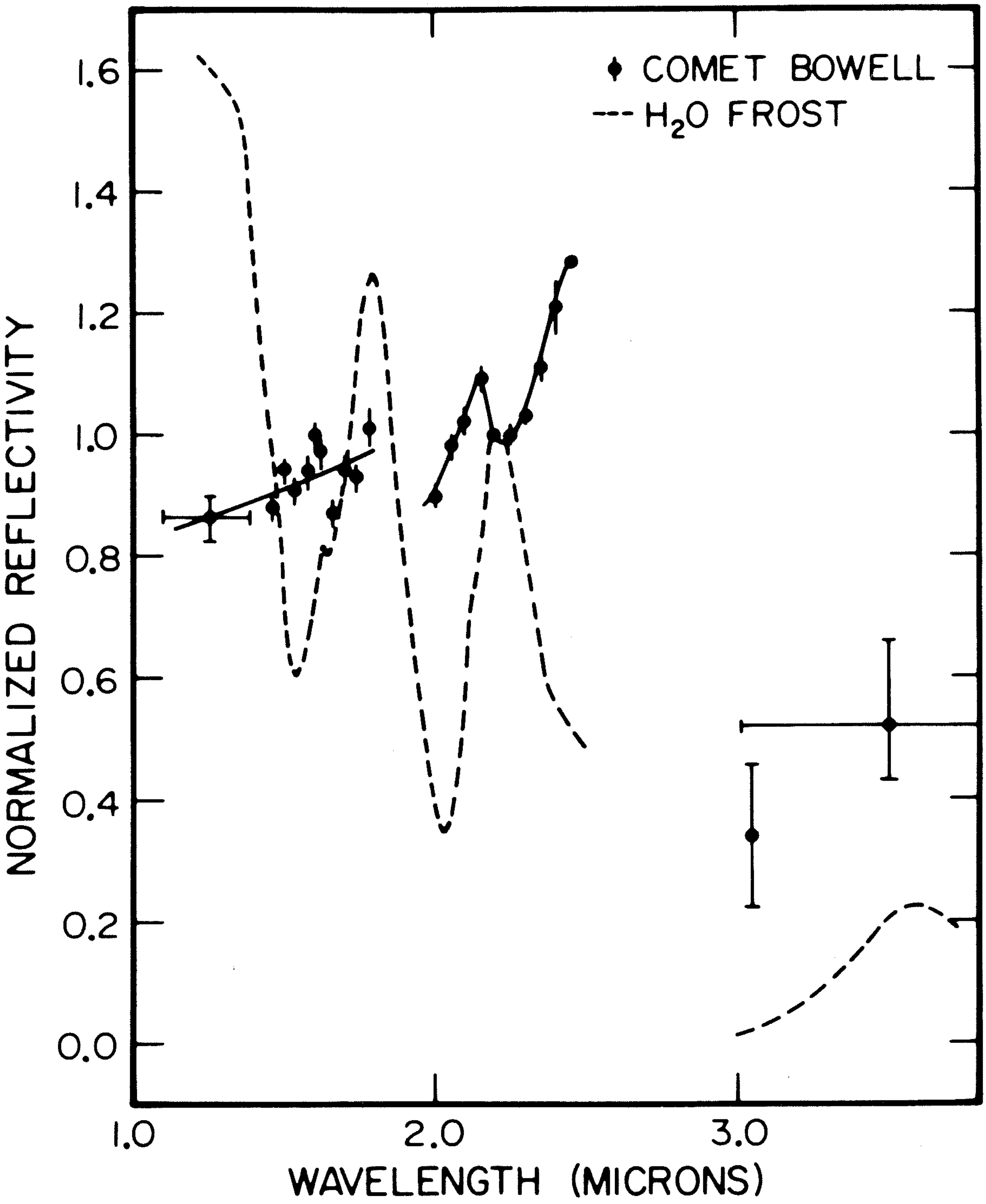

Table II. Comet Bowell J Magnitudes

JD	R	Δ	α	J	φ	Chop Amplitude	$\Delta J_1{}^1$	$\Delta J_2{}^2$	J_c	Source
4551	5.62	6.27	8	14.32 ± 0.05	10.3	35NS	0.03	-0.00	14.29	A'Hearn et al., 1981
4674	4.80	3.84	4	13.65 ± 0.05	8	20NS	-0.24	-0.11	13.30	Veeder and Hanner, 1981
4704	4.61	3.64	3	12.89 ±0.1	11.5	14EW	0.15	-0.08	12.96	Campins et al., (1982)
4709	4.58	3.63	5	14.0 ± 0.1	6	6NS	-0.55	-0.26	13.19	Paper I
4719	4.52	3.63	7	13.43 ±0.1	8.7	10EW	-0.15	-0.19	13.09	Campins et al., (1982)
4734	4.43	3.68	9	13.19 ±0.1	11.5	14EW	0.15	-0.17	13.17	Campins et al., (1982)
4739	4.40	3.71	11	13.13 ±0.1	7.8	10EW	-0.27	-0.16	12.70	Campins et al., (1982)
5092	3.40	2.70	14	12.91 ± 0.09	6	6NS	-0.55	-0.25	12.11	IRA, unpublished
5118	3.45	2.51	8	12.26 ± 0.05	8	20NS	-0.24	-0.00	12.02	this work
5152	3.53	2.52	2	12.6 ± ?	7.5	18EW	-0.31	-0.00	12.29	Koornshef and Shuster, 1982

The correction was determined from measurements of a CCD image at 0.65 μm wavelength. Artificial aperture photometry was performed in order to estimate the relative coma signals in the chopped reference beams. It was assumed that the surface brightness law at J (1.2 μm) was similar to that at 0.65 μm.

Column 10	$J_c = J + \Delta J_1 + \Delta J_2$.
Column 11	The source of the J magnitude measurement.

The K magnitudes published by Campins et al. (1982) were converted to J magnitudes using the empirical color $J - K = 0.46 \pm 0.04$ (see Table III). Figure 4 illustrates the variation of the corrected magnitudes, J_c with Julian Date.

The cometary magnitudes should also be corrected for the intrinsic phase function of the grains since the measurements were taken at different phase angles. However, in view of the absence of information relating to the phase coefficients of the cometary grains at small phase angles, we have not attempted this correction. It should be noted that unless the grains have very strongly peaked backscattering, the phase corrections would probably amount to $\lesssim 0.5$ mag.

3. Interpretation of the Observations

3.1 Infrared Reflectivities

The measured broadband reflectivities are plotted in Figure 3. Also shown is the 1.4 to 2.4 μm spectrum reported in Paper I. The reflectivities have been normalized to unity at K(2.20 μm). In compiling Figure 3 it has been implicitly assumed that the broadband reflectivities obtained in May, 1982 may be directly compared with a CVF spectrum obtained in April, 1981. We believe this assumption is justified since repeated measurements, listed in Table III,

Table III. Summary of Comet Bowell Color Measurements

JD	φ (arcseconds)	*J*−*H*	*H*−*K*	Source
4709	6	0.5 ± 0.1	0.0 ± 0.1	Paper I
4674	8	0.46 ± 0.07	0.08 ± 0.07	Veeder and Hanner (1981)
5092	6	0.37 ± 0.12	0.09 ± 0.11	IRA, unpublished
5118	8	0.45 ± 0.07	0.02 ± 0.07	this work

indicate that the broadband color of the comet has not changed perceptibly since the time of its discovery. Consequently, gross spectral variations are unlikely to have occurred in the interval between the two above-mentioned sets of observations.

The main feature of the spectrum of comet Bowell is the pronounced 3 μm reflectivity minimum. This feature is very broad and extends at least as far as the L(3.7 μm) data point. Other features in the 2 μm region have considerably smaller, though still significant, amplitudes. These features have been fully discussed in Paper I.

An important question concerns whether or not the 3 μm reflectivity minimum provides evidence for the existence of H_2O ice in comet Bowell, as has been claimed by Campins et al., 1983. Although H_2O ice does exhibit a deep reflectivity minimum at about 3.05 μm wavelength, the feature is much less broad than the one observed in comet Bowell (see Figure 3). The water ice feature has a full width at half maximum of about 300 cm^{-1} (Fink and Sill, 1982) corresponding to $\Delta\lambda_{1/2} \simeq 0.3$ μm. This is smaller than the observed width $\Delta\lambda_{1/2} \gtrsim 0.6$ μm. In addition, the 2.00 μm and 1.50 μm reflectivity minima of H_2O ice are coincident with local reflectivity maxima in the comet spectrum, suggesting that the comet material is not H_2O. The spectrum of solid NH_3 is similar to the 2 μm spectrum of comet Bowell and also displays a strong 3 μm absorption. However, the 3 μm absorption of NH_3 is again too narrow to be likened to the cometary 3 μm feature. Other chemically simple ices such as CH_4, CO_2, $H_2O{\cdot}NH_3$, $H_2O{\cdot}2NH_3$ do not have reflection spectra which are similar to the comet spectrum. Likewise, the spectra of cosmically abundant materials represented in planetary satellites, asteroids, meteorites and interstellar dust grains are not at all similar to the comet spectrum.

It might be argued that diffraction effects in very small coma grains could account for some aspects of the comet Bowell spectrum. Diffraction effects might broaden the 3 μm minimum, for example. However, independent constraints on the grain size in comet Bowell, inferred from the absence of superheat (Paper I) and from the length of the tail (Sekanina, 1982), both suggest grain diameters $2a \gtrsim 10\,\mu$m. Such grains have $x = 2\pi a/\lambda \gtrsim 10$ at $\lambda = 3\,\mu$m and are thus probably too large to produce broadening of the 3 μm feature. As in Paper I we must conclude that the spectrum of comet Bowell cannot be identified with any known material and is almost certainly not due to H_2O. The strongest similarity is still with solid NH_3 but significant differences exist and grains composed of the latter would in any case be unstable to sublimation at the heliocentric distance of comet Bowell (Paper I).

3.2 Photometric Behavior

The broadband magnitudes, which are plotted as a function of Julian Day Number in Figure 4, contain information concerning the volatility of the cometary material. We first attempt to compare the observations to a model in which the coma is supposed to result from equilibrium sublimation of the surface of the nucleus. The objective of the comparison is to determine the latent heat of sublimation of the nucleus material.

We adopt the Clausius-Clapeyron approximation for the gradient of the solid-vapor phase boundary to find the mass sublimation flux (Glasstone, 1946)

$$\frac{dm}{dt}(T) = \left[\frac{\mu m_{\rm H}}{2\pi k T}\right]^{1/2} P_0 \exp\left[\frac{\mu m_{\rm H} L}{k T_0}\right] \exp\left[\frac{-\mu m_{\rm H} L}{k T}\right] \quad . \tag{3}$$

Here, μ is the molecular weight of the material, $m_{\rm H}$ (kg) is the mass of a hydrogen atom, $k\,(JK^{-1})$ is Boltzmann's Constant and T (K) is the temperature

Figure 4. Photometric models of comet Bowell. The models, described in the text, involve the equilibrium sublimation of water, ammonia, and nitrogen ices as the source of the observed coma. The dots represent the corrected J magnitudes of the comet within a 10 arcsecond diameter diaphragm (Table II).

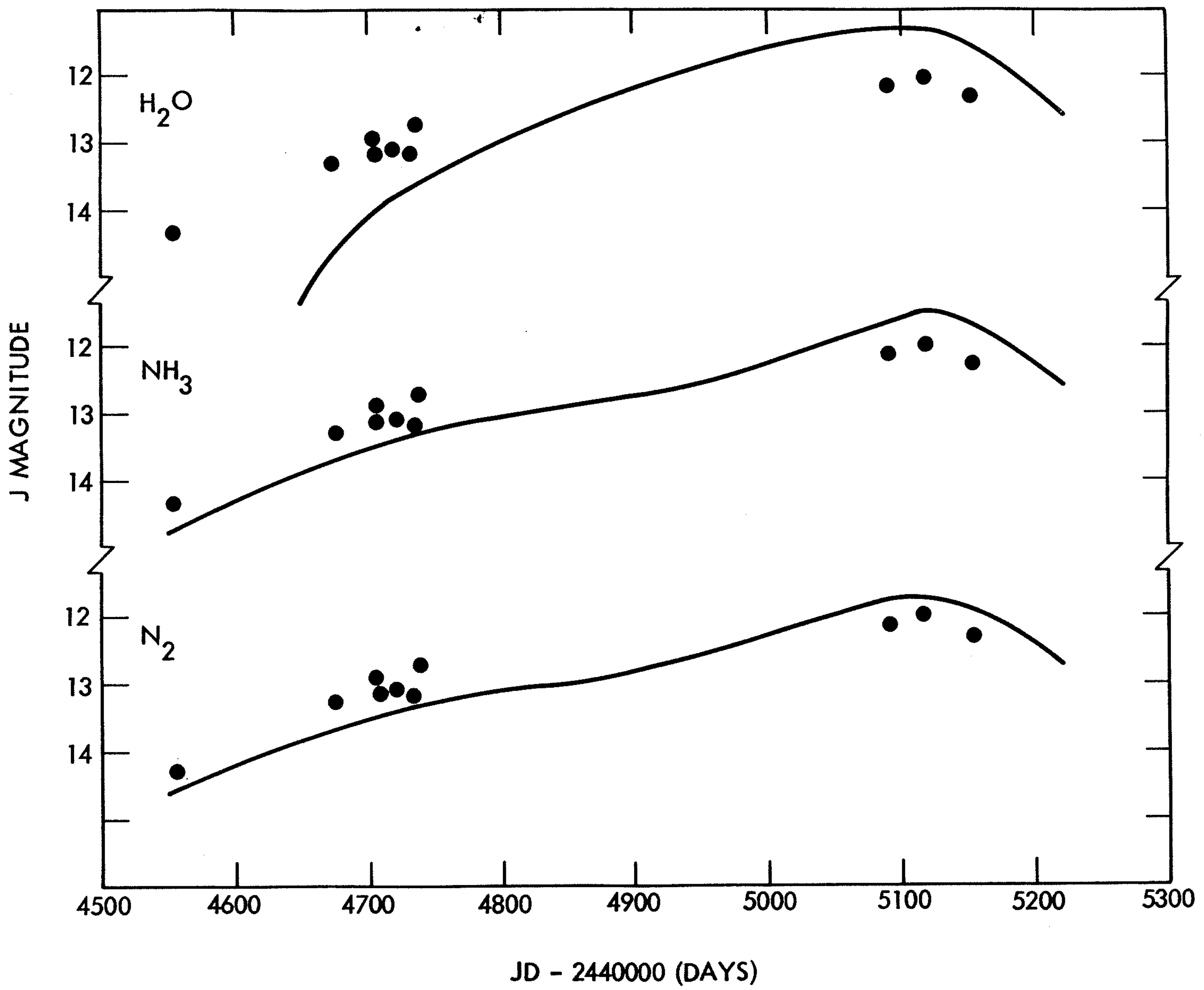
J MAGNITUDE
12
13
14
H_2O
NH_3
N_2
4500
4600
4700
4800
4900
5000
5100
5200
5300
JD - 2440000 (DAYS)

of the sublimating surface. $L(J\ \mathrm{kg}^{-1})$ is the latent heat of sublimation of the nucleus material and $P_0(Nm^{-2})$, T_0 (K) define a pressure, temperature reference point on the phase boundary. The temperature, T, must be found by solution of the thermal equilibrium equation at the surface of the nucleus, and will depend upon dm/dt. In addition, the solution for T will depend upon the albedo and emissivity of the nucleus and on its spin period. Since none of these quantities is known it is clear that the resulting model will be, at best, non-unique.

The mass sublimation flux was computed using the thermodynamic properties of the ices H_2O, NH_3, and N_2. These ices were selected to represent weak, intermediate and strong sublimation, respectively. However, their selection does not imply that we believe these particular substances to be present on the nucleus.

For the purposes of the model, it was further assumed that the ratio of the dust mass production rate to the gas mass production rate was a constant throughout the period of observations, namely:

$$\gamma \frac{dm}{dt} = \frac{4\pi}{3} \rho a^3 \frac{dN}{dt} . \tag{4}$$

Here, ρ (kg m^{-3}) is the dust grain density, $a(m)$ is the grain radius and dN/dt (m^{-2} s^{-1}) is the grain production rate per unit area. γ is a constant. Values of γ in the range $0.1 \lesssim \gamma \lesssim 1$ have been determined from observations of other comets (Ney, 1982) but we do not specify a value in the present model.

The rate of production of dust grain cross section dC/dt (m^2 s^{-1}) is given by

$$\frac{dC}{dt} = \chi \pi r_n^2 \, Q_{sca} \pi a^2 \frac{dN}{dt} \qquad (5)$$

where χ is equal to the ratio of the instantaneous sublimating area of the nucleus to the absorbing area ($2 \lesssim \chi \lesssim 4$), r_n (m) is the (unknown) radius of the nucleus and Q_{sca} is the scattering efficiency of the coma grains. The apparent magnitude of the model dust coma is given by

$$J = J_0 + 2.5 \log \left[\int_t^{t_0} \frac{dm}{dt} dt \right] \qquad (6)$$

where $t_0(s)$ is the epoch of observation and

$$t = t_0 - 3\varphi\Delta/4v \quad . \qquad (7)$$

In equation (6), J_0 is a function of χ, γ, r_n, Q_{sca}, ρ and a: it is effectively unconstrained by the observations. In equation (7), φ is the projected angular diameter of the diaphragm within which J is to be computed, Δ (m) is the geocentric distance of the comet and v (m s^{-1}) is the terminal speed at which the grains are ejected from the nucleus. We take $v = 1$ m s^{-1} as suggested by direct observation of the expansion of the coma (section 1.3). The difference $t_0 - t$) is a measurement of the diaphragm crossing time for the dust grains. For most of the observations we find $t_0 - t \geq 10^7$ seconds.

Equation (6) was solved for a range of times spanning the period of observations. The heliocentric and geocentric distances were found as functions of time from a model of the orbit by Yeomans (private communication, 1980).

The J magnitude models are plotted in Figure 4, for each of the three volatiles considered. The plotted curves represent the best fits obtained by varying the nucleus albedo and emissivity within wide ranges. Each model has been normalized to the data by selecting an appropriate value of J_0. The figure

Figure 5. Photometric model of comet Bowell in which the grain coma cross section is taken to be a constnt. The dots represent the corrected *J* magnitudes of the comet within a 10 arcsecond diameter diaphragm (Table II).

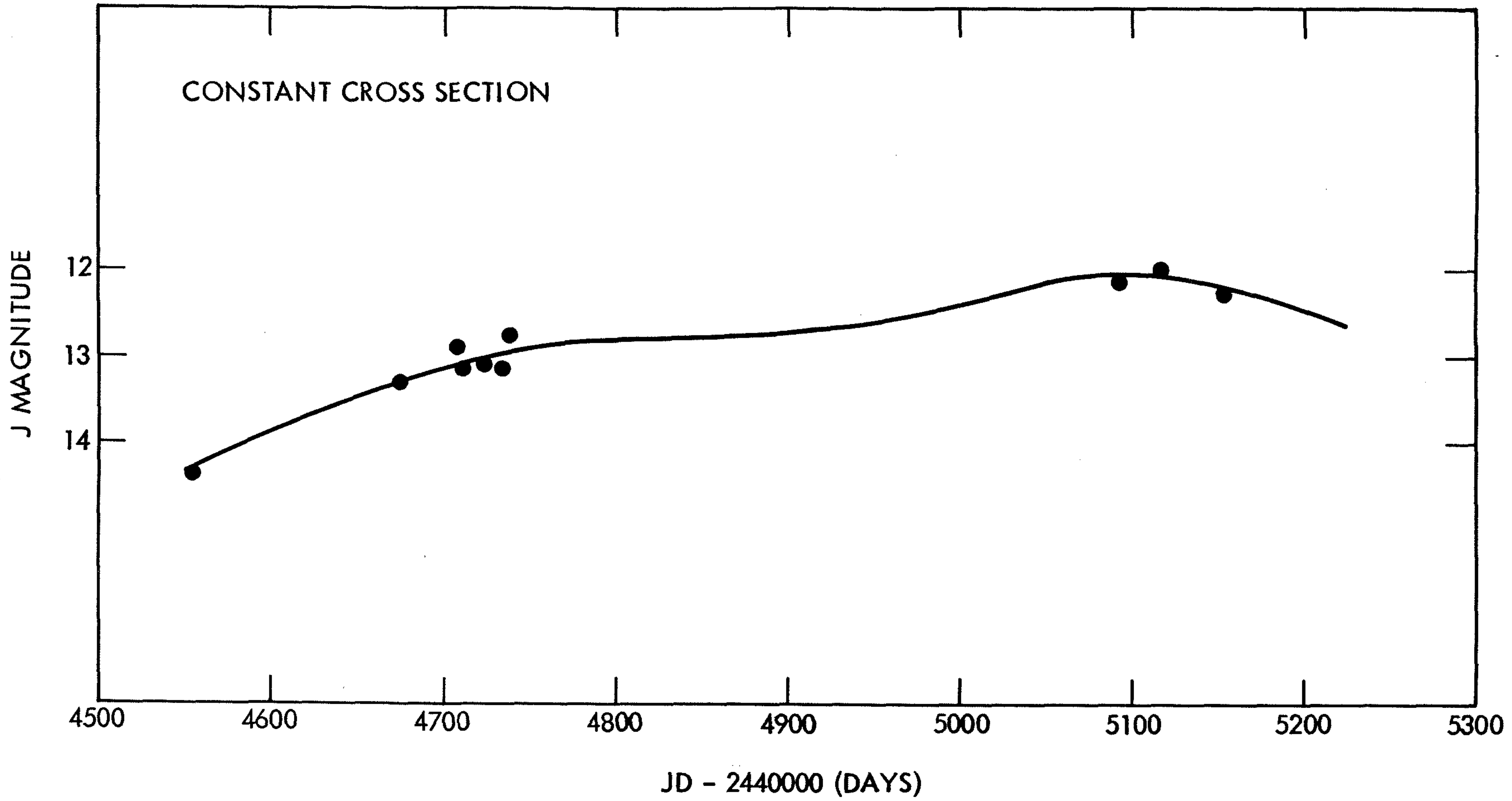
CONSTANT CROSS SECTION
J MAGNITUDE
12
13
14
4500
4600
4700
4800
4900
5000
5100
5200
5300
JD - 2440000 (DAYS)

shows that the equilibrium sublimation models do not well match the observed light variation of comet Bowell. The amplitude of the photometric variation of the comet within the period of observations is $\Delta J \approx 3$ mag. Even with very small nucleus albedos, $A = 0.02$, the model curves have significantly larger amplitudes. The least successful fit was obtained using H_2O as the sublimating volatile. We believe that Figure 4 presents a strong argument against the significant sublimation of H_2O from the nucleus of comet Bowell.

The apparent inadequacy of the equilibrium sublimation models prompted us to try a model in which the grain cross section is constant in time. In this model the variations of the J magnitude are entirely due to geometric effects. This second model is plotted, with the observations, in Figure 5. The model, in which J_0 is the only variable, evidently provides a better fit to the data than do the equilibrium sublimation models. This surprising result is consistent with the formation of the coma at some time prior to the first listed observation and is consistent with zero nucleus activity occurring at $R \lesssim 7$ AU.

It must be noted that although the calculated equilibrium sublimation models cannot be directly reconciled with the observations, the equilibrium sublimation of the nucleus may not be discounted. For instance, the models have been computed under the assumption of a constant dust to gas mass production ratio, γ. If γ happened to be a smoothly decreasing function of decreasing heliocentric distance then the model photometric amplitudes might be reduced to the observed value. Although we cannot disprove the hypothesis that γ varies with R in just the right way to fit the observations we are impressed by the success and simplicity of the constant cross section model.

4. Discussion

The observations reported in section 2 show that (1) the coma of comet Bowell is expanding at the rate $v = 0.9 \pm 0.2$ ms^{-}1, (2) the expansion was initiated in September 1978, approximately, (3) the grain cross section in the coma has not changed with time and (4) the grains have a peculiar near infrared reflection spectrum which is not similar to the spectra of common materials. Another pertinent observation has been made by Feldman et al. (1982), who find the OH production rate of comet Bowell to be $Q_{\mathrm{OH}} = 3 \times 10^{28}$ s^{-1} at $R = 3.4$ AU. This very large production rate must be reconciled with the apparently inert nature of the comet, as evidenced by the slow change of brightness with R and the inferred constant cross section in the coma.

The observation that coma expansion was initiated at $R \simeq 10$ AU effectively precludes water ice as the controlling volatile in the distant comet nucleus. At 10 AU even a perfectly absorbing water nucleus would exhibit negligible sublimation, the equilibrium temperature being as low as 100 K. However, it could be argued that water in the nucleus might be the source of the OH radicals detected near perihelion at $R = 3.4$ AU. We present an extreme example. At this heliocentric distance a water ice nucleus having a (very low) bond albedo, $A = 0.05$, would sublimate at the rate $dm/dt = 10^{-5.8}$ kg m^{-2} s^{-1}, corresponding to an OH production rate per unit area $\approx 6 \times 10^{19}$ m^{-2} s^{-1}. The sublimating surface area needed to supply the observed Q_{OH} would then be $\sigma = 3 \times 10^{28}/6 \times 10^{19} = 5 \times 10^{8}$ m^{2}. The radius of a spherical nucleus of this cross section would be $r_n = 1.3 \times 10^{4}$ m. A nucleus of this size would have an apparent magnitude $V \approx 17$, assuming its geometric albedo to be $p_v \sim 0.05$, and would be observed as a star-like central brightness spike in CCD images. The CCD images do not show such a feature. If we adopt the more reasonable parameters $A = 0.3$ and $p_v = 0.15$ (cf: Paper I) the equivalent spherical radius is very large, $r_n = 6 \times 10^4$ m, and the apparent magnitude of the supposed nucleus $V \approx 14$. Feldman et al. (1982) have suggested a nucleus radius $r_n \gtrsim 10^5$ m from similar considerations. The absence of a central brightness spike corresponding to a large nucleus implies that the OH radicals do not arise from dissociation of water molecules sublimated from such a nucleus. They must have another source. We suggest that the grain coma may be the source.

The grain coma was observed to have a cross section 3×10^8 m^2 within a diaphragm of radius 1.2×10^7 m (Paper I). From the surface brightness profile shown in Figure 1 of Paper I we estimate the total grain cross section to be $\sigma_g \simeq 10^9$ m^2. The grains are likely to be individually close to isothermal since they have diameters of only ~ 10 μm and they probably spin very rapidly. Consequently, the effective sublimation cross section is $4\sigma_g \sim 4 \times 10^9$ m^2. This is sufficiently large that the coma grains could supply the observed Q_{OH} if they were composed wholly or partly of water ice. Observations reported in Paper I show that the geometric albedo of the grains is close to 0.15: the Bond albedo is unlikely to be more than a few times this value and will not be any smaller than it. For example, if $A = 0.3$, the grains would sublimate so as to give $Q_{\mathrm{OH}} \approx 1.3 \times 10^{28}$ s^{-1}, which is equal to the observed $Q_{\mathrm{OH}} \approx 3 \times 10^{28}$ s^{-1}, within the approximations of the calculation and the uncertainty of the measurement.

One possible difficulty with the suggestion that the coma grains are the ultimate source of the OH radicals is that the overtones of OH bond vibrations are not observed in the near infrared spectrum of the grains. Instead, spectral features which resemble the overtones of NH vibrations are seen. Presumably this observation may be understood if the number of NH bonds in the grains considerably exceeds the number of OH bonds. However, we cannot suggest a material in which this condition holds.

An obvious requirement of the sublimating grain hypothesis is that the grains should not be depleted on a time scale short compared with the duration of observations. The mass of the grain coma is $m \sim \rho a C$ and the depletion time scale can be estimated from $t \sim \rho a C / \mu m_H Q_{OH}$, where $\mu = 18$ for H_2O and we assume $Q_{OH} = Q_{H_2O}$. Inserting $\rho \simeq 10^3$ kg m^{-3}, $a \gtrsim 10^{-5}$ m, $C = 10^9$ m^2 and $Q_{OH} \sim 10^{28}$ s^{-1} gives $t \gtrsim 3 \times 10^4$ s. This is very short. The largest grain size reasonably consistent with ejection from the nucleus by gas drag is probably 10^{-3} to 10^{-2} m, giving $t \sim 3 \times 10^6$ s to 3×10^7s. Evidently, only the largest conceivable grains could supply the observed OH fluxes for long periods of time.

The model presented in this paper may be used to make several predictions which will be susceptible to observational tests as the comet recedes from the sun. Firstly, the radius of the grain coma should continue to increase at the rate $v \sim 1$ ms^{-1}. Secondly, the total cross section should remain equal to σ_c and the comet magnitude will follow the curve shown in Figure 4. Thirdly, the distributed nature of the OH source will cause the usual Haser analysis to be inapplicable. In particular, at any instant the measured Q_{OH} should be proportional to the diameter of the diaphragm used to obtain the measurement.

A number of recent comets have exhibited optical properties which at least superficially resemble those of comet Bowell. Comets Panther and Elias were both active at large R (Elias at $R \gtrsim 5$ AU) and displayed large, roughly spherical dust comae. The infrared spectrum of comet Panther was identical to the spectrum of comet Bowell, within the uncertainties of measurement (Paper I). No information is available concerning variation of the coma radius or of the total grain cross section in either of these two comets, however.

5. Summary

1. The coma of comet Bowell is expanding at the speed $v = 0.9 \pm 0.2\ \mathrm{ms}^{-1}$.
2. The optical spectrum of the coma exhibits no gas emission lines or bands. Instead, only scattered sunlight is observed. The observed coma of comet Bowell was ejected impulsively at $R = 10$ AU on Julian Day 2443760 ± 700.
3. The dust cross section present in the coma has not changed throughout the interval of observation.
4. In the near infrared the coma dust grains display unidentified ammonia-like reflection spectra.
5. Large OH production rates inferred from IUE observations close to perihelion may result from sublimation of the grains in the coma, rather than sublimation of the surface of the nucleus.

Acknowledgements

Grateful thanks are offered to S. Staples (Palomar Observatory) and D. Greip (NASA-IRTF) for skillful operation of the telescopes. I thank J.A. Westphal and J.E. Gunn for permission to use the CCD camera 'PFUEI' and Ed Danielson for assistance with its operation.

References

A'Hearn, M.F., Dwek, E., and Tokunaga, A.T. (1981). *Ap. J.* **248**, L147.

Bowell, E. (1980). IAU Circular No. 3465 (April 3).

Campins, H., Rieke, G.H., Lebofsky, M.J., and Lebofsky, L.A. (1982). *Astron. J.* **87**, 1867.

Campins, H., Rieke, G.H., and Lebofsky, M.J. (1983). *Nature* **301**, 405.

Cowan, J.T. and A'Hearn, M.F. (1982). *Icarus* **50**, 53-62.

Eggerton, A.C. and Edmondson, W. (1928). In *International Critical Tables*, Vol. III, 207, McGraw-Hill, New York.

Feldman, P.D., A'Hearn, M.F., and Festou, M.C. (1982). *BAAS* **14**, 752 (abstract).

Feldman, P.D., A'Hearn, M.F. and Millis, R.L. (1982). IAU Circular No. 3699 (May 28).

Fink, U. and Sill, G.T. (1982). In *Comets*, ed. L.L. Wilkening, University of Arizona Press, Tucson.

Glasstone, S. (1946). *Textbook of Physical Chemistry, 2nd edition*, New York, D. Van Nostrand Company.

Hasegawa, I., Nakano, S. and Yabushita, S. (1981). *Mont. Not. R. astr. Soc.* **196**, 45P-46P.

Jewitt, D.C., Soifer, B.T., Neugebauer, G., Matthews, K. and Danielson, G.E. (1982), *Astron. J.* **87**, 1854.

Koornshef, J. and Shuster, H.E. (1982). IAU Circular No. 3710 (July 14).

Ney, E.P. (1982). In *Comets*, edited by L. Wilkening, University of Arizona Press, Tucson.

Sekanina, Z. (1982). *Astron. J.* **87**, 161-169.

Veeder, G.J. and Hanner, M.S. (1981). *Icarus* **47**, 381-387.

Washburn, E.W. (1928). In *International Critical Tables*, Vol. III, 210- 212, McGraw-Hill, New York.

Overview of Planetary Nebulae

Definition

A strict practical definition of a planetary nebula has yet to be agreed upon by the astronomical community. A useful working definition is that any sub-parsec scale object which emits strong forbidden lines of high ionization state ions (especially [OIII]λ5007), is a planetary. This definition excludes the nuclei of Seyfert galaxies (they are much larger) but may include a few novae and supernova remnants. This definition probably excludes very young planetaries in which the ionization fraction is small as a result of recombination promoted by high number densities, and may also exclude a small number of otherwise quite ordinary planetaries. However, to the extent that a rigid definition is necessary the present one is adequate.

The physical definition of a planetary nebula is less ambiguous. A planetary nebula is the escaping envelope of an evolved giant star. The envelope, or some fraction of it, is ionized and rendered visible by a high flux of ultraviolet photons from the exposed hot degenerate core of the star.

Statistics

Historically, PNs have been discovered serendipitously by astronomers involved in unrelated astronomical endeavors. William Herschel, who coined the name to highlight the superficial resemblance between some planetary nebulae and the planet Uranus, discovered several dozen PN's while engaged in his famous star counting project. Several hundred PNs, mostly unresolved or barely resolved, were discovered during widefield objective prism sky surveys made in the early and middle parts of this century. The Palomar Sky Survey led to the discovery of several hundred, mostly faint, resolved PNs. A similar Schmidt survey of the Southern skies being undertaken by the UK Schmidt Facility in Australia is likewise revealing many previously unobserved PNs.

In total, more than 1000 Galactic PNs have been cataloged (Perek and Kohoutek, 1967). The planetaries are distributed about the plane of the Galaxy with a scale height of $z \sim 200$ pc. Their distribution is similar to that of old Population I type stars. These stars have nuclear burning times of order 10^{10} years and have approximately solar mass. The progenitors of the planetary nebulae probably had similar characteristics. When corrections are made for interstellar extinction and for incompleteness of the existing surveys, it is estimated that the total number of Galactic planetaries is $N \approx 5 \times 10^4$. This number is uncertain by at least a factor of several. Comparable numbers presumably exist in other galaxies similar to our own (e.g. M31), but in general only the most luminous of these may be telescopically detected (e.g. Jacoby and Lesser, 1981). The number of PNs which exist close enough to the Sun to permit spatially resolved structural studies of the type reported in this thesis is on the order of 100.

Central Stars

The central stars of planetary nebulae exhibit a wide range of luminosities and spectral characteristics. The luminosities are high, $10^1 \lesssim L/L_\odot \lesssim 10^5$ as are the temperatures of the central stars, $3 \times 10^4 \lesssim T(K) \lesssim 3 \times 10^5$ (O'Dell, 1968). Together, the temperatures and luminosities suggest that the stellar radii are very small, in some cases less than $0.1\ R_\odot$. The central stars are spectrally diverse (Aller, 1968). Several stars are known to exhibit time-dependent spectra. Their white dwarf nature is often confirmed by spectral analysis. However, the spectra of many central stars exhibit features suggesting violent surface activity. Numerous 100 to 1000 km s^{-1} wide spectrum lines in some stars suggest active ejection or accretion of matter similar to that seen in Wolf-Rayet stars. Still other central stars exhibit no spectrum lines at all consistent with the absence of an envelope around these stars.

The masses of the central stars are of great interest in connection with the study of the evolution of the progenitor objects. In a few nebulae the central star is a binary member. The spectroscopic masses determined from these pairs are $M \gtrsim 0.6 \ M_\odot$. In nebulae with single central stars the mass is less easily estimated. If the central star luminosity is known then a lower limit to the mass equal to the mass of a star on the verge of radiative instability (Eddington limit) may be set. If the star is presumed to support no internal nuclear reactions its mass cannot be greater than the Chandrasakhar limiting mass $M_c \sim 1.2 \ M_\odot$. The luminosity may typically be uncertain within an order of magnitude (due to distance uncertainty), leading to a corresponding uncertainty in the Eddington mass. However, when the distance is well known (for planetaries in the Magellanic Clouds, for instance) the central star mass is usually found to be in the range $0.6 \lesssim M/M_\odot \lesssim 1.0$ (Stecher et al., 1982).

Ionization

Free electrons in planetary nebulae have kinetic energies $kT_e \sim 1$ eV, which are much too small to produce ionization of the nebular atoms. Instead, the ionization is due to photoionization by ultraviolet photons. The exciting source is the exposed hot degenerate core of the former giant star. The peak emission from this $\sim 10^5$ K body occurs near $\lambda \sim 300$ Å or $E \sim 40$ eV. This is comparable to or larger than the ionization potentials of many ions of abundant elements so that widespread photoionization is possible in the nebula. A list of the observed ionization states of atoms in PNs together with their respective ionization potentials is given in Table I.

In ionization equilibrium, each ionization of an atom is followed by a recombination and the emission of a photon. The equilibrium condition for a single element is

$$4\pi N(i)\int_{\nu_i}^{\infty} a_\nu \frac{J_\nu}{h_\nu} d\nu = N(i+1)N_e\, \alpha(T_e) \quad .$$

On the left hand side, J_ν (J s^{-1} m^{-2} hz^{-1}) is the mean intensity of the radiation of frequency ν(hz), h (Js) is Planck's Constant, a_ν (m^2) is the photoionization cross section at ν, $N(i)$ (m^{-3}) is the number density of $(i-1)$ times ionized atoms. ν_1 is the frequency corresponding to the ionization potential of the atom. $4\pi J_\nu/h\nu$ is just the number of photons passing through 1 m^2 in one second per unit frequency. On the right hand side, $N(i+1)$ (m^{-3}) and N_e (m^{-3}) are the number densities of i times ionized atoms and free electrons, respectively. $\alpha(T_e)$ (m^3 s^{-1}) is the recombination coefficient to all levels of the atom.

The ionization equilibrium equation may be used to compute the neutral fraction $\xi \equiv N(I)/(N(I) + N(II) + \cdots)$ as a function of position in the nebula. To first order the mean intensity J_ν may be set equal to a dilute blackbody intensity, that is

$$J_\nu \approx B_\nu(T_s)\left[\frac{R_s}{R}\right]^2$$

where R_s (m) is the star radius and R (m) is the radial distance from the central star. In a typical planetary, $(R_s/R)^2 \sim 10^{-12}$ to 10^{-15}. In general the equation must be solved repeatedly for the i, $i + 1$ pairs of each atom. There are two important features of the ionization structure of planetary nebulae. Firstly, the higher ionization states of a given atom occur closer to the central star. Secondly, the transition between i, $i + 1$ ionization states occurs over a very small radial distance. The transition width, ΔR, is in fact comparable to the mean free path of an ionizing photon, namely

$$\Delta R \approx \lambda_{mfp} \approx \frac{1}{a_\nu N(I)} \approx 10^{13}\, m$$

or

$$\frac{\Delta R}{R_n} \lesssim 10^{-2}$$

where R_n is the nebular radius.

Both the "ionization stratification" and the sharp transition regions are commonly observed in resolved PNs. Because of the former effect, the "size" of a given nebula may be a strong function of the ion in whose light it is observed. For instance, the HeII (54.4 eV) region of a PN will be smaller than the HeI (24.6 eV) region, which will in turn be smaller than the HI (13.6 eV) region. Because of the second effect, each of these regions will be relatively sharply delineated. Ionization stratification has been used as an observational tool in structural investigations of nebulae (Osterbrock, 1970).

In a more detailed treatment of the ionization equilibrium of a planetary nebula, account must be taken of a) the ionizing photons ($\nu \geq \nu_1$) scattered by the nebular gas and b) the radial dependence of the total number density.

About one third of the recombinations between protons and electrons occur to the ground state of hydrogen. These transitions release ionizing photons which constitute the "diffuse radiation field." The mean intensity may be written

$$J_\nu = J_{\nu,s} + J_{\nu,D}$$

where $J_{\nu,s}$ is the direct but attenuated intensity of stellar photons

$$J_{\nu,s} = B_\nu(T_s)\left(\frac{R_s}{R}\right)^2 \exp(-\tau_\nu)$$

with

$$d\tau_\nu = a_\nu N(I)\, dR$$

and

$$J_{\nu,D} = D(\tau_{\nu_1})\, B_\nu(T_e)$$

is the diffuse radiation field. $D(\tau_{\nu_1})$ assumes a complex form (see part 3 of this thesis).

The form of the radial dependence of the total number density is determined by the dynamics of the expansion of the nebula. The expansion itself depends both on the initial conditions of the nebular ejection and on the heating of the gas by stellar photons. In general it is expected that

$$N(R) \propto R^{-n} \quad , \qquad 2 \lesssim n \lesssim 3 \quad .$$

$n = 2$ would occur in a nebula undergoing isotropic expansion at constant speed.

An important parameter of PN models, and of PNs themselves, is the total radial optical depth at the hydrogen Lyman limit

$$\tau_{\nu_1} = -\int_{R_s}^{\infty} a_{\nu_1} \, N_H(I) \, dR$$

When $\tau_{\nu_1} << 1$ the nebula is optically thin at the Lyman limit and is said to be "density bounded." When $\tau_{\nu_1} >> 1$ the nebula is optically thick at the Lyman limit and is said to be "radiation bounded." Specific examples of nebulae in both categories are known. However, in general sufficient information does not exist to determine whether a particular nebula is in one limit or the other. This uncertainty poses a major obstacle to the interpretation of numerous observations of PNs. It has been common to assume that most nebulae are radiation bounded (for instance, in the application of the Zanstra (1926) method of central star temperature determination). Some of the observations reported in part 4 of this work do not support this assumption.

Up to this point we have quoted the typical electron densities and temperatures, N_e and T_e, to be about $N_e \approx 10^9$ m^{-3} and $T_e \approx 10^4$ K. These values are characteristic of PNs. They are observationally established by measurement of forbidden emission line ratios from certain ions. The forbidden ^{4}S-^{2}D lines of SII are commonly used for N_e, while the ^{1}D-^{1}S and ^{3}P-^{1}D lines of NII are used for T_e. It should be noted that measurements of N_e, T_e from emission line ratios suffer from the deleterious effects of line of sight averaging of dissimilar regions. For this reason, small scale structure often remains undetected in N_e, T_e maps even though considerable density and temperature fluctuations may be present.

To understand the reason for finding $T_e \approx 10^4$ K in PNs it is necessary to consider the heating and cooling mechanisms which occur in the gas (Osterbrock, 1974). The primary heating mechanism is the photoionization of hydrogen. Each stellar photon of frequency ν ejects a photoelectron of energy $h(\nu - \nu_1)$. The electron has a very large collisional cross section $\sigma_e \approx e^4/(\varepsilon_0 k T_e)^2 \approx 10^{-17}$ m^2, where $\varepsilon_0 (Fm^{-1})$ is the permitivity of free space and $e\,(C)$ is the charge on the electron, and a correspondingly small mean free path

$$\lambda_{mfp} \approx \frac{1}{\sigma_e N} \approx 10^8 \text{ m}$$

Consequently the photoelectrons become rapidly thermalized; a Boltzmann velocity distribution is rapidly achieved in the PN, which may be characterized by the temperature T_e.

The net heating rate per unit volume due to photoionization of hydrogen is

$$H = 4\pi N \int_{\nu_1}^{\infty} a_\nu \frac{J_\nu}{h\nu} h(\nu - \nu_1)\, d\nu$$

In a pure hydrogen nebula, cooling occurs through recombination and, to a much lesser extent, through free-free emission. The recombination cooling rate is

$$C_R = N_e N(I)\, k T_e \beta(T_e)$$

with

$$\beta(T_e) = \frac{1}{kT_e} \int_0^{\infty} \sigma(T_e)\, v f(v)\, \frac{1}{2} m v^2\, dv$$

where $\beta(T_e)$ (m^3 s^{-1}) is the kinetic energy weighted recombination coefficient.

In real nebulae, the cooling is dominated by forbidden line emission from collisionally excited metals, principally C, N, O. This is possible because the first excited levels of these abundant metals occur only a few eV above the ground states and can thus be populated by ~ 1 eV thermal electrons. (The first excited level of hydrogen is 10 eV above the ground state and cannot be so populated.) The computation of the cooling through the metals is slightly more complicated than for recombination cooling. We may write, for the cooling rate from a single ionization stage of an element

$$C_c = \sum_i N_i \sum_{j<i} A_{ij}\, h\nu_{ij}$$

where N_i (m^{-3}) is the number density of the ith level of excitation, A_{ij} (s^{-1}) is the spontaneous transition rate from levels i to j and ν_{ij} (hz) is the emitted photon frequency. The N_i can be computed, under the assumption of equilibrium, from

$$\sum N_j N_e q_{ji} + \sum N_j A_{ji} = \sum N_i N_e q_{ij} + \sum N_i A_{ij}$$

and

$$\sum_n N_n = N$$

where

$$q_{ij} = \int_0^\infty \sigma_{ij} v f(v)\, dv \quad .$$

q_{ij} ($m^3\ s^{-1}$) is the collisional de-excitation coefficient for the i to j transition, σ_{ij} (m^2) is the cross section, $f(v)$ is the velocity distribution of the nebular electrons. As noted above, $f(v)$ is normally well approximated by a Maxwellian.

Recent observations at thermal infrared wavelengths reveal strong emission from nebular dust grains (e.g. Telesco and Harper, 1977). The dust grains are heated by absorption of resonantly scattered Lyα photons, which have a very long path length in the gas. Additionally, absorption of Lyman continuum photons may be needed to explain the large infrared emission observed from some nebulae (Moseley, 1980). However, cooling by dust is difficult to account for, other than by empirical methods, since the dust properties and amounts seem to differ among nebulae.

In equilibrium, H = C and the equality may be solved for T_e. For total number densities $N \sim 10^9 - 10^{10}$ m^{-3} and for $T_s \sim 10^5$ K, typical PN temperatures are $T_e \sim 10^4$ K.

Structure

A description of the structure of planetary nebulae may be conveniently given in two parts; large scale structure and small scale structure. This division is made for observational reasons: it corresponds roughly to the division of the subject matter contained within parts 3 and 4 of this thesis.

Large Scale Structure

The large structures of PNs can be determined from monochromatic surface photometry and from resolved radial velocity profiles. The nebulae are optically thin at accessible visible wavelengths, making intepretation of the measurements feasible. On scales comparable with the nebular radius $10^{15} \lesssim l(m) \lesssim 10^{16}$ the PNs generally exhibit elliptical outlines in the plane of the sky. In a majority of cases the outlines are not very different from circles and an approximately spherical shape may be inferred. The surface brightness distributions of PNs suggest a wide variety of internal structures, however. The classical form is that of a bright annulus centered on the exciting star. The mass distributions in these "ring planetaries" have been modeled in two ways. The rings are supposed either to be thin spheroidal or ellipsoidal shells, or to be stubby toroids. On a statistical basis it may be shown that most ring planetaries belong to the former category, though some toroidal forms are known (NGC 6720, the subject of Chapter 3 of this thesis probably has a toroidal form (Minkowski and Osterbrock, 1960)). Other PNs have surface brightness increasing monotonically to the center, still others are bipolar and others irregular. The causes of the different morphologies are unknown. A simple evolutionary sequence which links the main subgroups has been proposed (Gurzadyan, 1969), but its validity is uncertain. Young PNs are supposed to be dense, bright and to have centrally condensed surface brightnesses. As the nebulae grow older they expand into rings (in the plane of the sky) and eventually become faint and distended as they mix with the interstellar medium. Bipolar PNs do not fit into this scheme, but for independent reasons they are believed to be young.

The distribution of mass in a PN generally cannot be inferred from the surface brightness distribution alone. We have already noted that the appearance of a given nebula may change dramatically depending on the wavelength of observation (due to ionization stratification). Combined measurements of the surface brightness profile, the line-of-sight averaged electron density and temperature and the velocity field can be used to obtain a clearer picture of the mass distribution. Only a few PNs have been observed in sufficient detail, however.

Observations of the internal motions in PNs are made by close inspection of forbidden emission lines at high spectral resolution (e.g. Osterbrock et al., 1966; Osterbrock, 1970). It is found that a) the PNs are expanding at $\bar{v} \approx 30$ km s^{-1}, with factor 2 dispersion; b) centrally condensed PNs exhibit a radial velocity gradient $v(R) \propto R$; c) no internal turbulence can be seen, setting a limit to the turbulent velocity dispersion of a few km s^{-1}.

In addition there is spectral evidence for the ellipsoidal true form of the nebulae from a Doppler shift asymmetry across nebular diameters.

Small Scale Structure

By small scale we refer to structures in PNs having characteristic dimensions comparable to or smaller than the best optical resolution attainable on the closest PNs, namely $l = 10^{14}$ m. Such structures can be discerned in many high quality Hα photographs of PNs. Small scale structure is of major importance to the understanding of the emission spectra of PNs. The small filaments and blobs in PNs often emit spectra quite unlike the spectra of adjacent regions (e.g. Mathis, 1976). Emission lines from low ionization potential ions are usually enhanced in the small structures. This observation suggests that these regions may be wholly or partly shielded from the direct stellar photons. Low ionization potential ions would be able to survive in the shadows of opaque or semi-opaque regions having dimensions $l \lesssim 10^{14}$ m. The necessary opacity might be provided by nebular dust particles, though it is not clear how such particles could be concentrated in optically thick knots and streamers. It has been suggested that dense "blobs" of HI could survive for significant periods against ionization, and would thus be able to provide shielding of stellar photons. Recent observations have revealed substantial masses of H_2 which could similarly provide temporary shielding. Possibly, the blobs could arise through a Rayleigh-Taylor instability at the HII/HI or HII/H_2

interface.

Mass

The masses of PNs are very uncertain. This is partly because the nebular distances cannot be measured with good accuracy. For instance, the optical mass may be estimated from

$$M \sim \mu m_H \overline{N_e}\, \vartheta^3 \Delta^3$$

where μ is the mean molecular weight of the plasma, m_H (kg) is the hydrogen atom mass, $\overline{N_e}$ (m^{-3}) is the average electron density in the PN (determined observationally). $R = \vartheta\Delta$ is the linear radius of the PN, ϑ is the angle subtended by the nebular radius and Δ is the distance to the nebula. In a bright optical nebula, $\overline{N_e}$ and ϑ may be measured with some precision. However, Δ must be determined by indirect means (as only one PN exhibits significant parallax). In practice, Δ is uncertain to within a factor ~ 2, so that the final mass is uncertain to within a factor $2^3 \approx 10$ (Acker, 1978; Milne, 1982). Such order of magnitude uncertainties are common to all mass estimates of PNs. Additionally, radiation bounded nebulae may contain considerable dark mass so that optically derived masses should properly be regarded as lower limits to the total mass.

The optical mass most commonly quoted in the literature is $M \sim 0.2\ M_\odot$, derived from observations of numerous planetary nebulae (Osterbrock, 1974). As the average of many different nebulae this estimate may be good to a factor of 2. In part 4 we argue that most PNs are surrounded by faint optical halos, each having a mass comparable to that of the nebula it surrounds. The best estimate of the optical mass would then be $M \sim 0.4\ M_\odot$ and the range of uncertainty in the above $0.2 \lesssim M/M_\odot \lesssim 0.8$. As noted in an earlier section, the central stars have masses $0.6 \lesssim M_s/M_\odot \lesssim 1.0$. Hence the total mass of the stellar plus optical nebula components is

$$0.8 \lesssim (M + M_s)/M_\odot \lesssim 1.8$$

from purely empirical considerations. This is likely to represent a rather generous estimate of the range of PN masses: a 0.8 $M_\odot$ star could not have evolved to the giant stage in the age of the galaxy and so could not give rise to a PN. However, these masses are consistent with estimates based on the galactic distribution of PNs (see earlier section).

Recent observations at longer wavelengths have tended to increase the probable masses of PNs by a large but uncertain amount. A handful of PNs have been shown to emit 2.12 μm vibration-rotation photons from molecular hydrogen, H_2 (Beckwith et al., 1978; Beckwith et al., 1980). The emission arises from the periphery of NGC 6720, the only PN it which it has been well mapped. A very indirect and uncertain estimate of the H_2 mass in NGC 7027 is $M_{H_2} \sim 3\ M_\odot$, with at least a factor of 3 uncertainty. The H_2 is shock excited (Kwan, 1977; Beckwith et al., 1980).

Observations of CO $J = 1 \rightarrow 0$ 2.6 mm emission from a small number of PNs have also been made in recent years (Mufson et al., 1975; Knapp et al., 1982). Indirect mass estimates give $M_{H_2} \sim 1$ to $5\ M_\odot$ in NGC 7027; although the uncertainty is large, evidently a considerable mass is present. No significant spatial information is available from the CO observations.

Formation

The mechanism of the formation of planetary nebulae is very poorly understood. The estimated total number of galactic planetaries, $N \sim 5 \times 10^4$, and the expansion lifetime, $t_e \sim 10^4$ years, suggest an order of magnitude formation rate ~ 10 per year. Even allowing for interstellar extinction it is likely that a few planetary nebulae should have been observed in the process of formation. There are several candidate objects, most notably V 1016 Cygni and HM Sge (Ciatti et al., 1977). The former underwent a brightness increase of $\Delta m \sim 5$ magnitudes in the interval 1963-67. In the same time, the spectrum changed from that of a giant long period variable star to that of a dense planetary nebula. Additionally, observations of CO emission from a number of stars reveal mass loss rates $\dot{M} \approx 10^{-4}\,M_{\odot}$/year, comparable to the rates expected in planetary nebula ejection (Knapp et al., 1982). However, since the information on these newest objects is either fragmentary or very new (and tentative) it is true to say that most clues to the formation of PNs have been gleaned from observations of older, more "ordinary" PNs.

The most important clue to the origin of PNs is provided by the relatively uniform nebular expansion velocity, $v_{\rm neb} \simeq 30$ km s^{-1}. $v_{\rm neb}$ is small compared to the escape velocity of the central star, $v_e \simeq 10^3$ km s^{-1}, but is close to the escape velocity expected of a red giant, $v_e \simeq 10$ km s^{-1}. The latter similarity suggests that planetary nebulae are ejected from red giants which then evolve into the small, hot central stars observed in PNs.

There are three main models of the nebula formation process:

1) Pulsational Instability

Giant stars are prone to pulsational oscillations which are caused by cyclic opacity variations in the envelopes. In certain modes the sum of the kinetic, gravitational potential and recombination energies may exceed zero.

Such modes are unstable and may lead to ejection of the stellar envelope. The degenerate core of the giant would be left as a remnant (Scott, 1973; Paczynski and Ziolkowski, 1968).

2) Radiation Pressure Ejection

The luminosity of the energy generating shell in the star may exceed the Eddington limit. The envelope would then be ejected by radiation pressure (Faulkner, 1970). The main objection to this mechanism is that stellar evolutionary models do not naturally lead to the very high shell luminosities needed.

3) Interacting Winds

Kwok et al. (1976) have noted that red giants lose mass in stellar winds. Typical mass outflow rates are $\dot{M} \lesssim 10^{-5}\ M_\odot$/year at outflow velocities $v \sim 10$ km s^{-1}. Kwok et al. suppose that such winds are followed by high velocity ($v \simeq 10^2$ to 10^3 km s^{-1}), low density ($\dot{M} < 10^{-7}\ M_\odot$/year) flows. The high velocity flow would overtake the low velocity wind. Compression in the interaction region would give rise to the observed ring-shaped planetary. This model has the advantage of great simplicity. However, there are formidable difficulties, most notably 1) observational evidence for the presence of high velocity flows is meager and 2) the model does not account for PNs other than those having ring morphologies.

A common feature of the red giant models of PN formation is that they predict each PN to be surrounded by a low density, potentially massive cloud of neutral hydrogen. A possible interpretation of the halos reported in part 4 of this thesis, is that they are the excited winds of the precursor red giants. This interpretation might also be compatible with the observation of peripheral molecular hydrogen in NGC 6720.

References

Abell, G.O. and Goldreich, P. (1966). *PASP* **78**, 232.

Acker, A. (1978). *Astron. Astrophys. Suppl.* **33**, 367.

Aller, L.H. (1968). In IAU Symposium No.34, "Planetary Nebulae," edited by D.E. Osterbrock and C.R. O'Dell, D. Reidel Publ. Co., New York.

Beckwith, S., Persson, S.E., and Gatley, I. (1978). *Ap. J.* **219**, L33.

Beckwith, S., Neugebauer, G., Becklin, E.E., and Matthews, K. (1980). *Astron. J.* **85**, 885.

Ciatti, F., Mammano, A., and Vittone, A. (1977). In "Interaction of Variable Stars with Their Environments," edited by Kippenhahn, Rahe, and Strohmeier, Bamberg.

Faulkner, D.J. (1970). *Ap. J.* **162**, 513.

Gurzadyan, G.A. (1969). Planetary Nebulae, Gordon and Breach, New York.

Jacoby, G.H. and Lesser, M.P. (1981). *Ap. J.* **86**, 185.

Knapp, G.R., Phillips, T.G., Leighton, R.G., Lo, K.Y., Wannier, P.G., and Wootten, H.A. (1982). *Ap. J.* **252**, 616.

Kwan, J. (1977). *Ap. J.* **216**, 713.

Mathis, J.S. (1976). *Ap. J.* **207**, 442.

Milne, D.K. (1982). *Mon. Not. R. astr. Soc. (1982)* 200, 51p.

Minkowski, R. and Osterbrock, D.E. (1960). *Ap. J.* **131**, 537.

Moseley, H. (1980). *Ap. J.* **238**, 892.

Mufson, S.L., Lyon, J., and Marionni, P.A. (1975). *Ap. J.* **201**, L85.

O'Dell, C.R. (1968). In IAU Symposium No. 34, "Planetary Nebulae," edited by D.E. Osterbrock and C.R. O'Dell, D. Reidel Publishing Co., New York.

Osterbrock, D.E., Miller, J.S., and Weedman, D.W. (1966). *Ap. J.* **145**, 697.

Osterbrock, D.E. (1970). *Ap. J.* **159**, 823.

Osterbrock, D.E. (1974). Astrophysics of Gaseous Nebulae, San Francisco, W.H. Freeman and Company.

Paczynski, B. and Ziolkowski, J. (1968). *Acta Astronomica* **18**, 255.

Perek, L. and Kohoutek, L. (1967). Catalog of Planetary Nebulae, Prague.

Scott, E.H. (1973). *Ap. J.* **180**, 487.

Stecher, T.P., Maran, S.P., Gull, T.R., Aller, L.H., and Savedoff, M.P. (1982). *Ap. J.* **262**, L41.

Telesco, C.M. and Harper, D.A. (1977). *Ap. J.* **211**, 475.

Zanstra, H. (1926). *Phys. Rev.* **27**, 644.

Distribution of Forbidden Neutral Carbon Emission in the Ring Nebula (NGC 6720)

D.C. Jewitt,[1,2] P.N. Kupferman,[3] G.E. Danielson,[1,2] S.P. Maran[4]

To appear in *The Astrophysical Journal*, May 15, 1983

[1]Palomar Observatory, California Institute of Technology

[2]Division of Geological and Planetary Sciences, California Institute of Technology

[3]Jet Propulsion Laboratory, California Institute of Technology

[4]Laboratory for Astronomy and Solar Physics, NASA Goddard Space Flight Center

Contribution number 3825 from the Division of Geological and Planetary Sciences, California Institute of Technology, Pasadena, California 91125.

Abstract

The spatial distribution of [CI] 9823, 9850 Å emission in NGC 6720 is reported. Like [OI], the [CI] radiation appears enhanced in the region of the bright filaments. A few percent of the carbon atoms in the filaments are neutral. This neutral fraction is consistent with ionization equilibrium calculations made under the assumption of complete shielding of direct stellar radiation by hydrogen. The observed carbon lines are excited by photoelectrons produced from hydrogen by the nebular diffuse radiation field. The [CI] observations confirm that the filaments in NGC 6720 are regions of locally enhanced shielding.

Subject headings: individual (NGC 6720) —nebulae: planetary

INTRODUCTION

Many planetary nebulae display emission lines from neutral atoms of low ionization potential which are considerably stronger than would be expected on the basis of standard ionization models. This fact is usually taken to indicate that some regions of the nebulae may be shielded from the ionizing UV radiation of the central star thus permitting neutral atoms to survive against ionization (Capriotti et al., 1971; Van Blerkom and Arny, 1972; Capriotti, 1973). Low ionization potential neutral atoms such as OI show a patchy and knotted distribution suggesting inhomogeneous distribution of shielding material in the nebulae. The shielding might be provided either by high density blobs of neutral hydrogen or by nebular dust particles.

However, evidence for the presence of shielded regions is not totally compelling. In particular, oxygen has a first ionization potential of 13.62 eV only marginally different from the value for hydrogen, 13.60 eV. This in addition to the presence of a strong charge exchange reaction with ionized hydrogen can lead to the stability of OI at the edges of HII zones in planetary nebulae without the necessity of special shielding.

Carbon has a first ionization potential of 11.26 eV, considerably less than the values for oxygen and hydrogen. The charge exchange cross section is unknown but is expected to be relatively small. In the absence of shielding carbon atoms would be rapidly ionized by the central star's UV radiation. Following an initial detection of [CI] in NGC 7027 by Danziger and Goad (1973) we have confirmed their result on that nebula and have searched for the 9823, 9850 Å $^3P-^1D$ lines of [CI] in five other planetary nebulae. A map of the spatial distribution of [CI] in NGC 6720 is the main topic of this paper.

OBSERVATIONS

The observations were taken using the Palomar 1.5 m telescope on UT March 23 and 24, 1982, and the Hale 5.1 m telescope on UT March 31, 1982. The Space Telescope WF/PC Investigation Definition Team CCD and the 'PFUEI' camera were used for all observations (Gunn and Westphal, 1981). In its direct camera mode PFUEI was used to obtain high resolution two dimensional images through narrow bandpass interference filters. The image scale on the 800 × 800 pixel CCD chip was 0.55 arcsecond per 15 micron pixel at the Cassegrainian focus of the 1.5 m telescope and 0.42 arcsecond per pixel at the prime focus of the 5.1 m telescope.

In its spectrographic mode PFUEI was used to obtain slit spectra in the range 6000 Å to 10000 Å. A grating blazed in the second order at 8100 Å was employed in conjunction with a 105 × 2 arcsecond slit. The dispersion was approximately 8.6 Å per pixel. Spectrum lines had FWHM of 5.2 pixels corresponding to 45 Å.

The high quantum efficiency (0.7 at 7000 Å wavelength and 0.2 at 10000 Å) and the large dynamic range of the CCD were crucial to the success of the observations. It proved possible to simultaneously record spectrum lines having intensity ratios of several thousands. In addition, the long slit permitted seeing-limited spatial resolution in the direction perpendicular to the dispersion. This enabled crude maps of emission line intensities to be constructed by taking data at several slit positions. The long slit also allowed the simultaneous recording of pure night sky emissions from the regions where it projected outside the nebula.

To facilitate data reduction, erase (zero exposure) and flat field frames were recorded intermittently during the observing periods. These were used to remove the effects of zero offsets from the chip and to divide out pixel to pixel variations in the chip sensitivity. Absolute flux calibration was obtained through observations of the flux standard stars HD 84937 and BD+26°2606 at similar airmasses.

Spectra of NGC's 2392, 3587, 6210, 6543, 6720 and 7027 were taken with the slit placed across the central stars at position angles 0° and 90°. NGC 2392 and NGC 6720 were more comprehensively mapped by taking several spectra at widely spaced positions over the surfaces of these nebulae. In the case of NGC 6720 the slit was moved to positions 5, 15 and 25 arcseconds north and south of the central star and exposures of 300 second duration were taken at each position using the 5.1 m telescope.

RESULTS

Figure 1 is an image of the first spatial derivative of the Hα surface brightness of NGC 6720 with respect to distance in the plane of the sky at a position angle 135°. It was obtained at the 1.5 m telescope using a single 200 second exposure made through a filter centered at 6562 ± 20 Å (FWHM). The first derivative of the surface brightness is presented because it strongly emphasizes the structure in the main shell of the nebula; in particular, several long curved filaments are enhanced. These filaments have characteristic widths of about 1 arcsecond in the Hα filter. The seven slit positions used to map the carbon emission are indicated in the figure.

Spectra of NGC's 2392, 3587 and 6543 fail to show the [CI] 9823, 9850 Å lines. However, NGC's 6210, 6720 and 7027 display [CI] emission. Nebulae other than NGC 6720 will be discussed in a future paper. In NGC 6720 the [CI] 9823 +

Fig. 1. An image of the first spatial derivative of the surface brightness of NGC 6720. The derivative of the surface brightness has been computed with respect to distance along a line running from north-west to south-east in the plane of the sky. Most of the light comes from Hα (6563 Å) but some is from [NII] (6548, 6588 Å). The seven slit positions used to obtain Fig. 2 are shown. The image emphasizes the long sharp filaments in the main ring.

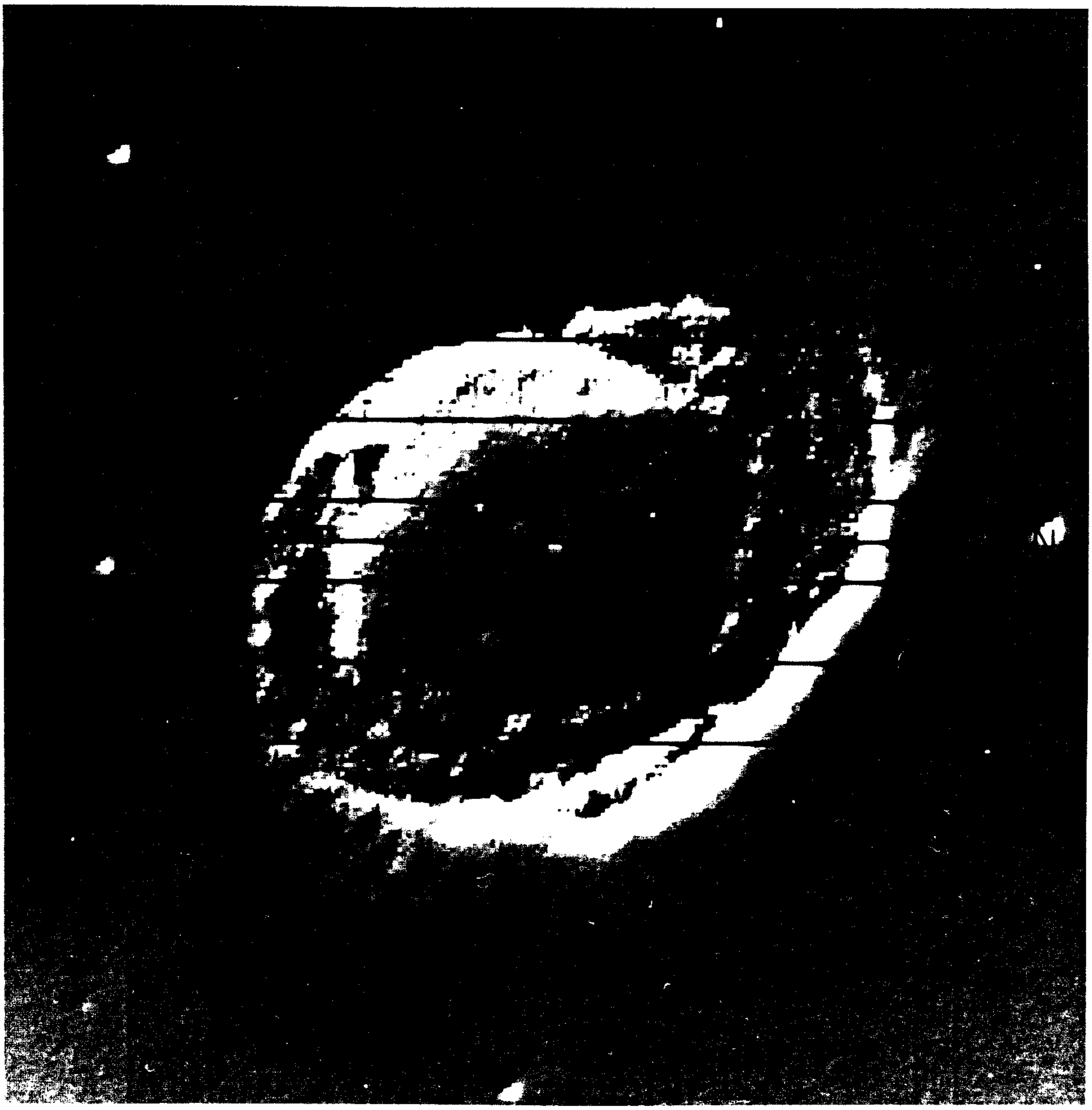

9850 Å lines were clearly recorded in the CCD spectra. They appear merged into a single broad line (FWHM 68 Å) centered at 9843 ± 2 Å. This is consistent with the combined effects of the instrumental resolution function and the 1:3.36 ratio of line intensities expected from the ratio of the transition probabilities (Nussbaumer and Rusca, 1979). The [CI] 9823 + 9850 Å emission distribution along seven slits projected across NGC 6720 is shown in Figure 2. The [OI] 6300 Å distribution, taken from the same spectra as the [CI] data, is shown for comparison. The emission is confined to a shell of about 20 arcseconds internal radius and 25 arcseconds thickness, centered on the central star. From the figure it may be seen that [CI] and [OI] emissions are strongly spatially correlated. Nowhere does the ratio of the two emissions vary by more than a factor of about two. Both [CI] and [OI] are irregularly distributed: comparison with Figure 1 shows that both lines appear bright where the slits cross the sharp filaments. In the central region of the planetary nebula the [OI] appears only faintly while the [CI] is virtually absent. Likewise, outside the main shell of the nebula both emissions fall to zero. Figures 1 and 2 together suggest that the [OI] and [CI] radiations originate from the same volumes of the nebula and that these volumes lie within the bright filaments.

The surface brightness in the [CI] 9823 + 9850 Å lines was measured to be $(1.3 \pm 0.1) \times 10^{-8}\ \mathrm{W m^{-2}\ sr^{-1}}$, from only the eastern half of the central slit spectrum. If the distance to the nebula is $\Delta \sim 700$ pc the interstellar absorption at 9800 Å amounts to about 0.3 magnitudes (Allen, 1973). The interstellar extinction correction is small enough that our conclusions are not sensitive to it. The corrected surface brightness is then $S = (1.7 \pm 0.2) \times 10^{-8}\ \mathrm{W m^{-2}\ sr^{-1}}$ and the total radiated power from the whole nebula is $4\pi S\Delta^2\Omega \simeq 1 \times 10^{25}$ W ($\sim 0.03\ L_{\odot}$). Here, $\Omega = 1.2 \times 10^{-7}$ sr is the solid angle

Fig. 2. Comparison of the [CI] 9823, 9850 Å and [OI] 6300 Å emission distributions in NGC 6720. Relative flux is plotted as a function of distance east and west of the central star for each of seven slit positions. The displacements of the different slit positions in the north-south direction are indicated. Sky and nebular continuum emissions have been subtracted.

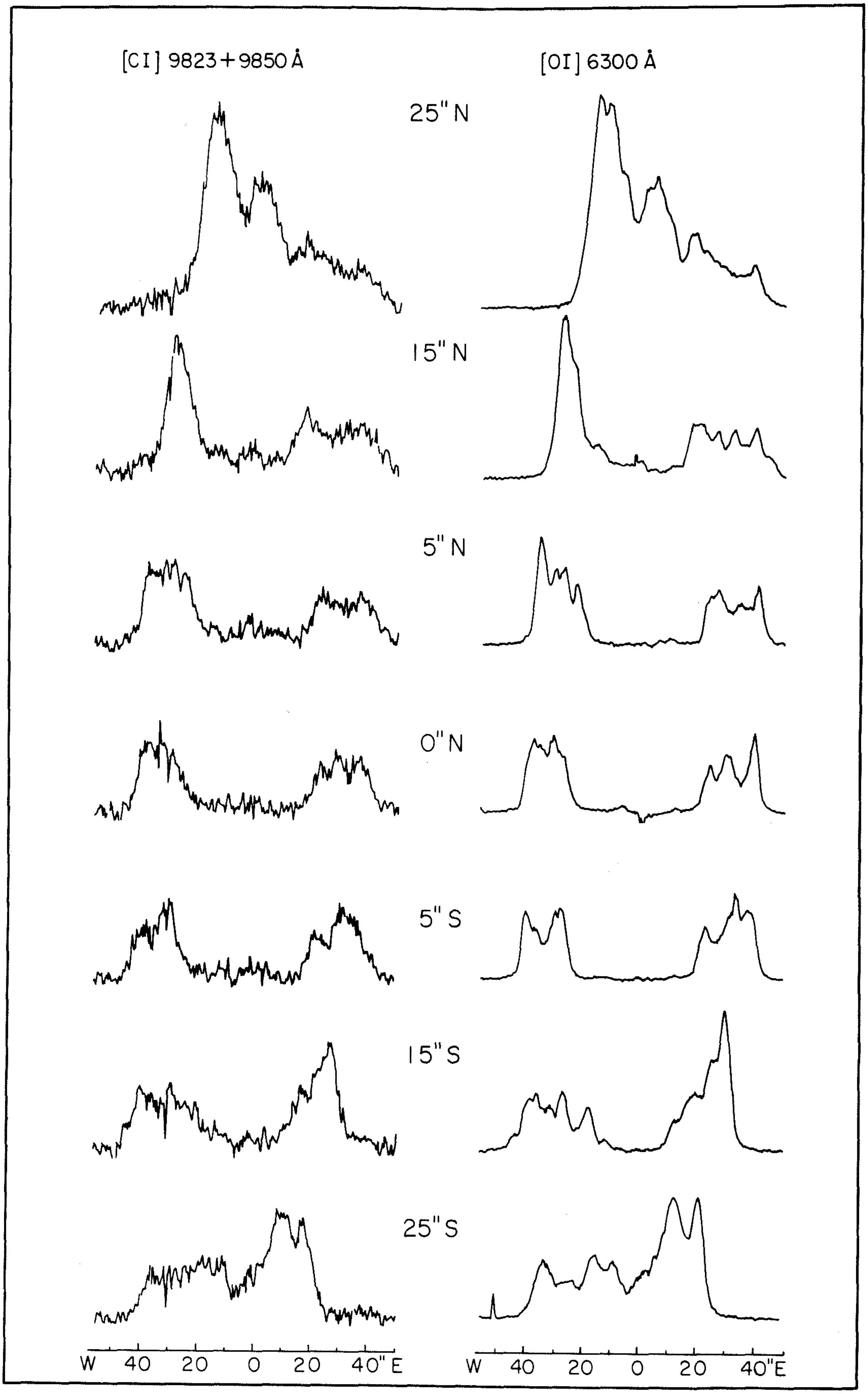
[CI] 9823+9850 Å
[OI] 6300 Å
25" N
15" N
5" N
0" N
5" S
15" S
25" S
W
40
20
0
20
40" E
W
40
20
0
20
40" E

subtended by the bright shell of the nebula.

The [CI] 8727 Å $^1D-^1S$ line was not detected in our observations. If present it must be blended with another nebular line only 13 Å away. Numerically generated spectrum lines were artificially blended in various proportions in order to estimate an upper limit to the [CI] 8727 Å line flux. Comparison with actual spectra shows that the [CI] 8727 Å line would have been detected if its surface brightness exceeded $(1.2 \pm 0.2) \times 10^{-9}$ Wm^{-2} sr^{-1}. Hence we find a 1 σ upper limit to the ratio

$$G = S(8727)/S(9823 + 9850) < 0.07 \qquad (1)$$

which is useful for comparison with theoretical calculations (see next section).

DISCUSSION

The principal difficulty with the interpretation of the present observations is that the electron temperature, T_e, and the electron density, N_e, are unknown in the [CI] emitting regions. This is because existing determinations of T_e and N_e are derived from line-of-sight averaged emission line intensity ratios from ions of relatively high ionization potential. The line-of-sight averages do not necessarily reflect the conditions inside the filaments where the [CI] radiation is produced. However, in the absence of other evidence we adopt the T_e, N_e measurements reported by Kupferman (1983). These are in quantitative agreement with independent determinations by Hawley and Miller (1977) and Barker (1980), but have the advantage of showing the two-dimensional dependences of T_e and N_e over the surface of the nebula.

The observation of [CI] may be used to estimate the number density of neutral carbon atoms in NGC 6720. [CI] emission has been computed as a function of N_e and T_e by Pequinot and Aldrovandi (1976). They employed a three level atom model and used the emission cross sections of Le Dourneuf et al. (1975). Under the assumption of a purely collisional excitation mechanism the equilibrium number density of CI is

$$N(\mathrm{CI}) = L/(N_e\ \varepsilon(T_e,N_e)V) \tag{2}$$

where N_e (m^{-3}) is the local electron density, $\varepsilon(T_e,N_e)$ ($\mathrm{Jm}^3\ \mathrm{s}^{-1}$) is the emission coefficient in the 9823 +9850 Å lines, and $L(W)$ is the total luminosity within the same lines produced within a volume $V(m^3)$. N_e and T_e were taken to be 10^9 m^{-3} and 10^4 K, respectively (Kupferman, 1983). The luminosity per unit volume was estimated from $\frac{L}{V} = \frac{4\pi S}{l}$ where S is the observed surface brightness. l is a characteristic length for the emitting region along the line of sight. The neutral carbon number density is found to be

$$N(\mathrm{CI}) \sim \frac{10^{19}}{l} \tag{3}$$

with l in meters. The major uncertainty in N(CI) results from the difficulty in assigning a value to l. An absolute upper limit to l can be set equal to 3×10^{15} m, the path length through the entire nebula at the observed position of the [CI] emission. The variation of the emission across the nebular filaments (see Figure 2), strongly suggests that l is similar to the characteristic width of these filaments, namely $l \sim 10^{14}$ m. The resulting CI number densities are $N(\mathrm{CI}) \gtrsim 3 \times 10^3$ m^{-3} and $N(\mathrm{CI}) \sim 10^5$ m^{-3}, respectively, with the latter value being the more plausible.

In passing we note that Pequinot and Aldrovandi (1976) predict a line intensity ratio $G = 0.06$ at our assumed values $N_e = 10^9$ m^{-3}, $T_e = 10^4$ K. This is consistent with the empirical upper limit $G < 0.07$. If N_e were 50% higher or T_e were 40% higher than the values we have used the predicted and observed ratios would not agree. However all lower values of N_e and T_e would be consistent with $G < 0.07$. $\varepsilon(T_e, N_e)$ is a very weak function of N_e but would increase (decrease) by a factor of four if T_e were increased (decreased) by a factor of two.

Assuming the cosmic abundance of carbon to be $10^{-3.4}$ that of hydrogen, we find $N(\mathrm{CI})/N(\mathrm{C}) > 10^{-2}$ and $N(\mathrm{CI})/N(\mathrm{C}) \sim 10^{-1}$ corresponding to the two length scales discussed above. The abundance of CI relative to hydrogen is $\sim 10^{-5}$. These values apply only to the filaments observed in [CI] emission.

The major questions arising from the observed high neutral carbon abundance are: 1) how can the carbon remain neutral against the effects of the ionizing stellar flux? and 2) how are the observed lines excited? We propose that the neutral carbon is located in regions of the nebula which are shielded from the direct stellar radiation and that photoionization of shielded hydrogen by photons from the diffuse radiation field provides the high electron densities needed to excite the neutral carbon atoms.

The equation of ionization equilibrium for hydrogen in the nebula is

$$4\pi N(HI)\int_{\nu_1}^{\infty} a(\nu)\, \frac{J_\nu}{h\nu} d\nu = N_e N(HII)\, \alpha\,(HI, T_e) \qquad (4)$$

where $N(HI)$ $N(HII)$ and N_e are the number densities of neutral and singly ionized hydrogen and of free electrons, respectively. $a(\nu)$ is the photoionization cross section for neutral hydrogen, $\alpha(HI, T_e)$ is the hydrogen recombination coefficient and ν_1 is the frequency of radiation at the Lyman limit. J_ν is the mean intensity of the radiation. To good approximation the photoionization cross section may be set equal to

$$\alpha(\nu) = A_H \left[\frac{\nu_1}{\nu}\right]^3 \tag{5}$$

where A_H is the cross section at $\nu = \nu_1$.

In general J_ν may be expressed as the sum of contributions from the direct but attenuated stellar radiation and from the diffuse radiation field. In the shielded regions of the nebula only the diffuse radiation is important. We use the approach of Van Blerkom and Arny (1972) and approximate the mean intensity at optical depth, τ, by

$$J_\nu(\tau) = D(\tau)\, B_\nu(T_e) \tag{6}$$

where $B_\nu(T_e)$ is the Planck function at electron temperature T_e and

$$D(\tau) = \left[\frac{1-\varepsilon}{\varepsilon}\right] W \frac{\int_{\nu_1}^{\infty}\left[\frac{\nu_1}{\nu}\right]^3 \frac{B_\nu(T_s)}{h\nu}\exp\left\{-\left[\frac{\nu_1}{\nu}\right]^3 \tau\right\} d\nu}{\int_{\nu_1}^{\infty}\left[\frac{\nu_1}{\nu}\right]^3 \frac{B_\nu(T_e)}{h\nu} d\nu} \tag{7}$$

Here $1-\varepsilon$ is the probability that a given recombination will occur to the ground state, W is a geometrical dilution factor equal to $(R_s/R)^2$, where R_s is the radius of the central star and R is the radius to the shielded region in the nebula. The optical depth, τ, is measured at $\nu = \nu_1$ along a radial direction from the central star. For simplicity the central star is approximated by a black body having temperature T_s.

Equations (4)-(7) have been used to compute the neutral hydrogen fraction in the shielded region. Assumed values were $N(HI) + N(HII) = 10^9$ m^{-3}, $T_e = 10^4$ K, $T_s = 10^5$ K and $W = 10^{-14}$. The values of A_H, ε and $\alpha(T_e)$ were taken to be 6.3×10^{-22} m^2, 0.62 and 4.2×10^{-19} m^3 s^{-1}, respectively (Osterbrock, 1974). The computed neutral fraction $\chi(H) = N(HI)/(N(HI) + N(HII))$ is given as a function of τ in the second-column of Table 1.

Table 1. Computed Neutral Fractions

τ	$\log\chi(H)$	$\log\chi(C)$
0	-3.67	-3.59
20	-2.21	-2.13
40	-1.75	-1.67
60	-1.45	-1.38
80	-1.24	-1.16
100	-1.07	-1.00

In the case of carbon the ionization equilibrium equation (4) was solved under the assumption that all free electrons come from hydrogen so that $N_e = N(HII) = 10^9(1-\chi(H))$. The CI photoionization cross section was approximated by (Osterbrock, 1974)

$$a(\nu) = a_T\left[\beta\left(\frac{\nu_1}{\nu}\right)^s + (1-\beta)\left(\frac{\nu_1}{\nu}\right)^{+s+1}\right] \tag{8}$$

where $a_T = 1.22\times 10^{-21}$ m^2, $\beta = 3.32$, $s = 2.0$ and $\nu_1 = 2.73\times 10^{15}$ Hz. The recombination coefficient was taken to be $\alpha(\mathrm{CI}, T_e) = 4\times 10^{-19}$ m^3 s^{-1} (Osterbrock, 1974). The computed neutral carbon fraction $\chi(C)$ is given as a function of τ in column 3 of Table 1.

It is evident from the Table that a significant fraction of the carbon atoms in the shielded regions may exist in the neutral state. Moreover, neutral carbon fractions on the order of 1%-10% occur even though the shielded hydrogen is quite strongly ionized $1-\chi(H) > 0.9$). This result remains true for other plausible choices of T_s and W. The electrons produced by the ionization of the hydrogen atoms are able to collisionally excite the neutral carbon atoms. Hence the observation of [CI] emission is consistent with the presence of shielded regions in NGC 6720. Furthermore, the distribution of [CI] radiation shows that the shielded regions are located within the bright filaments.

The 609 μm $^3P_1-^3P_0$ line of neutral carbon has been observed in several interstellar clouds (Phillips and Huggins, 1981). Assuming a line width due to turbulence of 1 km s^{-1} and an Einstein A coefficient equal to 8×10^{-8} s^{-1}, the 609 μm CI emission from NGC 6720 would be expected to lead to an antenna temperature $T_A < 10^{-2}$ K. This is about 100 times too weak to be detected using present submillimeter technology. Molecular hydrogen has been detected in the Ring Nebula and may be present in the shielded regions (Beckwith et al., 1978).

It remains to be seen whether all nebulae showing [CI] emission also show molecular hydrogen emission.

Numerous approximations have been made in this simple treatment. For example, the stellar flux may be poorly represented by a Planck function and helium has not been included in the calculations. When solving equation (4) we have neglected the (factor of two) N_e and T_e differences in the shielded regions. However, the uncertainties in the interpretation of the data probably do not warrant a treatment substantially more detailed than the one presented here.

SUMMARY

Neutral carbon emission in NGC 6720 is concentrated in several bright filaments and indicates a fractional concentration $N(CI)/(N(CI)+N(CII)) \sim 1$ to 10%. The [CI] radiation probably emanates from regions of the nebula which are locally shielded from the direct stellar radiation. Carbon in the shielded regions is able to remain neutral at the 1%-10% level, against photoionization by the nebular diffuse radiation field. Much of the hydrogen in the shielded regions is ionized by the diffuse radiation. The photoelectrons produced from the hydrogen are responsible for the collisional excitation of the neutral carbon.

Acknowledgements

We thank J.A. Westphal and J.E. Gunn for permission to use the CCD system and J. Carrasco, S. Staples and S. von Grolliken for assistance with the observations. S.P.M. thanks L. Aller, J.P. Harrington, M. Jura and T. Stecher for helpful discussions.

REFERENCES

Allen, C.W., 1973, ***Astrophysical Quantities***, Third Edition, The Athlone Press.

Barker, T., 1980, *Ap. J.* **240**, 99.

Barker, T., 1982, *Ap. J.* **253**, 167.

Beckwith, S., Persson, S.E., and Gatley, I. 1980, *Ap. J.* **219**, L33.

Capriotti, E.R., Cromwell, R.H. and Williams, R.E. 1971, *Ap. Letters* **7**, 241.

Capriotti, E.R. 1973, *Ap. J.* **179**, 495.

Danziger, I.J., and Goad, L.E. 1973, *Ap. Letters* **14**, 115.

Gunn, J.E. and Westphal, J.A., 1981, *SPIE* **290**, 16.

Hawley, S.A., and Miller, J.S., 1977, *Ap. J.* **212**, 94.

Kupferman, P.N., 1983, *Ap. J.* **266**, 689.

Le Dourneuf, M., Vo Ky Lan, Berrington, K.A., and Burk, P.G. 1975, Abst. IXth, ICPEAC, Seattle, p. 634.

Nussbaumer, H., and Rusca, C. 1979, *Astron. Astrophys.* **72**, 129.

Osterbrock, D.E. 1974, *Astrophysics of Gaseous Nebulae*, W.H. Freeman and Company, San Francisco.

Pequinot, D., and Aldrovandi, S.M.V. 1976, *Astron. Astrophys.* **50**, 141.

Phillips, T.G., and Huggins, P.J. 1981, *Ap. J.* **251**, 533.

Van Blerkom, D., and Arny, T.T. 1972, *Mon. Not. R. astr. Soc.* **156**, 91.

Halos Around Planetary Nebulae

David C. Jewitt,[1,2] G.E. Danielson, [1,2] P.N. Kupferman[3]

[1]Palomar Observatory, California Institute of Technology

[2]Division of Geological and Planetary Sciences, California Institute of Technology

[3]Jet Propulsion Laboratory, California Institute of Technology

Contribution number 3879 of the Division of Geological and Planetary Sciences, California Institute of Technology, Pasadena, California 91125.

Abstract

We report preliminary results of a CCD survey designed to detect and investigate faint halos around planetary nebulae. A TI 800 × 800 pixel CCD was used to take deep exposures of 44 planetary nebulae. The exposures were mostly obtained through an Hα filter at the Cassegrainian focus of the Palomar 1.5 m telescope. Spatial resolutions of 1 to 2 arcsecond were obtained across 400 arcsecond wide fields. The images, which are in many cases considerably deeper than any previously taken, reveal numerous planetary nebula halos. About 2/3 of the studied nebulae possess extensive outer halos. In some nebulae the mass in the halo is comparable to the mass contained in the primary HII region. We have used the data to place constraints on the mode of origin of the halos. It is likely that the halos originate either by dynamical separation of a single ejected shell of gas, or by the ejection of two or more such shells from the central star. It is unlikely that the halos are caused by excitation of the pre-planetary stellar wind and highly improbable that the halos represent reflection nebulae.

1. Introduction

The morphologies of planetary nebulae have been the subject of numerous observational and theoretical investigations (Curtis, 1918; Wilson, 1950; Osterbrock et al., 1966; Mathews, 1966; Weedman, 1968; Wentzel, 1976). Observationally, the problem is to deduce the three dimensional structure of the nebulae from their projections in the plane of the sky. This problem is made easier by the fact that the nebulae are optically thin at most wavelengths of observation. To some extent, Doppler velocity measurements can be substituted for the line of sight dimension, but the inversion problem is still intractable in many instances. A majority of the nebulae appear as elliptical rings in the plane of the sky. These are frequently interpreted to be single thin, ellipsoidal shells of gas. Other interpretations include toroidal shells with their cylindrical symmetry axes near the line of sight. Some nebulae appear as centrally condensed objects; still others seem to be completely amorphous. Theoretical investigations have been confined to the most simple, spherically symmetric models and have had some success in matching the observed nebular expansions (Mathews, 1966; Hunter and Sofia, 1971).

In a number of planetaries, faint material can be observed projected outside the body of the main H II nebulae. Nebulae reported to show faint halos include NGC 2392, 3242, 6309, 6543, 6804, 6720 and 7662 (Minkowski and Osterbrock, 1959; Millikan, 1974). These objects are known as double-shell or halo nebulae, and have received considerable attention. Kaler (1974) suggests that the double shell nebulae result from a double pulse planetary nebula ejection process. In the case of NGC 7027, Atherton et al. (1979) suggest that the halo is a reflection nebulosity probably unrelated to the inner planetary nebula except by coincidental proximity. Mathews (1966) notes that the halos may result from shock acceleration of the outer layers of the expanding primary shells. Kwok et al. (1978) suppose that the halos may be the illuminated escaping winds of the progenitor red giants.

An understanding of the halo nebulae may be important in the determination of the masses of the nebulae, and of their radii and lifetimes. Furthermore, since planetary nebulae are important contributors of material to the interstellar medium, the nature and frequency of occurrence of the halos may be of importance to the study of the mass balance of the interstellar medium. However, despite the numerous interpretations of the halo nebulae, relatively few such objects have been identified to the present time and their status as normal components of planetary nebulae is in doubt.

The present survey was designed to investigate a moderate number of planetary nebulae, in a sensitive and systematic way, in order to determine the true frequency of occurrence of halo structures. It was also hoped that by observing a number of these objects some common properties, indicative of the mode of origin, might be discerned.

2. Observations

2.1 Instrumentation

The observations were taken with a Texas Instruments 800 × 800 pixel charge coupled device (CCD) during June-July, 1982. This CCD detector was characterized by very low readout noise (~ 10 electrons per pixel), good linearity of response ($\sim 0.1\%$), high sensitivity (quantum efficiency ~ 0.6 at $0.65\,\mu$m wavelength) and large dynamic range (~ 5000). Dark current was effectively eliminated by cooling the detector to 150 K with liquid nitrogen. For the present observations the CCD was mounted inside the versatile camera 'PFUEI' (Gunn and Westphal, 1981). PFUEI permitted observations in two distinct modes. As a camera the instrument was used to obtain direct images through narrow bandpass interference filters. As a spectrograph PFUEI was used to obtain low spectral resolution slit spectra of selected regions of the nebulae.

Most of the observations were acquired with the PFUEI at the Cassegrain focus of the 1.5 m telescope at Palomar Observatory. The f/8.75 focal ratio of the telescope was reduced to f/3.75 by a system of lenses in the PFUEI: the resulting image scale was 0.55 arcsecond per 15 μm pixel at 0.65 μm wavelength. The field size was 440 arcsecond square. In addition, a smaller number of observations were taken at the prime focus of the Hale 5.1 m telescope. With the Wynne corrector lens and PFUEI in place an effective focal ratio of f/1.4 was obtained. The corresponding image scale and field width were 0.42 arcsecond per pixel and 340 arcsecond, respectively. At both telescopes the final spatial resolution was determined by the atmospheric seeing. A journal of observations is given in Table I.

2.2 Images

Planetary nebulae were selected from the atlas of Perek and Kohoutek (1967) according to two criteria: (1) the position of each object was chosen to satisfy the conditions

$$16^{\mathrm{h}}00^{\mathrm{m}} \lesssim \alpha_{1950} \lesssim 24^{\mathrm{h}}00^{\mathrm{m}} \quad \text{and} \quad -25^{\circ}00' < \delta_{1950}$$

where α_{1950}, δ_{1950} are the right ascension and declination of the nebula at epoch 1950, and (2) the longest dimension of the nebular image, l (arcseconds), was chosen to be in the range

Table I. *Journal of Observations*

UT Date, 1982	Telescope (m)	Seeing FWHM (arcsecond)	Sky Conditions	Work[1]
19-20 June	1.5	2.0	Cloud to photometric	Hα
22-23 June	1.5	1.0 to 2.0	Photometric	Hα
23-24 June	1.5	1.0	High cirrus	Hα POL
24-25 June	1.5	2.0	Photometric to cirrus	Hα, Hα POL
28-29 June	5.1	1.0	Photometric to cirrus	Hα
18-19 July	1.5	1.5	Photometric	Hα
19-20 July	1.5	2.0	Photometric	Hα
20-21 July	1.5	1.0	Photometric to cloud	Hα
21-22 July	1.5	1.5	Cirrus	Sp
22-23 July	1.5	1.2	Cirrus	Sp
23-24 July	1.5	1.8	Cloud	Sp
24-25 July	1.5	1.0 to 1.5	Photometric	Hα
26-27 July	1.5	1.5	Photometric	Hα, Sp
27-28 July	1.5	1.0	Photometric	Hα, Sp

[1] Hα, direct imaging; Hα POL, direct imaging through polarizer; Sp, spectrography.

$$10 \lesssim l \lesssim 200 \quad .$$

The latter criterion was implemented to ensure that a reasonable number of resolution elements were present across each nebular image and to exclude those nebulae which were substantially larger than the field of view (in retrospect, some nebulae proved to extend beyond the field of view at very low surface brightness levels).

Observations in the direct camera mode were all taken through an interference filter centered at 6560 Å and having a FWHM = 98 Å and a peak transmission of 58%. This filter passed the Hα λ 6563 emission line as well as the [N II] λλ 6548, 6583 emission lines from the nebulae together with some nebular continuum.

In the imaging mode, short exposures were used to find and center each object in the field of view. A guide star was then acquired in an adjustable field eyepiece and was locked into position. In a few cases guiding was rendered impossible by the absence of suitable field stars. Exposures of 1200 second duration were taken on each nebula. Additional shorter exposures of nebulae having very high surface brightness were taken to prevent saturation of the CCD. The images were photometrically calibrated by taking short exposures of the standard stars BD+17°4708 and BD+26°2606. Flat field frames were recorded each time the PFUEI was mechanically adjusted in order to permit the subsequent removal of pixel to pixel response variations from the data frames. Numerous zero exposure 'erase' frames were also recorded to permit subtraction of the bias level from the CCD.

Two bright nebulae with halos were imaged through a polarizing sheet to attempt to detect gross polarization of the radiation. The polarizer was rotated

90° between exposures and separate flat fields were recorded for each polarizer orientation. The data were not absolutely calibrated — instead the field stars within each image were used to provide relative intensity calibration between the two polarization frames. It was assumed that the field stars did not exhibit gross intrinsic polarization.

2.3 Low Resolution Spectra

Low resolution spectra were taken of many of the imaged nebulae in order to estimate the nebular electron densities from the [S II] λ 6716, 6731 line ratio. The dispersing element was a 600 lines per millimeter grating blazed at 5700 Å. It gave a dispersion of 4.3 Å per pixel and a useful wavelength range from 4300 Å to 7100 Å. The spectral resolution was determined by the width of the entrance slit. A 1 arcsecond wide slit was used: the resulting spectrum lines had FWHM = 1.5 pixel corresponding to 6.4 Å. This resolution was sufficient to allow clear separation of the 6716, 6731 Å lines of [S II]. The 240 arcsecond long slit permitted the simultaneous recording of the spectra of widely separated regions of each nebula, with seeing limited spatial resolution along the length of the slit. In most cases the slit was long enough to project onto the adjacent sky, thereby providing an independent, simultaneous night sky spectrum.

The positioning of the spectrograph slit on each nebula was achieved by using PFUEI as a direct finder camera. PFUEI was then converted to a spectrograph and a short exposure was taken to confirm the correct positioning of the slit (usually by noting the location and appearance of the spectrum of the central star of the planetary). The positioning was found to be accurate to better than 1 arcsecond in declination and to about 1 arcsecond in right ascension. The slit was oriented east to west for all the observations reported here. Rather long exposures (1200 to 3600 seconds) were obtained to attempt to achieve good signal strengths in the [S II] lines. Flat field and erase frames were recorded in the same manner as for the direct frames. No attempt was made to obtain absolute flux calibration for the spectra, such calibration being precluded by the very narrow slit and by atmospheric effects.

3. Results

3.1 (H I + [N II]) Images

Images of 44 nebulae in the light of H I + [N II] are presented in Figure 1. The figure should be read from left to right then from top to bottom. Each image is shown in two versions in order to provide a basis for the systematic intercomparison of the nebulae. The first image of each object is a 'stretch' between the sky brightness and the brightest part of the nebula, i.e: it displays all of the data numbers in the image of the nebula. In the second image the lowest 10% of the data numbers are displayed; those above have been set equal to white in the figure. This presentation has the advantage of emphasizing the bright primary structures in the first image and the faint, secondary halos in the second. In a few nebulae, very faint halos are not well seen in either stretch of Figure 1. These halos are more clearly evident in Figure 2, where only the lowest 1% of the data numbers are displayed. In both figures, pixels which are saturated in the raw data appear black. Strongly saturated images appear elongated east-west due to a property of the detector. Each nebula is accompanied by a scale bar of 20 arcsecond length and by a designation from the Perek and Kohoutek catalog.

The nebulae shown in Figure 1 exhibit a wide range of morphologies. For example, centrally condensed, ring, bipolar and irregular nebulae are all present

Figure 1. CCD images of planetary nebulae. Each nebula is shown twice. The left hand image shows all data numbers between the sky brightness and the peak nebular brightness; the right hand image shows the lowest 10% of the data numbers. The left hand image emphasizes the primary nebula, whereas the right hand image emphasizes the halo in nebulae where one is present. Each picture has north to the top, east to the left. The scale bars are each 20 arcseconds long.

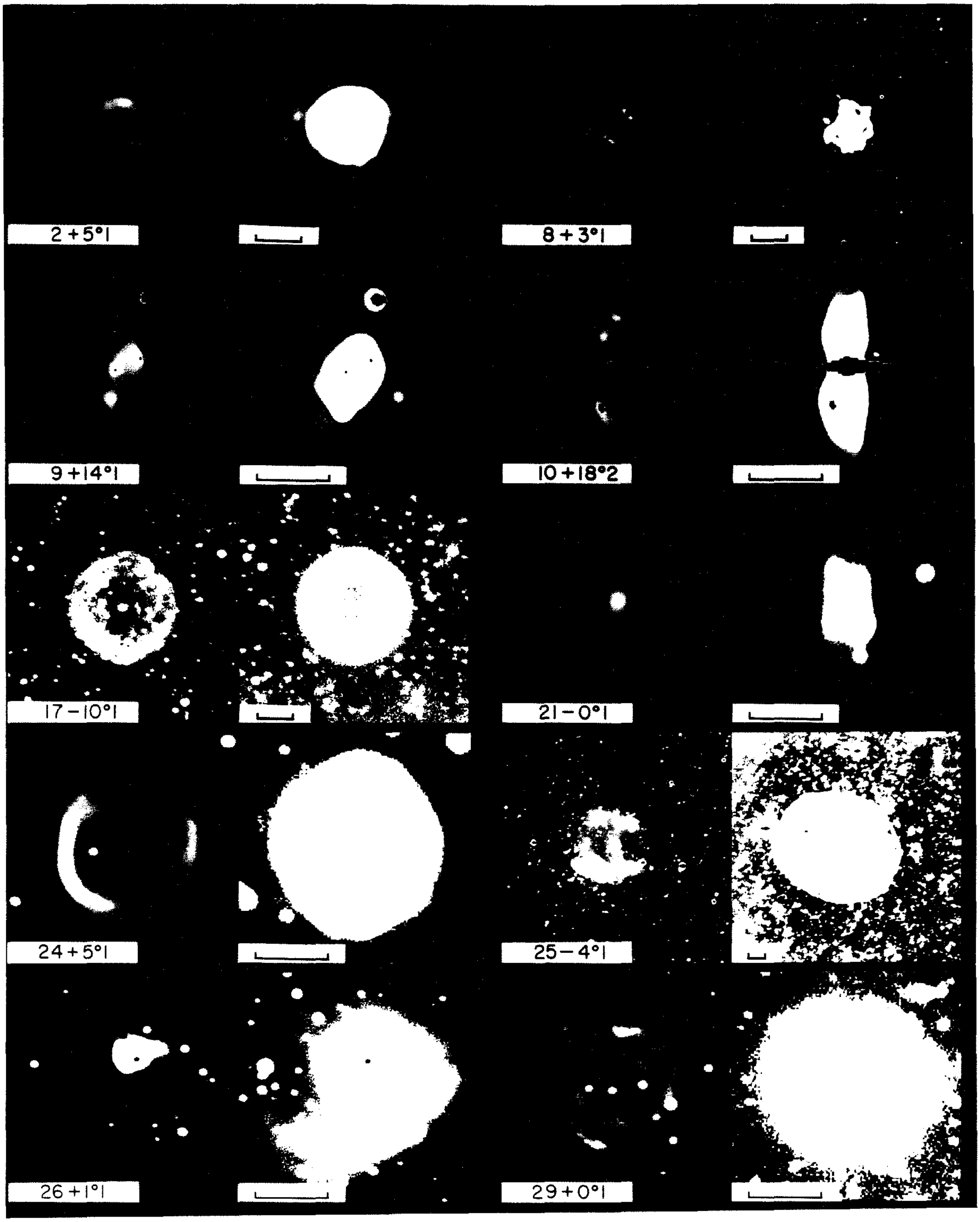
2+5°1
8+3°1
9+14°1
10+18°2
17-10°1
21-0°1
24+5°1
25-4°1
26+1°1
29+0°1

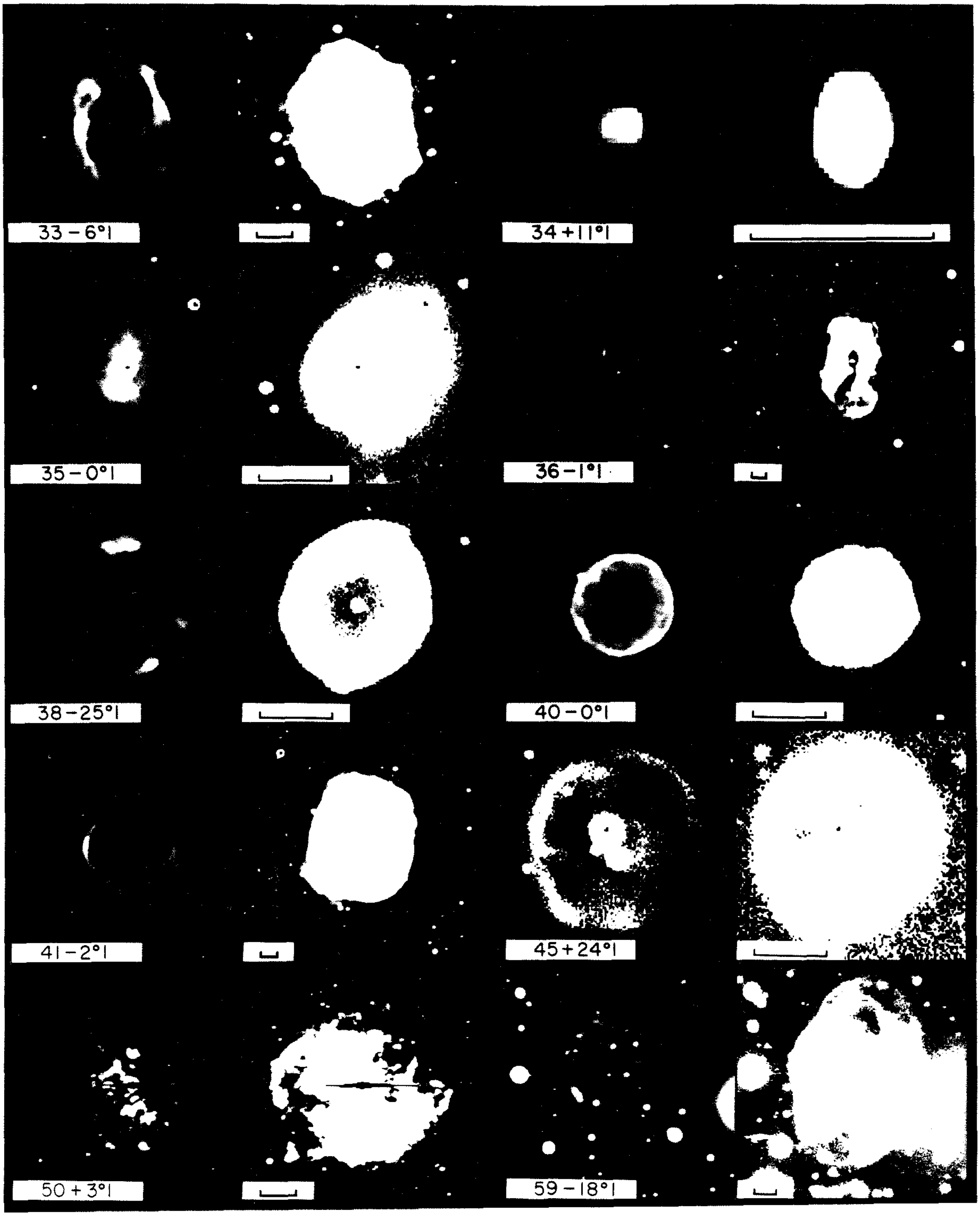
33 − 6°1
34 + 11°1
35 − 0°1
36 − 1°1
38 − 25°1
40 − 0°1
41 − 2°1
45 + 24°1
50 + 3°1
59 − 18°1

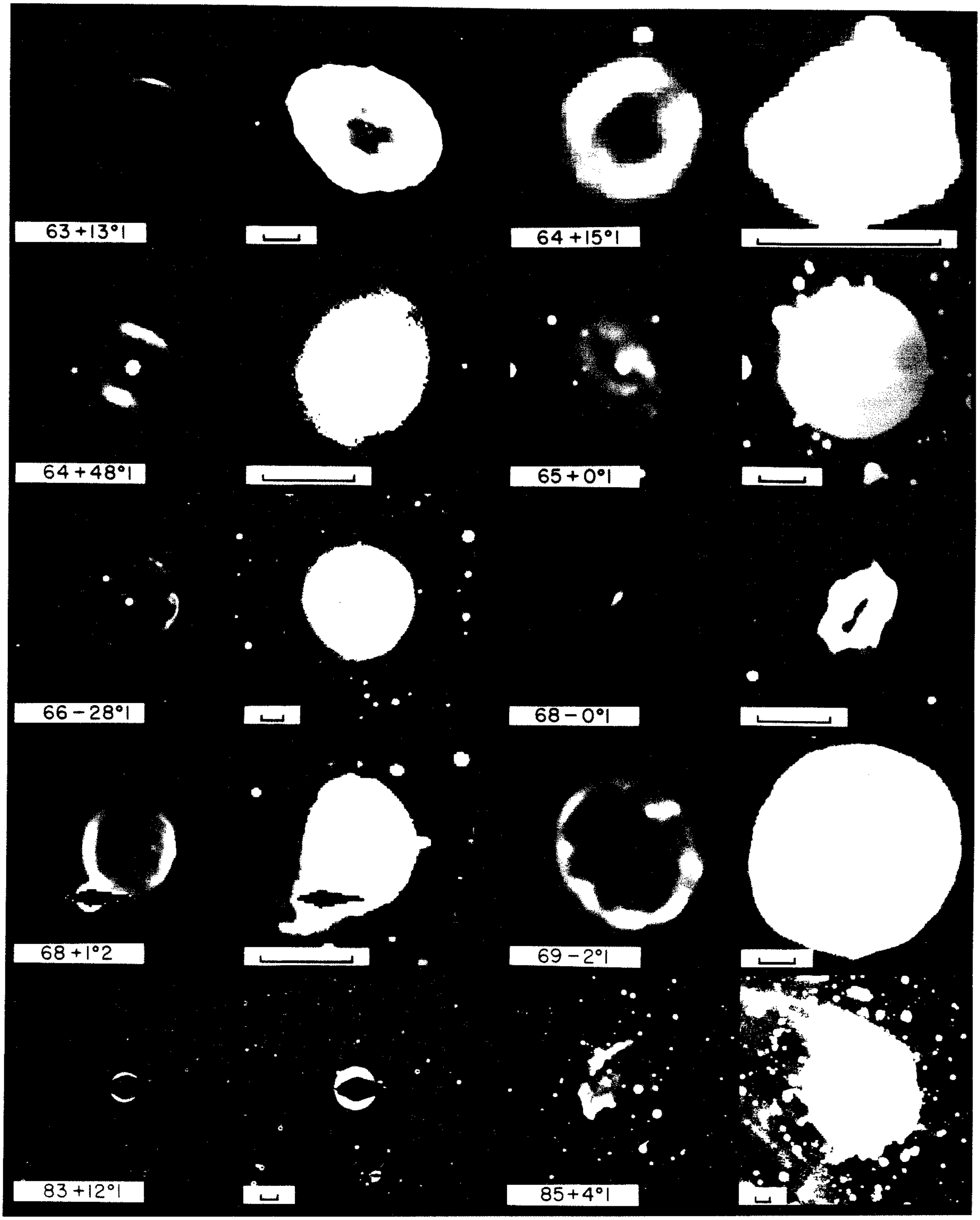
63 + 13°1
64 + 15°1
64 + 48°1
65 + 0°1
66 − 28°1
68 − 0°1
68 + 1°2
69 − 2°1
83 + 12°1
85 + 4°1

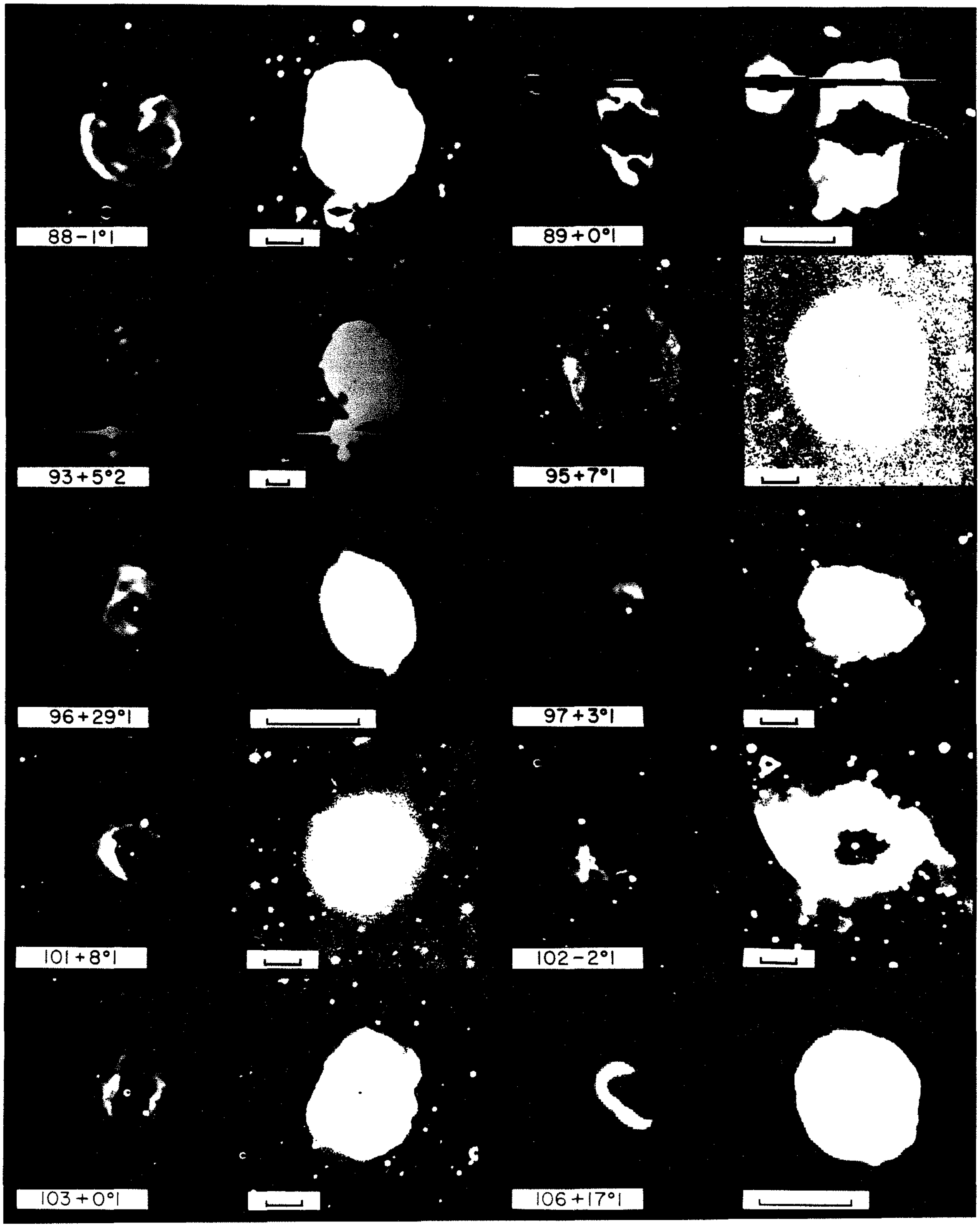
88−1°1
89+0°1
93+5°2
95+7°1
96+29°1
97+3°1
101+8°1
102−2°1
103+0°1
106+17°1

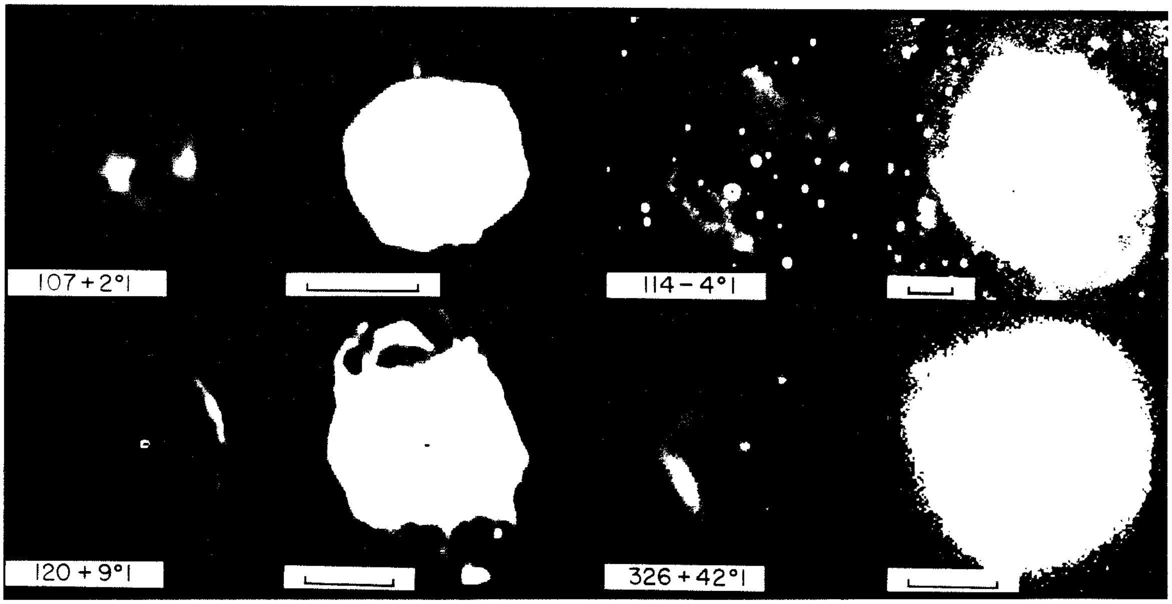
107+2°1
114-4°1
120+9°1
326+42°1

Figure 2. Stronger stretches of nebulae shown in Figure 1. Only the lowest 1% of the data numbers are shown. The images emphasize very faint halos not well seen in Figure 1. North is to the top, east to the left. The scale bars are each 20 arcseconds long.

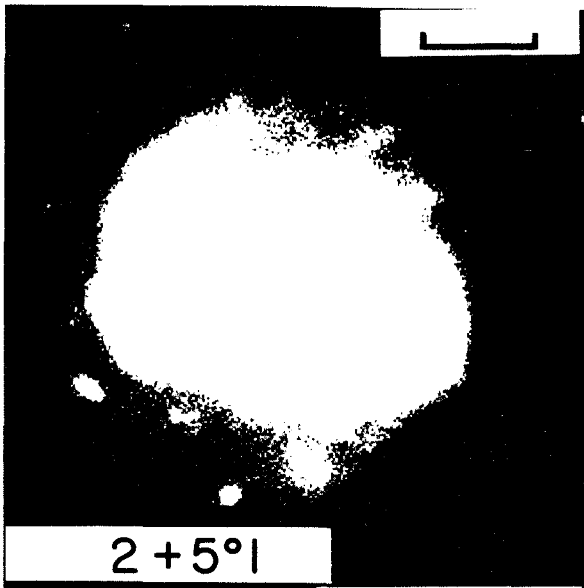

2+5°1

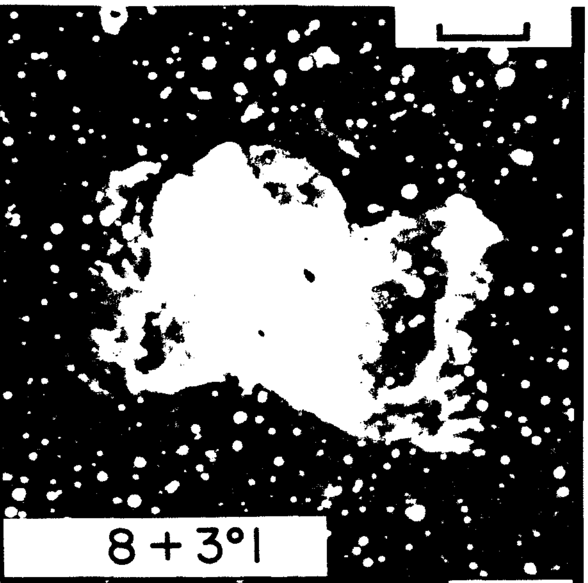

8+3°1

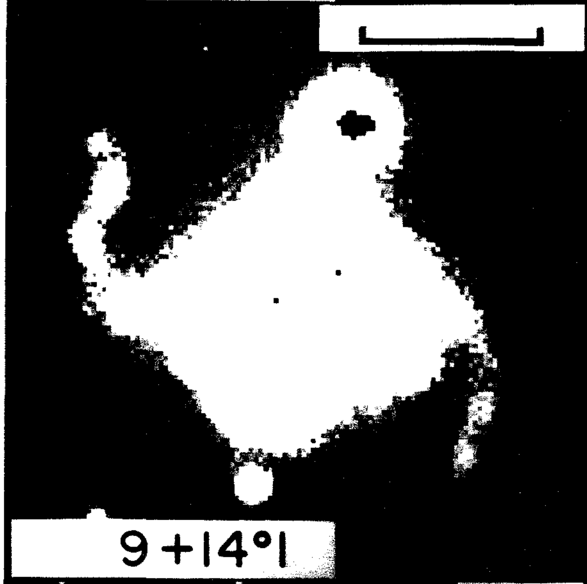

9+14°1

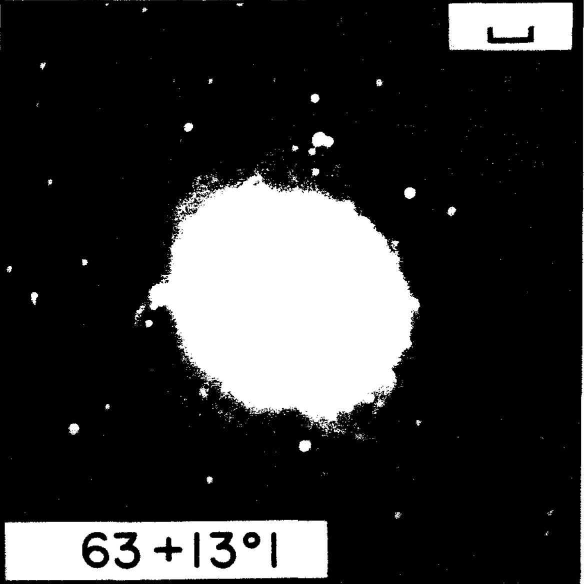

63+13°1

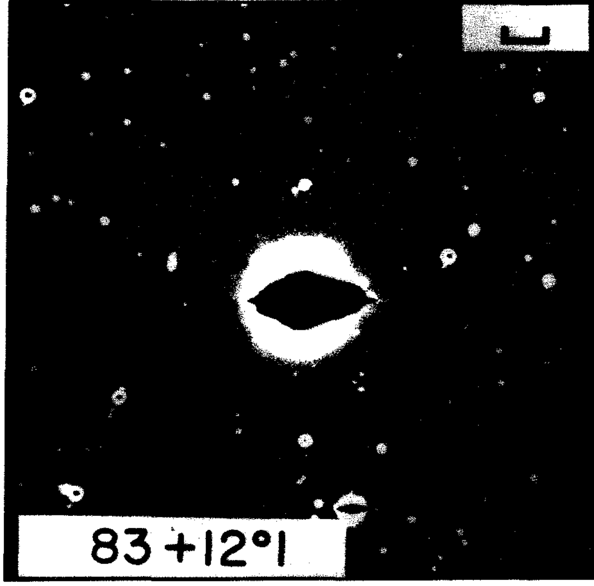

83+12°1

in the sample (see, for example, 21-0°1, 40-0°1, 10+18°2 and 85+4°1, respectively). It is possible, though unlikely, that a few of the objects selected from the Perek and Kohoutek catalog are not true planetary nebulae. Such pronounced variations of appearance make the intercomparison of the nebulae very difficult. In addition the nebulae exhibit great structural complexity which thwarts much quantitative analysis of the images. In this work we are mostly concerned with ascertaining the gross properties of the halos. Consequently, we elect to describe each nebula by a few readily measured parameters, even though these may not fully reflect the true complexities evident in the images. The basic parameters have been chosen as follows:

a,b ; the semimajor and semiminor axes of the best fit ellipse to the 10% isophote.

p,q ; the semimajor and semiminor axes of the best fit ellipse to the outer edge of the halo material, where a halo is observed.

φ ; the position angle of the major axis of the best fit ellipse to the 10% isophote.

The 10% isophotes are close to the outer boundaries of most of the primary nebulae. Consequently, the 10% isophotes have been selected to provide a working definition of the outer boundaries. From the above quantities, which serve to describe the shapes of the primary nebulae and their halos, several secondary quantities have been computed and are listed in Table 2. These are

e_p, e_H ; the ellipticities of the primary nebulae and halos.

R_H/R_p ; the ratio of the averaged semiaxes of the primary nebulae and halos.

The ellipticities have been defined through

Table 2. *Properties of Nebulae.*

Object	Name	α_{1950}	δ_{1960}	l^{II}	b^{II}	φ	ϑ	Halo	Δ (kpc)	Type	R_p	R_h	R_h/R_p	R_p (pc)	e_p	e_H
2+ 5°1	6369	17 26.3	-23°43'	2.44	+5.85	74	-72	Y	1.2	R	17	34	2.00	0.10	0.31	0.42
8+ 3°1	6445	17 46.3	-20 00	8.07	+3.90	-10	21	Y	1.35	R	18	106	5.89	0.12	0.65	0.40
9+14°1	6309	17 11.3	-12 51	9.66	+14.81	-20	13	Y	2.6	I,C	16	45	2.81	0.20	0.85	0.81
10+18°2	M2-9	17 02.9	-10 04	10.91	+18.06	0	33	N	2.75	B	13	—	—	0.17	0.98	—
17-10°1	A51	18 58.1	-18 17	17.61	-10.24	—	—	N	—	R	31	—	—	—	0.19	—
21- 0°1	M3-28	18 29.9	-10 08	21.82	-0.47	0	28	Y	2.3	C	4	14	3.50	0.04	0.71	0.92
24+ 5°1	M4-9	18 11.6	-05 00	24.22	+5.95	-10	18	N	1.3	R	21	—	—	0.13	0.55	—
25- 4°1	K4-8	18 51.6	-08 51	25.42	-4.63	65	-88	Y	—	R	45	65	1.44	—	0.52	0.62
26+ 1°1	V-V1-8	18 30.6	-05 00	26.44	+1.77	-30	-2	Y	1.0	I	—	> 240	—	—	—	—
29+ 0°1	A48	18 40.2	-03 16	29.09	+0.45	60	87	N	—	R	10	—	—	—	0.65	0.60
33- 6°1	6772	19 12.0	-02 47	33.17	-6.38	10	37	Y	1.25	R	37	54	1.46	0.22	0.17	0.80
34+11°1	6572	18 09.7	+06 50	34.62	+11.84	-5	22	N	0.67	C	7	—	—	0.02	0.75	—
35- 0°1	Ap2-1	18 55.6	+01 33	35.13	-0.75	-60	-23	Y	—	C	14	19	1.36	—	0.57	0.54
36- 1°1	Sh2-71	18 59.5	+02 05	36.06	-1.37	-10	17	Y	—	R	67	194	2.90	—	0.84	0.40
38-25°1	A70	20 28.9	-07 16	38.11	-25.47	-25	2	N	—	R	21	—	—	—	0.55	—
40- 0°1	A53	19 04.3	+06 19	40.37	-0.47	—	—	N	—	R	15	—	—	—	0.00	—
41- 2°1	6781	19 16.0	+06 27	41.84	-2.98	-16	13	Y	0.80	R	60	79	1.32	0.23	0.49	0.77
45+24°1	K1-14	17 40.4	+21 28	45.59	+24.33	-20	1	N	—	R	26	—	—	—	0.20	—
50+ 3°1	M1-67	19 09.3	+16 47	50.21	+3.31	30	58	N	0.85	IR	57	—	—	0.18	0.40	—
59-18°1	A72	20 47.7	+13 22	59.80	-18.74	-15	20	N	—	R?	111	—	—	—	0.86	—
63+13°1	6720	18 51.7	+32 58	63.17	+13.98	60	84	Y	0.57	R	39	74	1.90	0.11	0.65	0.61
64+15°1	M1-64	18 48.2	+35 11	64.98	+15.53	-40	-17	Y	2.5	R	9	15	1.67	0.11	0.55	0.00
64+48°1	6058	16 02.7	+40 49	64.67	+48.30	-25	-22	Y	2.6	R	10	15	1.50	0.13	0.52	0.62
65+ 0°1	6842	19 53.0	+29 09	65.91	+00.60	—	—	Y	1.27	R	13	29	2.23	0.08	0.70	0.43
66-28°1	7094	21 34.5	+12 34	66.79	-28.21	—	—	N	1.3	R	49	—	—	0.31	0.18	—
68-0°1	M1-75	20 02.8	+31 19	68.86	-0.05	-30	3	Y	2.8	R	8	21	2.63	0.11	0.82	0.94
68+ 1°2	He1-4	19 57.3	+31 47	68.63	+1.19	-30	2	Y	1.8	R	11	14	1.27	0.10	0.50	0.38
69- 2°1	6894	20 14.4	+30 25	69.48	-2.62	—	—	Y	1.41	R	20	31	1.55	0.14	0.57	0.31
83+12°1	6826	19 43.5	+50 24	83.56	+12.78	—	—	Y	1.02	C?	≲13	69	≳5.3	—	—	0.00
85+ 4°1	A71	20 30.8	+47 11	85.01	+4.49	20	56	Y	—	I	106	> 220	> 2.08	—	0.67	—
88- 1°1	7048	21 12.4	+46 04	88.76	-1.68	15	59	Y	1.3	R?	35	54	1.54	0.22	0.64	0.48
89+ 0°1	7026	21 04.6	+47 39	89.00	+0.37	-5	37	Y	1.67	R?	—	20	—	—	—	0.83
93+ 5°2	7008	20 59.1	+54 21	93.42	+5.49	15	56	Y	—	I	40	60	1.50	—	0.60	0.73
95+ 7°1	A73	20 55.2	+57 15	95.27	+7.80	15	55	N	—	R	40	—	—	—	0.49	—
96+29°1	6543	17 58.6	+66 38	96.47	+29.95	20	20	Y	0.65	R	6	12	2.00	0.02	0.80	0.79
97+ 3°1	A77	21 30.6	+55 40	97.52	+3.18	80	-53	N	—	I	28	—	—	—	—	—
101+ 8°1	A75	21 25.2	+62 40	101.85	+8.74	—	—	Y	—	I	18	35	1.94	—	0.62	0.00
102- 2°1	A79	22 24.4	+54 34	102.98	-2.33	65	-57	N	—	IR	25	—	—	—	0.40	—
103+ 0°1	M2-51	22 14.3	+57 14	103.23	+0.68	-20	36	Y	1.6	R	16	38	2.38	0.12	0.89	0.72
106-17°1	7662	23 23.5	+42 16	106.56	-17.60	35	-75	Y	1.15	R	7	17	2.43	0.04	0.75	0.48
107+ 2°1	7354	22 38.5	+61 01	107.84	+2.31	—	—	Y	1.6	I?	10	21	2.10	0.08	0.59	0.44
114- 4°1	A82	23 43.4	+56 47	114.07	-4.68	40	-65	Y	—	B	42	53	1.28	—	0.27	0.72
120+ 9°1	40	00 10.3	+72 15	120.02	+9.87	20	-79	N	0.92	R?	25	—	—	0.11	0.81	—
326+42°1	I972	14 01.7	-17 01	326.75	+42.21	—	—	Y	2.0	R	24	26	1.08	0.23	0.36	0.39

$$e_p = \left\{1 - (a/b)^2\right\}^{1/2} \quad , \quad e_H = \left\{1 - (p/q)^2\right\}^{1/2}$$

and the equivalent circular semi-axes through

$$R_p = (ab)^{1/2} \quad , \quad R_H = (pq)^{1/2}$$

Other quantities listed in Table 2 include:

Column 1	Object designation from the Perek and Kohoutek (1967) catalog
Column 2	Alternative designations
Columns 3,4	α, δ: right ascension and declination (epoch 1950) of each nebula from Perek and Kohoutek
Columns 5,6	l^{II}, b^{II}: galactic longitude and latitude of each nebula
Column 7	φ, the position angle of the long axis of the primary nebula
Column 8	ϑ, the angle between the long axis and the galactic equator
Column 9	An indication of whether a halo is (Y) or is not (N) present
Column 10	Δ, the heliocentric distance of the nebula where known, from Acker (1979)
Column 11	The morphological type of the primary nebula determined by inspection of the CCD images. R = Ring, I = Irregular, C = Centrally condensed, B = Bipolar

We refer to any material which extends clearly beyond the outer boundary of a primary nebula as halo material. Excellent examples, shown in Figure 1, are found in the nebulae 2+5°1, 8+3°1, 33-6°1, 36-1°1, 64-28°1, 69-2°1, 83+12°1, 85+4°1, 89+0°1 and 106-17°1. In some nebulae the halos are circularly symmetric (e.g. 69-2°1, 83+12°1, 106-17°1) whereas in others the halos have an irregular or filamentary appearance and do not exhibit circular symmetry (e.g. 2+5°1, 8+3°1, 85+4°1). At least two extreme interpretations of the more irregular halos are possible: either (a) the irregular appearance is due to a truly irregular distribution of matter in the halos or (b) the irregular appearance results from azimuthal variations of the radial Lyman limit optical depth in the primary nebulae. The former case would correspond to a "density bounded" nebula, the latter to a "radiation bounded" nebula. In the latter case a complete spherical shell halo would appear to be irregular as a result of the patchy shadowing of ionizing radiation by material in the primary shell. Plausible examples of shadowing are found in 41-2°1 and 88-1°1. In both nebulae the azimuthal angles of faint sections of the primary nebulae are coincident with the azimuthal angles of bright sections of the respective halos. Other possible examples may be found in 8+3°1, 36-1°1, 68-0°1, 103+0°1 and 114-4°1. Counter examples may be found in 33-6°1, 64+48°1 and 106-17°1.

The frequency distribution of the ratio R_H/R_p is plotted in Figure 3. The range is $1.2 \lesssim R_H/R_p \lesssim 5$ and the mean is 2.1 ± 0.2 ($n = 25$). Similarly, the ratio of the halo to primary nebula surface brightnesses I_H/I_p exhibits wide variations within the range $10^{-3} \leq I_H/I_p \leq 0.1$. The mean ellipticities of the primary nebulae and the halos are $\bar{e}_p = 0.57 \pm 0.04$ ($n = 40$) and $\bar{e}_{\mathrm{H}} = 0.54 \pm 0.05$ ($n = 28$), respectively. These means are the same within the uncertainties. Hence, there is no evidence for a systematic difference between the gross shapes of the primary nebulae and the halos.

The distribution of the orientations of the apparent long axes of the nebulae is shown in Figure 4. ϑ, the angle between the apparent long axis of each nebula and the galactic plane is also listed in Table 2. The dotted curve in Figure 4 represents the ϑ distribution to be expected if the nebular long axes

Figure 3. Distribution of the ratio of the halo radius R_{H} to the primary nebula radius R_p. The distribution is peaked toward small values of the ratio and has a mean equal to 2.

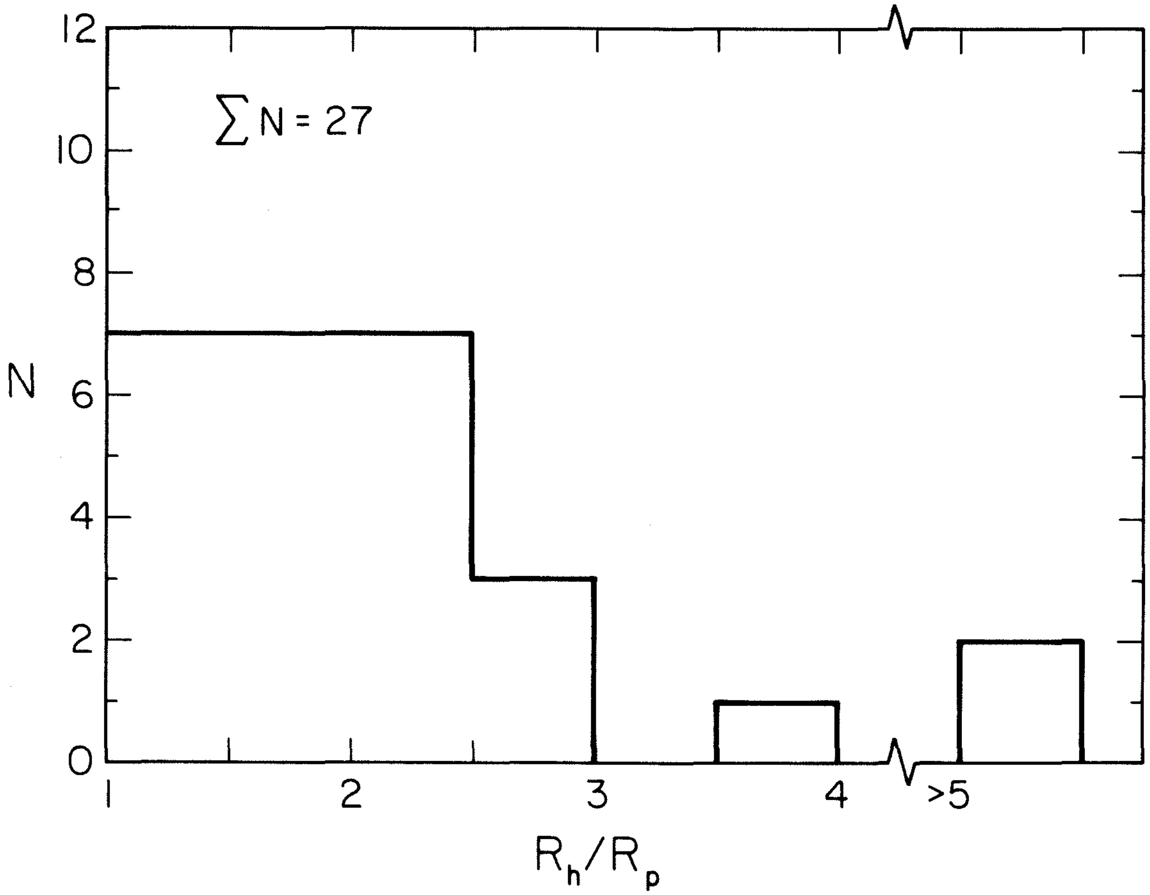
∑N = 27
N
0
2
4
6
8
10
12
1
2
3
4
>5
R_h/R_p

Figure 4. Distribution of the apparent long axes of planetary nebulae. The number of nebulae, N, having their longest axes inclined to the galactic equator at angle ϑ is shown. The dashed line depicts the distribution to be expected if the longest axes are randomly oriented. Within the statistical uncertainties the model and observed distribution are similar.

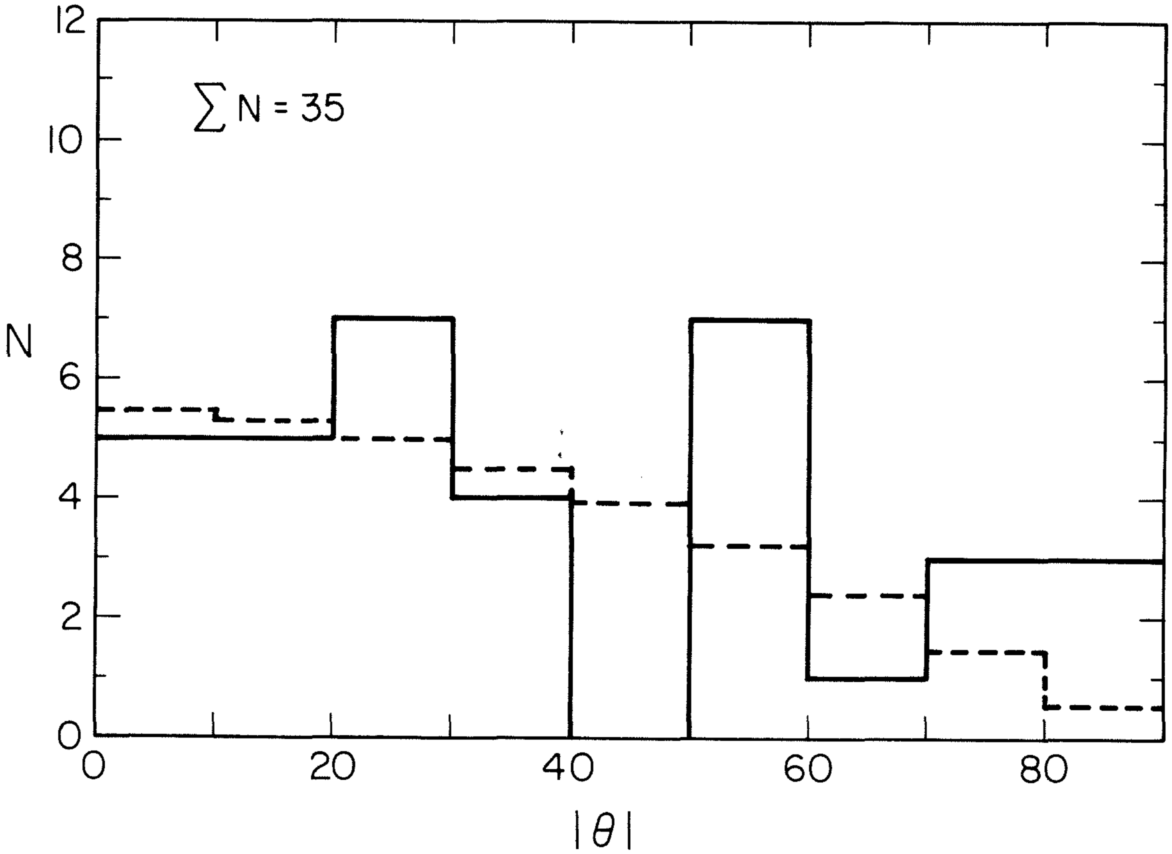
∑N = 35
N
|θ|
0
2
4
6
8
10
12
0
20
40
60
80

are distributed randomly in direction. Evidently the observed distribution is similar to the model curve, suggesting that there is no preferential alignment of the axes. This is opposite to the conclusion reached by Grinin and Zvereva (1967), who found the long axes of planetary nebulae to be preferentially aligned in the galactic plane. Such an alignment would have provided evidence for the control of nebular morphology by an external agency, possibly the interstellar magnetic field. However, external control is very implausible in view of the low value of the interstellar magnetic field strength.

The variation of the nebular surface brightness as a function of radial distance from the central star has been investigated by examination of nearly circularly symmetric nebulae possessing halos. The surface brightness, $B(\mathrm{r})$, was averaged around concentric circles centered on each nebula center. Figure 5 contains plots of $\log B(\mathrm{r})$ versus $\log(\mathrm{r})$ for six nebulae. The plots have been marked to show the location of the boundary between the primary nebula and the halo in each instance. The plots show that the surface brightness of the halos decreases sharply with r, often more quickly than the inverse fifth power of r.

The majority of the halos are too irregular to allow the construction of meaningful plots of the type presented in Figure 5. Large variations of surface brightness occur over small distances in the halos. A common feature of many of the halos, shown in Figures 1 and 2, is the presence of loop filaments. The loop filaments appear convex outward, have radii equal to a fraction of R_p, have widths comparable to the seeing and often appear to have centers of curvature close to the primary/halo boundaries. Examples may be seen in 2+5°1, 33-6°1, 68-0°1, 89+0°1, 103+0°1 and 120+9°1 (in Figure 1) and in 8+3°1, 9+14°1, 63+13°1 and 83+12°1 (in Figure 2). Many of the halo electron density

Figure 5. Azimuthally averaged Hα + [N II] surface brightness plots of circularly symmetric nebulae. The logarithm of the surface brightness is plotted against the logarithm of the radial distance from the central star in arcseconds. Vertical ticks mark the boundaries between primary and halo material in those nebulae which possess halos. Lines of slope -4 and -5 are shown for reference.

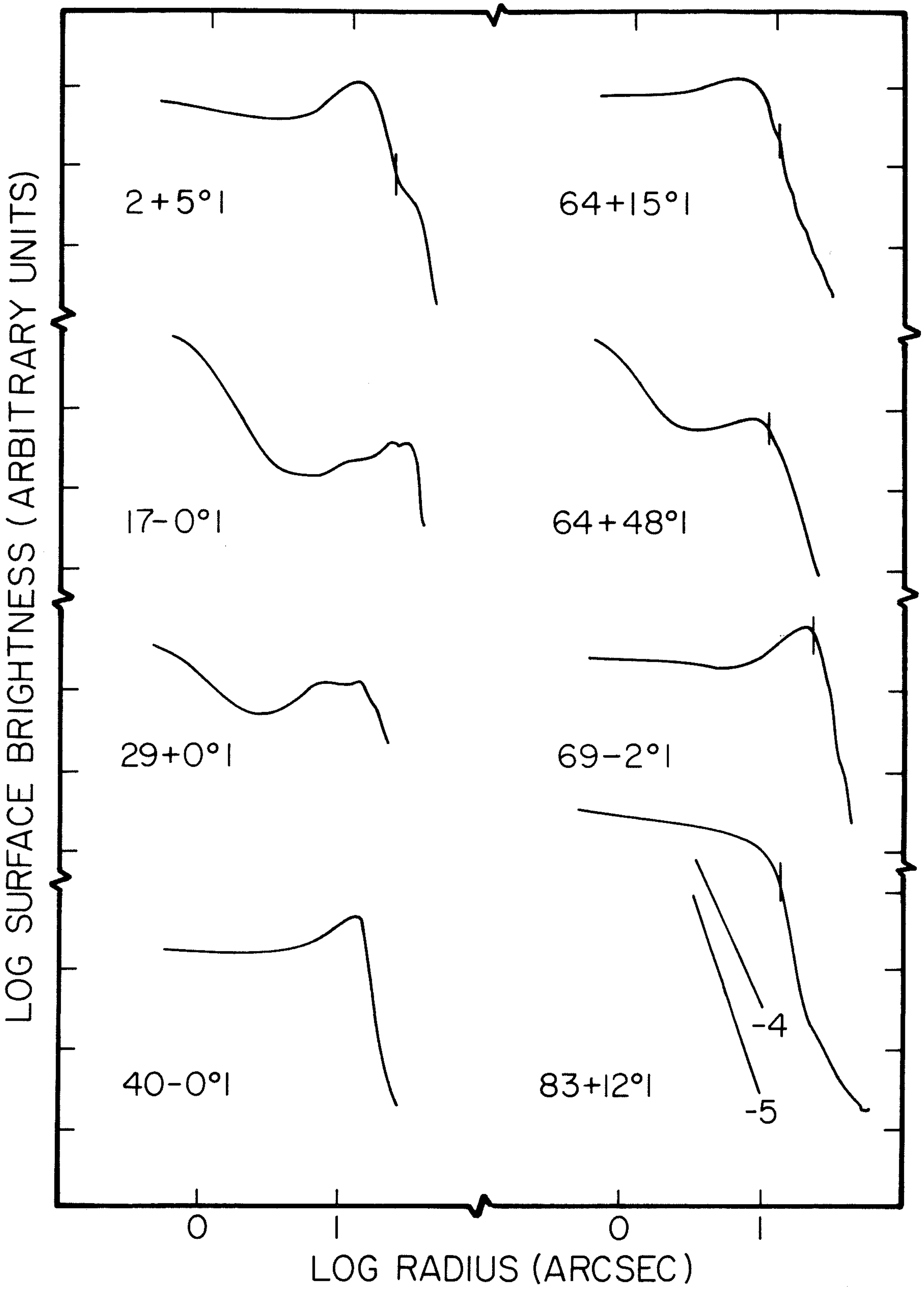
LOG SURFACE BRIGHTNESS (ARBITRARY UNITS)
2+5°1
64+15°1
17-0°1
64+48°1
29+0°1
69-2°1
40-0°1
83+12°1
-4
-5
0
1
0
1
LOG RADIUS (ARCSEC)

mesurements discussed in section 3.3 refer to loop filaments rather than to the fainter surrounding material. The origin of the loops is unclear but their resemblance to shock fronts is striking.

3.2 Polarizations

Images of the nebulae 63+13°1 and 64+48°1 taken through perpendicular polarizers were scaled by equalizing the intensities of field stars (assumed to have negligible polarization). Scale factors determined from different field stars were equal to within 1%. The scaled frames were then subtracted. Residual differences in the subtracted images were attributable to registration errors. They place an approximate upper limit to the degree of linear polarization present in the nebular H_α + [N II] radiation of $\lesssim 0.05$. The significance of the absence of larger polarization in the halos of these nebulae will be discussed in section 4.

3.3 Optical Spectra

The optical spectra were examined with the principal objective of measuring the halo electron densities. This was achieved by determination of the ratio of the intensities of the [S II] λλ 6716, 6731 lines. In the majority of the spectra, these lines were sufficiently faint that small scale variations along the spectrograph slit could not be separated from the pixel to pixel noise. In these spectra, the ratio of the line intensities was obtained by the averaging of long segments (typically ~ 10 arcsecond) of the slit images.

The unresolved electron density measurements are presented in Table 3. The contents of the table are as follows:

Column 1	Object designation from the Perek and Kohoutek (1967) catalog.
Column 2	$\Delta\alpha$ (arcsec): the offset of the center of the spectrograph

Table 3. Electron Density Measurements

Object	$\Delta\alpha$ (arcsec)	$\Delta\delta$ (arcsec)	L (arcsec)	r/R_p	Type	[S II] (6716/ 6731)	log N_e $(10^4/T_e)$ (m^{-3})
2+ 5°1	11W	ON	11	0.65	P	0.59 ± 0.06	$9.59^{+0.15}_{-0.11}$
	14E	ON	11	0.82	P	0.70 ± 0.07	$9.39^{+0.13}_{-0.14}$
	28W	ON	6	1.65	H	0.80 ± 0.20	$9.19^{+0.38}_{-0.35}$
	32E	ON	10	1.88	H	1.00 ± 0.10	$8.85^{+0.16}_{-0.15}$
10+18°2	0E	2N	5	0.15	P	0.51 ± 0.05	$9.81^{+0.24}_{-0.15}$
	7W	2N	9	0.56	P	0.64 ± 0.06	$9.50^{+0.11}_{-0.11}$
35- 0°1	10W	ON	8	0.71	P	0.89 ± 0.09	$9.02^{+0.18}_{-0.14}$
	13E	ON	16	0.93	P	0.86 ± 0.09	$9.08^{+0.17}_{-0.16}$
	25W	ON	22	1.79	H	1.14 ± 0.11	$8.63^{+0.17}_{-0.28}$
50+ 3°1	0E	12S	46	0.90	P	0.76 ± 0.08	$9.27^{+0.16}_{-0.15}$
68- 0°1	12E	ON	?	1.50	H	1.10 ± 0.11	$8.70^{+0.16}_{-0.23}$
	12E	12S	8	2.12	P	1.00 ± 0.10	$8.85^{+0.16}_{-0.15}$
68+ 1°2	0E	ON	12	0.00	P	0.96 ± 0.10	$8.91^{+0.17}_{-0.15}$
	10W	ON	8	0.91	P	0.94 ± 0.09	$8.94^{+0.16}_{-0.14}$
	13E	ON	8	1.18	P	0.98 ± 0.10	$8.88^{+0.16}_{-0.15}$
89+ 0°1	0E	ON	15	0.00	P	0.63 ± 0.06	$9.52^{+0.12}_{-0.11}$
	0E	12S	27		H	0.79 ± 0.08	$9.22^{+0.15}_{-0.16}$
97+ 3°1	17E	ON	29	0.61	P	1.29 ± 0.13	$8.22^{+0.37}_{-0.42}$
102- 2°1	22E	ON	23	0.88	P	1.16 ± 0.12	$8.59^{+0.20}_{-0.34}$
	29W	ON	24	1.16	P	1.20 ± 0.12	$8.49^{+0.24}_{-0.38}$
	48E	ON	10	1.92	P	1.25 ± 0.13	$8.35^{+0.31}_{-0.43}$
103+ 0°1	27W	6S	31	1.73	P	0.94 ± 0.09	$8.94^{+0.16}_{-0.14}$
107+ 2°1	6W	ON	8	0.60	P	0.68 ± 0.07	$9.43^{+0.12}_{-0.14}$
	11E	ON	13	1.10	P	0.58 ± 0.06	$9.61^{+0.16}_{-0.11}$

	slit from the central star, in right ascension.
Column 3	$\Delta\delta$ (arcsec): the offset of the center of the spectrograph slit from the central star, in declination.
Column 4	L (arcsec): the length of the slit along which the [SII] line intensities were averaged. The slit was always aligned East-West on the sky and was of 1 arcsec width.
Column 5	r/R_p: where $r = (\Delta\alpha^2 + \Delta\delta^2)^{1/2}$ is the summation between the central star and the effective center of the slit. R_p is the radius of the primary nebula in arcseconds (from Table 2).
Column 6	The type of material sampled by the spectrograph slit, either primary nebula (P) or halo (H).
Column 7	[SII] (6716/6731); the ratio of the intensities of the [SII] lines within the effective slit. The tabulated uncertainties were computed by assuming a statistical error distribution within the effective slit and are generally due to photon noise.
Column 8	$\log N_e$ (m^{-3}): the logarithm of the electron density within the effective slit, and its formal uncertainity. The electron density was estimated from the [SII] (6716/6731) line ratio using the transition probabilities calculated by Pradhan (1978).

An additional five nebulae had surface brightnesses high enough to permit the determination of spatially resolved electron densities. Results from these nebulae are not given in Table 3 but instead are plotted in Figures 6a-e. From these plots the general trend toward smaller electron densities in the

Figure 6. **Variation of [S II] λλ 6716, 6731 line intensity ratio and of electron** density, $\log N_e (m^{-3})$, as a function of distance along slits projected east-west on the surfaces of five nebulae. The points represent measurements along single lines of pixels parallel to the dispersion. The statistical uncertainties in the line ratio at each slit position are indicated by the local scatter of the measurements. Very uncertain measurements have been omitted for clarity. The continuous lines, where drawn, have been added to guide the eye.

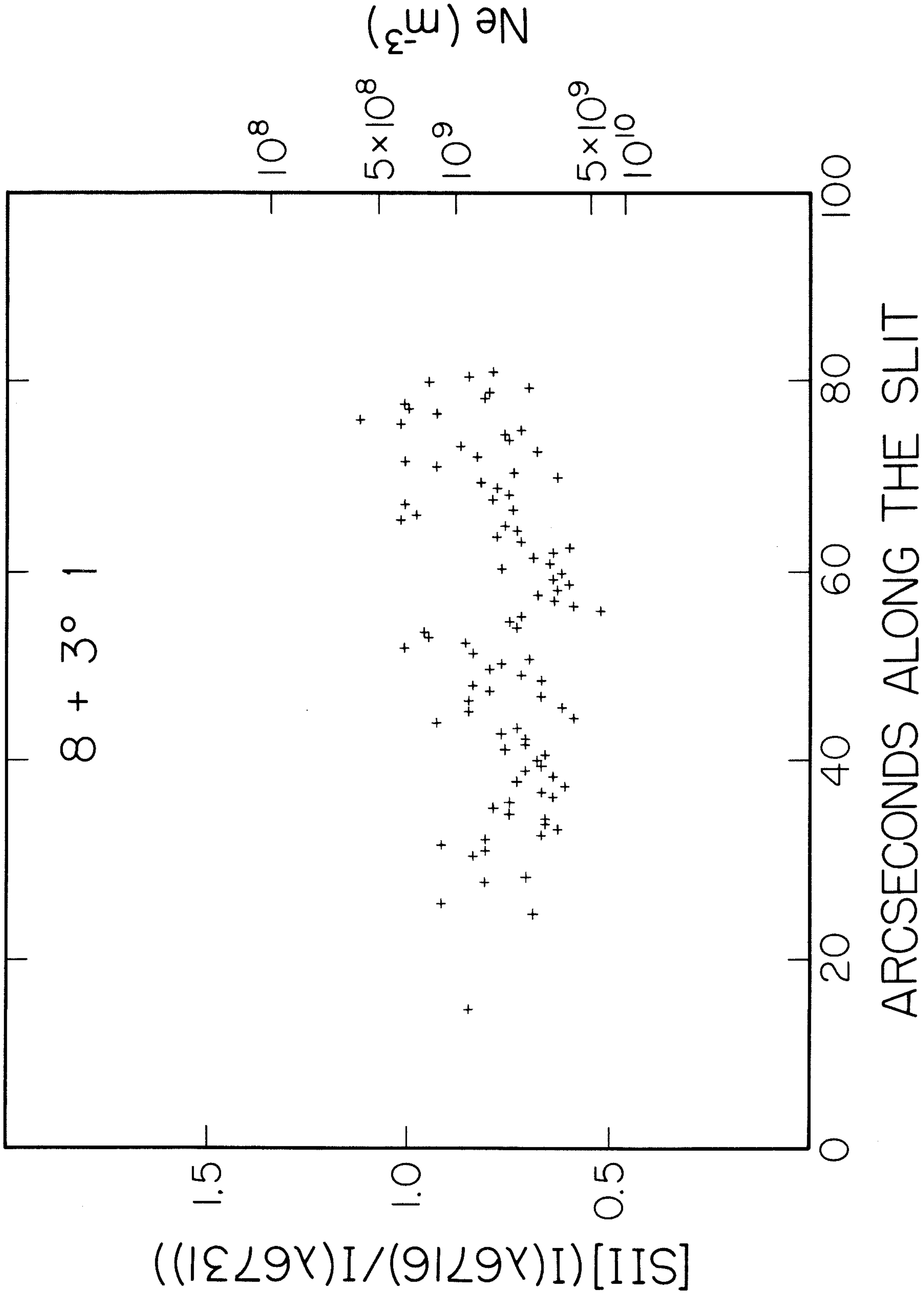
8 + 3° 1
[SII](I(λ6716)/I(λ6731))
1.5
1.0
0.5
ARCSECONDS ALONG THE SLIT
0
20
40
60
80
100
Ne (m⁻³)
10⁸
5×10⁸
10⁹
5×10⁹
10¹⁰

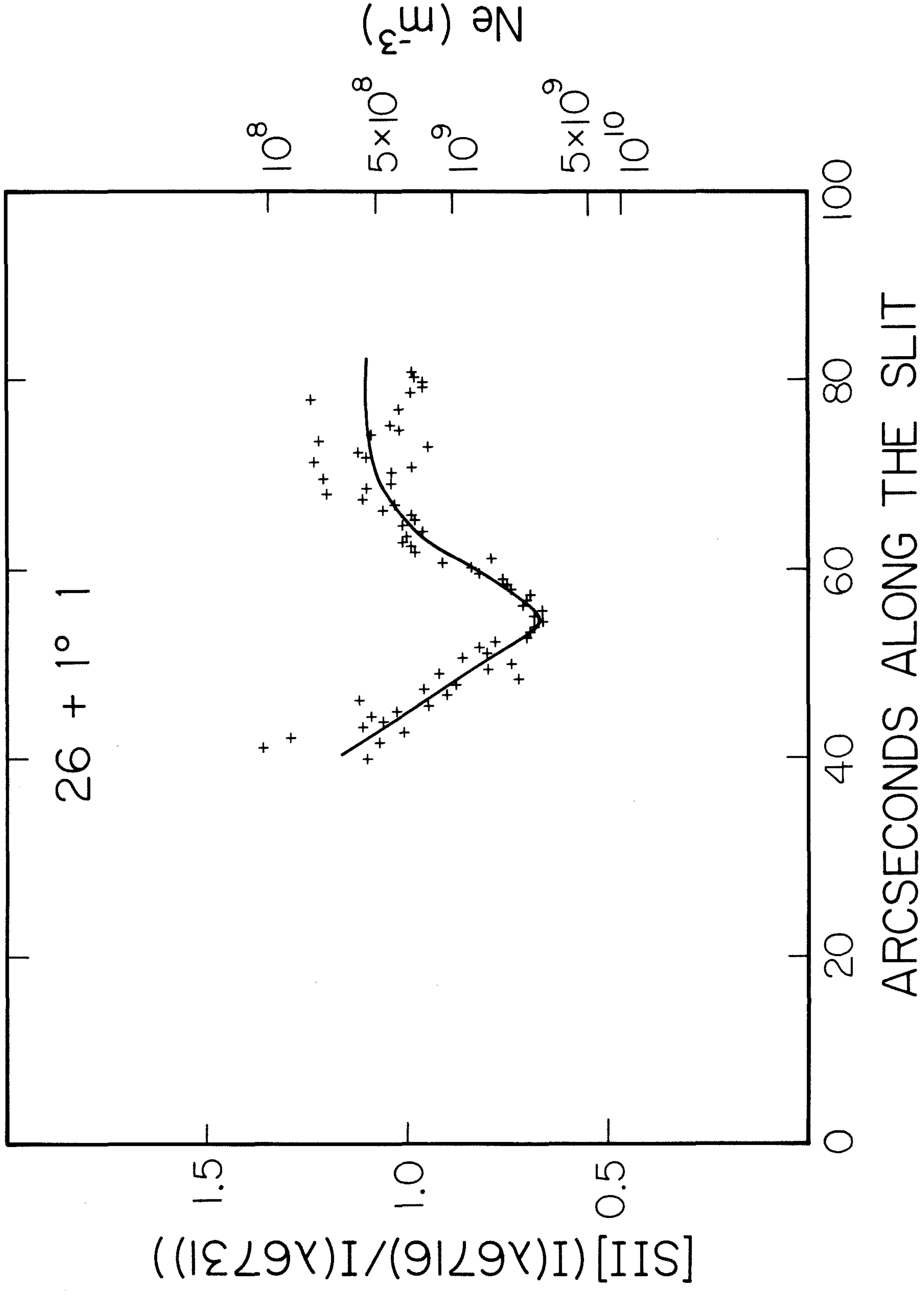
26 + 1° 1
ARCSECONDS ALONG THE SLIT
0
20
40
60
80
100
[SII] (I(λ6716)/I(λ6731))
1.5
1.0
0.5
Ne (m-3)
10^8
5×10^8
10^9
5×10^9
10^10

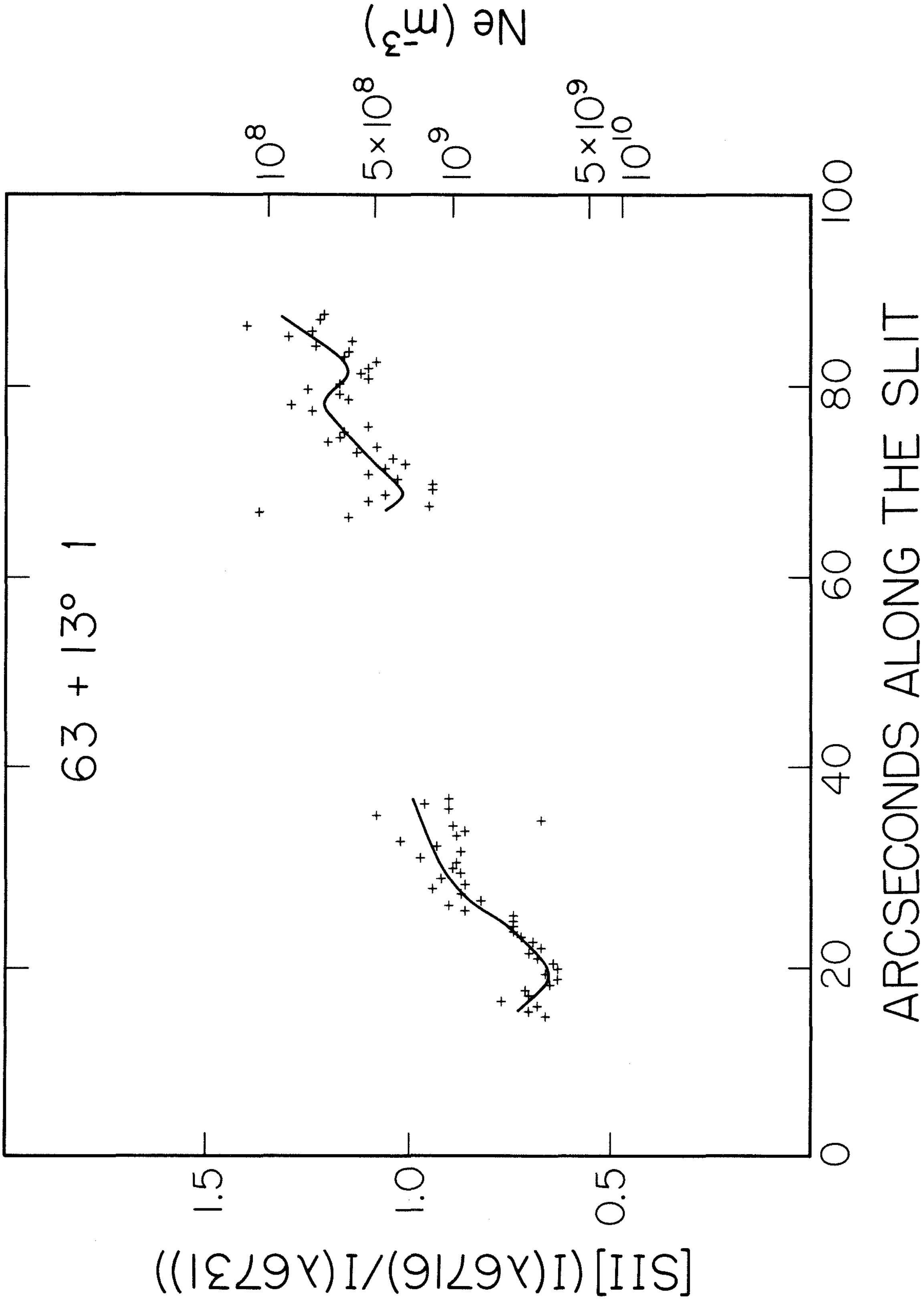
63 + 13° 1
Ne (m^{-3})
10^8
5×10^8
10^9
5×10^9
10^{10}
[SII](I(λ6716)/I(λ6731))
1.5
1.0
0.5
0
20
40
60
80
100
ARCSECONDS ALONG THE SLIT

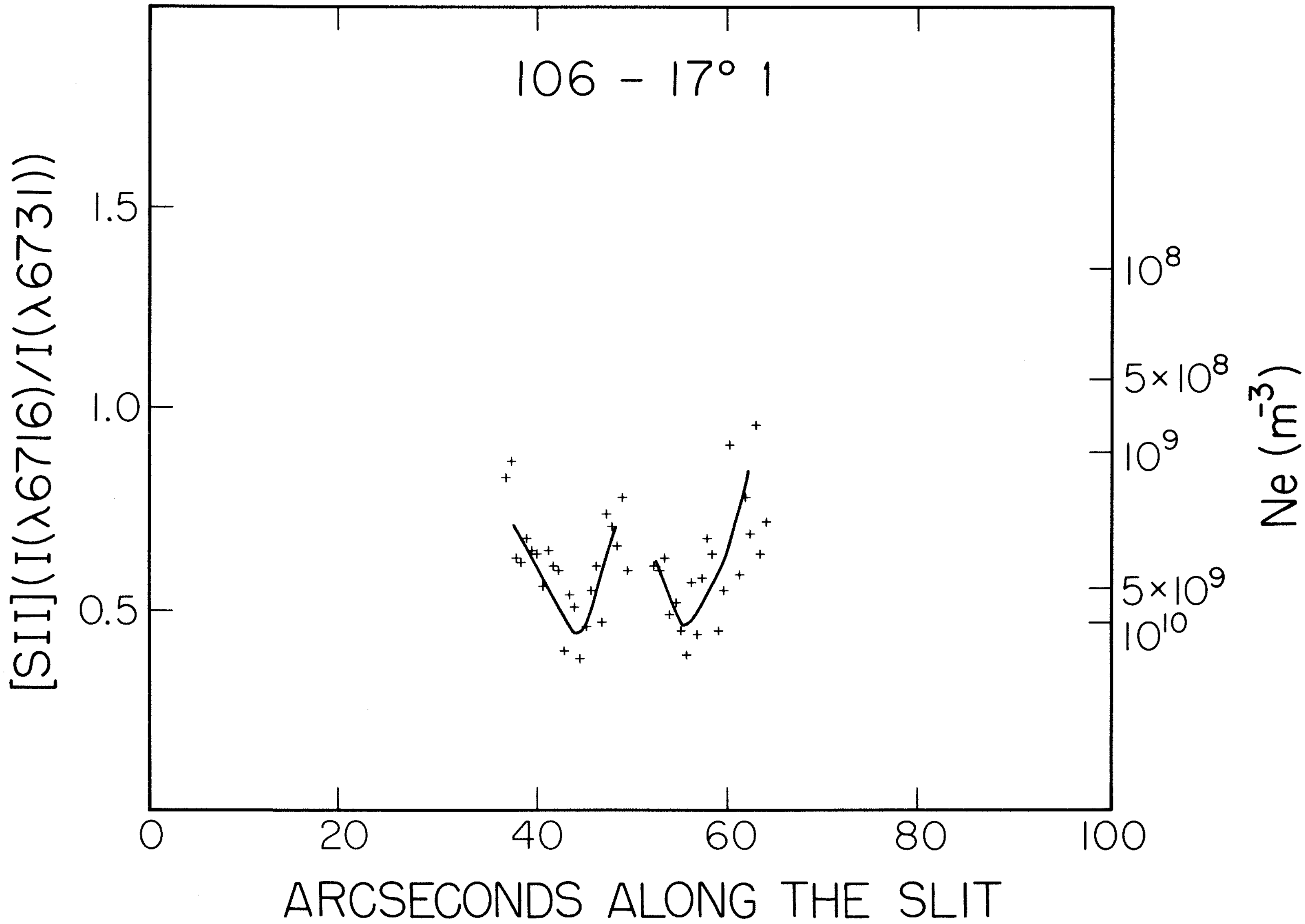
106 - 17° 1
[SII](I(λ6716)/I(λ6731))
1.5
1.0
0.5
0
20
40
60
80
100
ARCSECONDS ALONG THE SLIT
Ne (m^{-3})
10^{8}
5×10^{8}
10^{9}
5×10^{9}
10^{10}

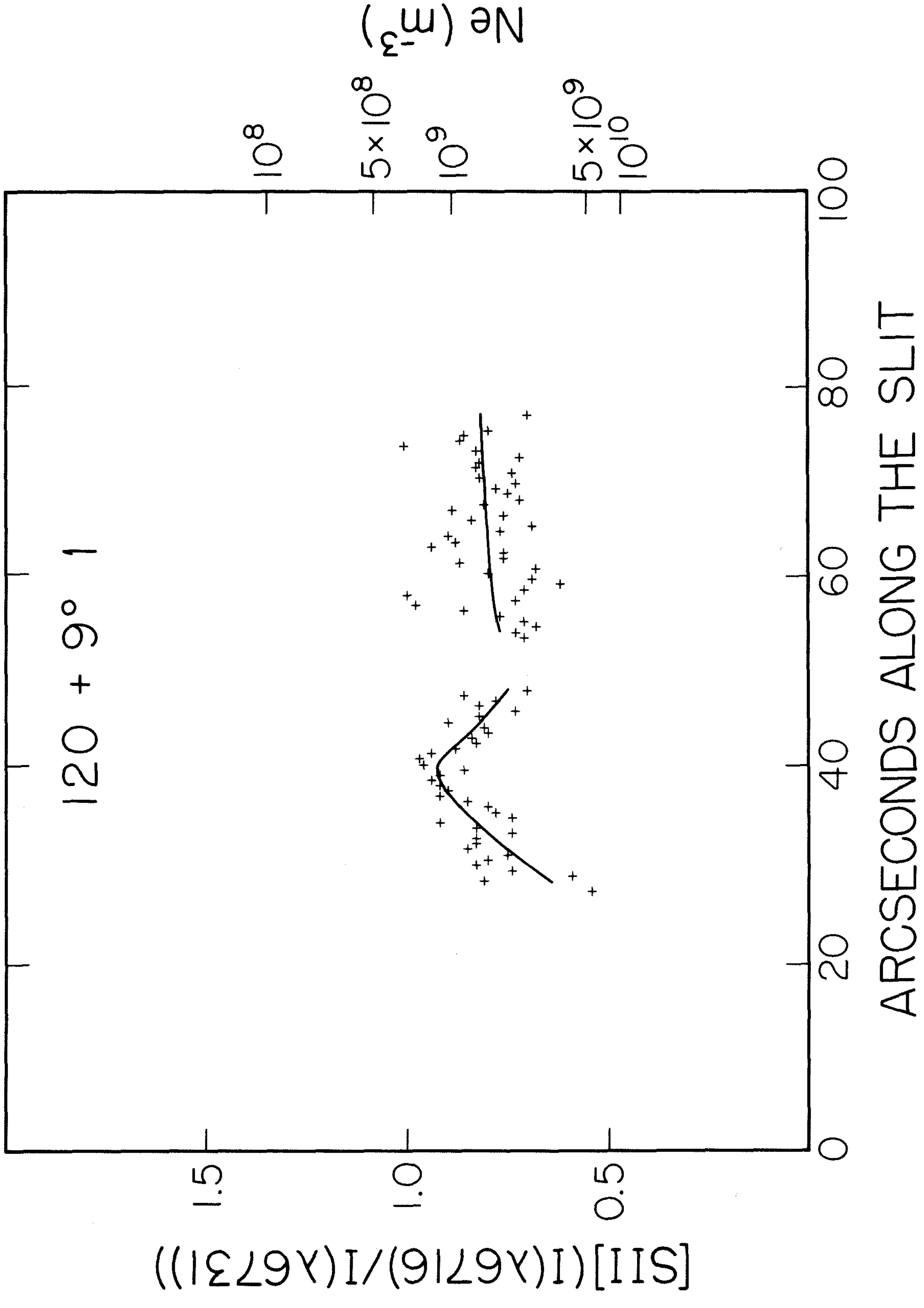
120 + 9° 1
ARCSECONDS ALONG THE SLIT
0
20
40
60
80
100
[SII](I(λ6716)/I(λ6731))
1.5
1.0
0.5
Ne (m^{-3})
10^8
5×10^8
10^9
5×10^9
10^{10}

halos may be followed. The rate of decrease is relatively slow. By inspection, the plots seem to preclude variations of the form $N_e(r) \propto r^n$ with $n \lesssim -2$. However, the plotted measurements of the electron densities in the halos most likely represent only upper limits to the true spatially averaged halo electron densities. This is because regions of locally enhanced density will tend to have higher surface brightness than surrounding regions and will therefore be preferentially conspicuous in the slit spectra. The bright filamentary structures present in many halos (e.g: see 2+5°1, 25-4°1, 83+12°1) probably represent regions of locally enhanced density. A rough estimate of the magnitude of the density enhancement may be obtained by comparing the surface brightness of the filaments to the surface brightness of adjacent halo material. The surface brightness in a recombination line (e.g: Hα λ6563) varies as

$$B_r \propto N_e N_i \, \alpha(T_e) l \quad ,$$

where N_e and N_i are the electron and ion densities, $\alpha(T_e)$ is the recombination coefficient appropriate for the line of interest and l is the line of sight path length through the emitting region. Denoting filamentary properties "fil" and adjacent halo properties "h", we may take $B_{fil}/B_h \sim 5$, and $l_{fil}/l_h \sim 0.1$ from observations. Provided the filament and general halo electron temperatures are similar we may take $\alpha_{fil}/\alpha_h \sim 1$, since α is a very weak function of temperature. Furthermore, in a pure hydrogen nebula $N_e = N_i$, giving $N_e(fil)/N_e(h) \sim 7$. This suggests that the measured electron densities, which refer primarily to filaments, overestimate the locally averaged electron densities by about a factor of 7. This is comparable to the filament density enhancement estimated by Capriotti (1973) from dynamical considerations.

The mean electron density in five planetary nebula halos, corrected as above for observational selection, is $N_e = 1.4 \times 10^8\ \mathrm{m}^{-3}$. This is equal to about 1/10th the typical electron density in the primary nebulae (Table 3). Taking $\overline{R_H/R_P} = 2$ (Section 3.1) gives the ratio of the halo volume to the primary nebula volume to be ~ 10. Hence, by this argument the order of magnitude of the ratio of the halo mass to the primary nebula mass is $M_H/M_P \sim 1$.

4. Interpretation

We consider four independent models of the origin of the nebular halos. The models, and others derived from them, have been previously proposed by other workers to account for the existence of individual halo nebulae. While each model may successfully represent some of the nebulae studied in this survey, our objective is to determine the model which is best able to represent a majority of the nebulae.

i. The halos might be caused by the scattering of nebular radiation from interstellar dust grains, as occurs in normal reflection nebulae. This model has been proposed by Atherton et al. (1979) to account for the halo surrounding NGC 7027. Several observations are inconsistent with this model of the planetary nebula halos. (a) The optical spectra of the halos are generally different from the spectra of the respective primary nebulae. However, scattering of the radiation by dust grains would be nearly grey and could not produce variations of emission line ratios. (b) Polarization measurements of the halos of 63+13°1 and 64+48°1 show that the linear polarization is $POL < 0.05$ at the wavelength of Hα. Typical reflection nebulae are observed to exhibit larger polarizations in the range

$0.05 \lesssim POL \lesssim 0.15$

(Zellner, 1973). (c) The large frequency of occurrence of halo nebulae reported in the present study would imply an unreasonably high coincidence between the spatial location of planetary nebulae and of interstellar dust clouds. Furthermore, high galactic latitude planetaries such as 64+48°1 ($b^{II} = +48°$) and 96+29°1 ($b^{II} = +30°$) possess conspicuous halos even though the interstellar medium at such large b^{II} is, presumably, very rarefied. (d) The planetary nebula halos commonly exhibit a characteristic filamentary morphology which is not similar to the morphology of known reflection nebulae. In view of the above mentioned arguments it seems very unlikely that a majority of the halos might be due to reflection nebulae.

ii. The halos might be due to excitation of the escaping stellar wind produced by the central star when in a cool pre-planetary red giant state (e.g., Kwok et al., 1978; Kwok, 1982).

Typical stellar wind mass loss rates from red giant stars are observed to lie in the range $10^{-8} \lesssim \dot{M}$ ($M_{\odot}$/year) $\lesssim 10^{-6}$ (Cassinelli, 1979). Exceptional stars, including the long period variables often cited as progenitors of planetary nebulae, have $\dot{M} \lesssim 10^{-5} M_{\odot}$/year. Such a wind expanding isotropically at the stellar escape speed from a star of mass $\sim 1 M_{\odot}$ and radius $\sim 1000 R_{\odot}$ would have a number density $N_{W}(\mathrm{m}^{-3}) \lesssim 10^{39} R^{-2}$, at distance R (m) from the central star. The observed planetary nebula halos extend to at least $R \sim 0.5$ pc $\sim 1.5 \times 10^{16}$ m (Table II). At this distance the stellar wind would have a number density $N_W \lesssim 4 \times 10^6$ m^{-3}. N_W may be compared with the halo electron densities listed in Table III. There it is seen that typical halo filament electron densities are $N_e(H) \sim 1 \times 10^9$ m^{-3}. Allowing for an estimated factor of 7 density enhancement in the halo filaments (section 3.3) gives $N_e(H) \sim 1 \times 10^8$ m^{-3} which is more than an order of magnitude larger than N_W. Hence it is apparently unlikely that the planetary nebula halos are caused by excitation of expanding stellar winds. However the uncertainties are large enough that a few of the halos may be due to such a process. Mass loss rates exceeding 10^{-4} $M_\odot$/year, if sustained for the nebular expansion time ~ 10^4 year would be able to produce the observed halo densities. Knapp et al. (1982) report mass loss rates approaching 10^{-4} $M_\odot$/year in some stars.

Excitation of the interstellar medium is even less likely to give rise to observable emission since the number densities there are very small, generally $< 10^6$ m^{-3}.

iii. The halos might represent excited gas which is expanding away from but which originated in the primary nebula shell. The halo would be formed by dynamical separation from the primary shell after its ejection from the central star. Models of this type have been computed by Mathews (1966). The outer layers of the shell undergo accelerated expansion into the relative vacuum of interstellar space. Simple considerations lead to a model of the nebula in which the radial expansion speed, v, is proportional to the distance from the central star, R. The halo consists of gas which has accelerated away from the primary nebula. Taking $v \propto R$, the condition of continuity gives $N(R) \propto R^{-3}$, where N is the total number density of particles at R, and the expansion is assumed to be spherically symmetric. Assuming N_e/N = constant (i.e. tantamount to the assumption that the hydrogen Stromgren radius is larger than the radius of the halo), and assuming constant electron temperature, the halo surface brightness in a recombination line (e.g. Hα) would vary as $B \propto R^{-5}$. Detailed calculations by Mathews in which the previous two assumptions are relaxed, yield similarly steep surface brightness variations. Comparison with the halo surface brightness profiles shown in Figure 5 suggests that accelerated expansion models of this type may be able to reproduce the planetary nebula halos. However, the model profiles are sensitive to the net heating rate in the expanding gas. The heating rate is very poorly constrained by existing observations. In the absence of more rigid constraints, in the form of resolved electron density and temperature maps of specific halos, it would seem to be premature to perform model fitting. Hence, we conclude that model (iii) in our list may be consistent with the halo observations, but that a firm conclusion cannot be reached.

iv. The planetary nebula ejection mechanism may lead to the production of two or more separate expanding gas shells, ejected from the central star at different times. We can find no strong observational test of this model in our data. However, one relevant observation is that the halo material always appears contiguous with the primary nebula. There is never a case in which the supposed halo ejection occurred so long before the primary nebula ejection that a prominent gap exists between them. Unless there is some fundamental limit to the length of time between successive ejections from the central star, this observation would seem to provide an argument against the multiple ejection model.

Further discrimination between the above formation mechanisms might be possible using radial velocity measurements of the halos. For instance, in the red giant wind model of Kwok we would expect to find a ratio of halo velocity to primary nebula velocity $v_h/v_p < 1$, since the typical stellar wind speeds are only a fraction of the typical planetary nebula expansion speeds. Conversely, the accelerated expansion models of Mathews predict $v_h/v_p > 1$. A program of halo expansion velocity measurements is presently under way at the Palomar Observatory.

5. Summary

1. 27 out of 44 nebulae for which deep CCD images were taken are found to possess halos.
2. The halos exhibit a wide range of properties. The relative radii are concentrated in the range $1.1 \lesssim (R_H/R_P) \lesssim 5$ with an average $R_H/R_p \simeq 2$. The relative surface brightnesses lie in the range $0.01 \lesssim I_H/I_P \lesssim 0.3$. Many halos exhibit filamentary structure.
3. The apparent long axes of the primary nebulae are distributed randomly in direction. There is no evidence for the axis alignment reported by Grinin and Zvereva, 1967.

4. The spatially averaged electron densities in 5 halos average $N_e \sim 10^8\ \mathrm{m}^{-3}$, about 10% of the densities of the primary nebula shells. These densities are corrected for an effect of observational selection. The correction factor is approximately equal to 1/7. The estimated ratio of the halo mass to the main shell mass is ~ 1.

5. The halos are unlikely to be produced by scattering from interstellar dust nebulae or by excitation of pre-planetary winds or of the interstellar gas. It is likely that the halos result from either the dynamical separation of a single ejected shell or from the multiple ejection of shells from the central star. In future work, expansion velocity measurements will be used to discriminate between these models.

Acknowledgements

We thank J.A. Westphal and J.E. Gunn for permission to use the PFUEI. We are thankful for the skilled operation of the telescopes by Juan Carrasco, Al Lilge, Skip Staples and Dave Tennant. Mike Ravine and Barbara Zimmerman provided valuable assistance during some of the observing runs.

References

Acker, A., 1979, *Astr. and Ap. Suppl.* **33**, 367.

Atherton, P.D., Hicks, T.R., Reay, N.K., Robinson, G.J., Worswick, S.P., and Phillips, J.P., 1979, *Ap. J.* **232**, 786.

Capriotti, E.R., 1973, *Ap. J.* **179**, 495.

Cassinelli, J.P., 1979, *Ann. Rev. Astron. Astrophys.* **17**, 275.

Curtis, H.D., 1918, *Pub. Lick. Obs.* **13**, 57.

Grinin, V.P., and Zvereva, A.M., 1967, *IAU Symp.* **34**, D.E. Osterbrock and C.R. O'Dell (eds.), D. Reidel Pub. Co., New York.

Gunn, J.E., and Westphal., J.A., 1981, *S.P.I.E.* **290**, 16.

Hunter, J.H., and Sofia, S., 1971, *Mon. Not. R. astr. Soc.* **154**, 393.

Kaler, J.B., 1974, *Astr. J.* **79**, 594.

Knapp, G.R., Phillips, T.G., Leighton, R.B., Lo, K.-Y., Wannier, P.G., Wootten, H.A., and Huggins, P.J., 1982, *Ap. J.* **252**, 616.

Kwok, S., Purton, C.R., and Fitzgerald, P.M., 1978, *Ap. J. (Letters)*, **219**, L125.

Kwok, S., 1982, *Ap. J.*, **258**, 280.

Mathews, W.G., 1966, *Ap. J.* **143**, 173.

Millikan, A.G., 1974, *Astr. J.* **79**, 11.

Minkowski, R., and Osterbrock, D.E., 1960, *Ap. J.* **131**, 537.

Osterbrock, D.E., Miller, J.S., and Weedman, D.W., 1966, *Ap. J.* **145**, 697.

Perek, L., and Kohoutek, L., 1967, Catalog of Galactic Planetary Nebulae, Prague.

Pradhan, A.K., 1978, *Mon. Not. R. astr. Soc.* **184**, 89 p.

Reimers, D., 1977, IAU Symposium No. 42, edited by R. Kippenhahn, J. Rahe and W. Strohmeier, Bamberg.

Weedman, D.W., 1968, *Ap. J.* **153**, 49.

Wentzel, D.G., 1976, *Ap. J.* **204**, 452.

Wilson, O.C., 1950, *Ap. J.* **111**, 279.

Zellner, B., 1973, in IAU Symposium No. 52, "Interstellar Dust and Related Topics," edited by J.M. Greenberg and H.C. Van De Hulst, D. Reidel Publishing Co., New York.